Modelling Physical Mechanisms of Nodule Development in Phonotraumatic Vocal Hyperfunction using Computational Vocal Fold Models

by

Jonathan J. Deng

A thesis
presented to the University of Waterloo
in fulfillment of the
thesis requirement for the degree of
Doctor of Philosophy
in
Mechanical and Mechatronics Engineering

Waterloo, Ontario, Canada, 2023

Examining Committee Membership

The following served on the Examining Committee for this thesis. The decision of the Examining Committee is by majority vote.

External Examiner:	Xudong Zheng Associate Professor, Dept. of Mechanical Engineering, Rochester Institute of Technology
Supervisor(s):	Sean D. Peterson Professor, Dept. of Mechanical and Mechatronics Engineering, University of Waterloo
Internal Member:	Arash Arami Assistant Professor, Dept. of Mechanical and Mechatronics Engineering, University of Waterloo
Internal Member:	Duane Cronin Professor, Dept. of Mechanical and Mechatronics Engineering, University of Waterloo
Internal-External Member:	Kirsten Morris Professor, Dept. of Applied Mathematics, University of Waterloo

Author's Declaration

This thesis consists of material all of which I authored or co-authored: see Statement of Contributions included in the thesis. This is a true copy of the thesis, including any required final revisions, as accepted by my examiners

I understand that my thesis may be made electronically available to the public.

Statement of Contributions

Some of the works in this thesis involve multiple authors besides myself. A summary of contributions for relevant sections is given below.

Chapter 3:

This work was co-authored by myself and my advisor, Sean D. Peterson. I developed the code, performed the simulations, analyzed data, generated figures, and wrote the first draft of the manuscript. Sean D. Peterson contributed to conceptualization, supervised the work, and reviewed the manuscript.

Chapter 4:

This work was co-authored by myself and my advisor, Sean D. Peterson. I developed the code, performed the simulations, analyzed data, generated figures, and wrote the first draft of the manuscript. Sean D. Peterson contributed to conceptualization, supervised the work, and reviewed the manuscript. Part of this chapter was published as an article in Biomechanics and Modeling in Mechanobiology [1].

Chapter 5:

This work was co-authored by myself, Sean D. Peterson (my advisor), Byron D. Erath, and Matías Zañartu. I developed the code, performed the simulations, analyzed data, generated figures, and wrote the first draft of the manuscript. Byron D. Erath and Matías Zañartu contributed to conceptualization and reviewed the manuscript. Sean Peterson contributed to conceptualization, supervised the work, and reviewed the manuscript. Part of this chapter was accepted for publication as an article in Biomechanics and Modeling in Mechanobiology [2].

Abstract

Vocal hyperfunction is a prevalent voice disorder with significant impacts on the daily lives of patients, but has poorly understood causes. At its root, vocal hyperfunction is neurological, involving excessive muscular activation due to compensation for some underlying issue. In order to improve understanding of the causes of this disorder and ultimately improve its treatment, this thesis uses computational models to investigate mechanical aspects in the development of vocal fold nodules in phonotraumatic vocal hyperfunction (a specific class of vocal hyperfunction), specifically: whether biomechanical differences in stiffness of the vocal folds can lead to inefficient speech production that predisposes one to developing these nodules, and whether swelling can establish an amplifying feedback loop, a so-called "vicious cycle", wherein swelling leads to compensatory adjustments that incur further swelling and ultimately lead to nodules. To address these questions a two-dimensional finite-element vocal fold model coupled with a simplified one-dimensional flow model was developed with modifications to this basic model made to study the phenomena of interest. Towards modelling swelling, a computationally efficient approach to model the epithelium layer of the vocal folds is also developed and validated.

To investigate the first research question, the aforementioned model was adapted to study phonation onset pressure, a measure of effort required to produce speech, as a function of vocal fold stiffness. The results show that onset pressure is primarily dependent on just three stiffness distributions: smooth distributions with body-cover stiffness differences and smooth distributions with inferior-superior stiffness differences minimize onset pressure while a uniform stiffness increase increases onset pressure. Since a uniform stiffness increase increases the natural frequency of the vocal folds (VFs), this increase in onset pressure is roughly associated with increases in frequency. This suggests that for a given average stiffness (onset frequency) deviations from an optimal body-cover and inferior-superior-like distribution lead to increases in phonatory effort that could increase susceptibility to vocal hyperfunction.

To investigate the second research question, the finite element model was augmented with a model of swelling, as well as an epithelium using a membrane model. Results showed that swelling has negligible impact on loudness of speech but significantly influences frequency, and that furthermore, swelling increases measures of phonotrauma. These results suggest that swelling could incur a vicious cycle. Specifically, a decrease in fundamental frequency initiates compensatory adjustments through increased muscle tension and subglottal pressure, which tends to increase phonotrauma in the folds, and increased swelling with phonotrauma does not tend to limit further swelling. This result demonstrates how swelling can potentially lead to the formation of nodules.

Acknowledgements

I would like to thank my advisor Dr. Sean Peterson for the many discussions and help that ultimately resulted in this work. I would like to thank Dr. Paul Hadwin for introducing me to Bayesian inference and helping me understand it. I would also like to thank the committee members Dr. Arash Arami, Dr. Duane Cronin, Dr. Kirsten Morris, and Dr. Xudong Zheng for their time in reviewing this work. To all my colleagues and friends throughout graduate school, thank you for the conversations and enjoyable times, with special mention to Winston Hu, Mohamed Serry, Eva Liu and Bobo. To the staff and faculty at the University of Waterloo, thank you for your help throughout my time here. Thanks to NSERC for graciously funding part of this work.

Finally I would like to thank my family, my parents, Lin and Shao, and sisters, Jane and Sarah, for always supporting me.

Table of Contents

List of Figures

List of Tables

List of Abbreviations

Vocal fold anatomy

VF	vocal fold
BC	body-cover
LP	lamina propria
ECM	extracellular matrix

Anatomical directions

IS	inferior-superior
ML	medial-lateral
AP	anterior-posterior

Vocal hyperfunction

VH	vocal hyperfunction
PVH	phonotraumatic vocal hyperfunction
NPVH	non-phonotraumatic vocal hyperfunction

Modelling methods

FEM	finite element method
LMM	lumped mass model

WRA	wave-reflection analog

Equations

ODE	ordinary differential equation
PDE	partial differential equation
NS	Navier-Stokes

List of Symbols

Matrix and tensor operators

$\intercal$	Transpose of a matrix
Tr	Trace of a matrix
$\cdot$	Dot product between two tensors
:	Double dot product between two tensors

Other variables

t	Time

Discretization variables

Δt	Time step
h	Finite difference step size

Strains and other kinematic variables

$\boldsymbol{X}$	Spatial coordinate in the reference configuration
$\boldsymbol{x}$	Spatial coordinate in the current/deformed configuration
$\boldsymbol{n}$	Outer normal vector to the surface in the reference configuration
$\boldsymbol{u}$	Displacement from the reference configuration
$\boldsymbol{v}$	Velocity from the reference configuration

$\boldsymbol{a}$	Acceleration from the reference configuration
$\boldsymbol{F}$	Deformation gradient
$\boldsymbol{\epsilon}$	Infinitesimal strain tensor
$\boldsymbol{E}$	Green-lagrange strain tensor
J	Determinant of the deformation gradient
$\boldsymbol{I}$	Identity tensor

Stresses and other dynamic variables

p	Pressure in a continuum or on a surface
$\boldsymbol{t}$	Surface traction
$\boldsymbol{\sigma}$	Cauchy stress
$\boldsymbol{S}$	2^{nd} Piola-Kirchoff stress

Constitutive relation variables

w	Hyperelastic strain energy function
m	Swelling-induced strain energy scaling
$\boldsymbol{K}$	Linearized elasticity tensor

Material properties

ρ	Density of a material
v	Swelling field
E	Young's modulus for an isotropic material
ν	Poisson's for an isotropic material
η	Viscosity for the damping term of a Kelvin-Voigt viscoelastic model

Variational forms

$\boldsymbol{V}$	Space of piecewise linear functions over a mesh

$\boldsymbol{W}$	Space of cell-wise constant functions over a mesh
ϕ	A hat function basis for the space of $\boldsymbol{V}$
ψ	A cell-wise constant function basis for the space $\boldsymbol{W}$

Glottal flow and acoustic variables

q	Volumetric flow rate for a 1D fluid or acoustic model
p	Static pressure for a 1D fluid or acoustic model
a	Cross-sectional area for a 1D fluid or acoustic model channel

Glottal flow model parameters

r_{sep}	Ratio of area at flow separation to minimum area in a 1D fluid channel

Acoustic measures

F_{o}	Fundamental frequency
SPL	Sound pressure level

Vocal fold model parameters

d	Depth dimension/length (the medial-lateral direction)

Dynamical system variables

X	State vector of a dynamical system
λ	Bifurcation parameter for a dynamical system
P	Generic parameter vector for a dynamical system
F	Residual function governing the dynamics for a dynamical system
p_{on}	Onset pressure
f_{on}	Onset frequency

Chapter 1

Introduction

Speech production is a process involving a complex coordinated effort across several organs of the speech system. Briefly, speech production involves the following steps [3]: The lungs are contracted to force air through the airway and out the mouth and nose. Along the airway, the flow passes through a set of visco-elastic structures in the larynx (the cartilage of the structure is externally visible as the Adam's apple in males) called vocal folds (VFs) which are adducted to narrow the channel between them, a region called the glottis. Fluid-structure interactions between the glottal flow and VFs result in a self-sustained oscillation of the VFs that modulates the glottal flow and forms the basic source of sound. This source sound is then augmented by changing the shape of the pharynx, mouth, and nasal cavities to form the wide variety of sounds people are capable of making [4, 5]. This process of speech sound production involving regular oscillation of the VFs is called phonation.

There are a wide variety of speech disorders that can disrupt the phonation process resulting in significant detrimental impacts. Roy et al. [6] found that the lifetime prevalence of voice disorders was 29.9 %, and that disorders are more common among occupations with high voice usage, resulting in an economic impact due to lost work hours. For example, Roy et al. [6] found that 7.2 % of people had missed one or more days of work due to a voice disorder. On a personal level, the presence of voice disorders is also associated with reduced quality of life [7].

Many of these voice disorders are broadly classified under the umbrella of vocal hyperfunction (VH) or are associated with it. In fact, Morrison et al. [8] found VH present in about 40 % of voice disorders. Vocal hyperfunction is a highly prevalent [9] voice disorder that involves "excessive perilaryngeal musculoskeletal activity" [9] due to compensation for some underlying issue [9, 10], where hyperfunction refers to excessive adjustments of the

speech mechanism, particularly in perilaryngeal musculature. While the general concept of VH involving a pattern of excessive muscle use is generally accepted [9], how specifically VH forms is poorly understood. Symptomatically, VH results in a sense of increased effort during voice production [9] among numerous other negative symptoms [11] and is also thought to play an etiological role in other common voice disorders [12, 13] (for example, growth of VF nodules and polyps, etc.).

Hillman et al. [13] proposed a framework for understanding VH and its hypothesized etiologies in which VH is categorized into phonotraumatic vocal hyperfunction (PVH) and non-phonotraumatic vocal hyperfunction (NPVH) forms, each with different hypothesized etiologies. In PVH, VF damage is present (presence of phonotraumatic lesions) while in NPVH, no visible damage is present. In either case, development of VH is hypothesized to start from an initial hyperfunctional response (abnormal compensatory adjustments in speech) triggered by changes in vocal function, such as from increased vocal demand, biomechanical changes in the speech system, and/or psychological factors, to name a few. In the case of PVH, the initial hyperfunctional response elicits a modified vocal function which is thought to induce further compensatory hyperfunctional responses, thus resulting in a vicious cycle and the eventual growth of nodules, a kind of phonotraumatic lesion. In the case of NPVH, the initial hyperfunctional response does not cause a cycle of self-reinforcing compensatory adjustments and no phonotraumatic lesion growth occurs. Whether a hyperfunctional response develops into PVH or NPVH is thought to be driven by a variety of factors such as individual differences in biomechanical properties of the VFs (susceptibility to damage, etc.), psychological factors, and sensorimotor deficits, among others.

Biomechanical factors are an important class of hypothesized etiologies of VH as confirmed by a range of experimental and computational studies. Experimental studies have provided strong support for the idea that biomechanical factors do play a role. For example, clinical measurements of glottal aerodynamics in patients with PVH show that these patients require higher subglottal pressures than normal to achieve typical speech volumes, which also reflects increased potential for vocal fold trauma [12–14]. Limited computational studies have investigated specific biomechanical factors in the etiology of VH. Galindo et al. [15] and Zañartu et al. [16] showed that the presence of a posterior glottal gap can induce compensatory changes in subglottal pressure to achieve normal speech volumes at the cost of increased collision forces and risk for phonotrauma, which suggests that the posterior glottal gap is a potential biomechanical factor that can result in PVH. Many more biomechanical factors, however, remain unexplored.

One important biomechanical factor that could predispose some patients to the development of PVH are stiffness distributions in the VFs that lead to effortful speech production. Viscoelastic properties of the VFs have long been considered key to their vibration. One

of the first such studies to hypothesize this was performed by Hirano et al. [17] who noted the VFs have layers that can be roughly grouped into a body-cover (BC) structure wherein the outer cover is softer and the inner body is stiffer; Hirano et al. [17] hypothesized that varying the properties of these two groups changed the manner of VF vibration. Since stiffness differences in the VFs play a critical role in their oscillation, they can also contribute to increased 'effort' of speech production which would require higher subglottal pressure and thus increase potential for phonotrauma and the development of PVH. Computational studies using models of the VFs have confirmed this by showing that stiffnesses of the BC groups have a strong impact on the the 'effort' of speech production as measured by phonation onset pressure, the minimum pressure required to initiate phonation [18–22]. While these studies demonstrate the importance of body and cover stiffness of the VFs on phonatory effort and onset pressure, recent studies show that stiffness distributions within the VFs are more complicated than the BC grouping suggests. For example, gradients in stiffness exist within the cover layer [19, 23], and smooth transitions in the protein distributions between VF layers are also present in contrast to the discrete layer transitions that are usually considered [24]. Furthermore, studies have also shown that some of these stiffness variations (such as gradients in the inferior-superior direction in the cover) affect VF dynamics and likely onset pressure [25, 26]. Because most of these more complicated stiffness variations' effects on onset pressure have not been studied, it is unknown what types of stiffness distributions play the biggest role in increasing phonatory effort (phonation onset pressure), and thus what kinds of stiffness distributions would play the biggest role in increasing risk for VH.

Another important hypothesized biomechanical factor in the development of PVH and growth of nodules is VF swelling (or edema) [13], which is commonly seen after periods of voice usage [27, 28] and is a hypothesized mechanism that can trigger a hyperfunctional response. Swelling of tissues results in the local accumulation of fluid and changes in their mechanical properties [29]. In the case of VFs, small amounts of swelling are seen after voice usage [30] and could have beneficial effects such as in vocal warm up exercises; however, larger amounts of swelling will likely lead to modified vocal function potentially triggering a hyperfunctional response. Furthermore, this hyperfunctional response would lead to hyperfunctional compensatory adjustments, and if these compensatory adjustments result in further swelling, a vicious cycle could form. To the best of our knowledge, however, there are no studies demonstrating how or if swelling can trigger such a hyperfunctional response. The most closely related studies have investigated the effects of biphasic models of water and solid phases in VF tissues to study the effects of fluid motion on VF behaviour [31–34]. While these studies demonstrated water content in the VFs plays an important role in voice production, they did not capture the accumulation of fluid and subsequent changes

in shape that occur during swelling.

1.1 Objectives

This research aims to investigate two biomechanical factors in the etiology of PVH and eventual development of VF nodules. Specifically, on the role of VF stiffness distribution in increasing phonatory effort that would increase the risk of developing PVH, and on the role of swelling in triggering compensatory responses that lead to the vicious cycle of PVH and eventual development of nodules, using computational models of the VFs. Towards this, this work develops two models, one which can be used to compute phonation onset pressure as a measure of phonatory effort, and a model that captures the physical effects of swelling in order to investigate if biomechanical changes induced by swelling can lead to PVH. Due to limitations in past literature, development of the swelling model also involves the development of an epithelium model which more accurately captures the effects of a lumped cover layer.

Specific objectives for this research are:

1. Explore the sensitivity of phonation onset pressure to stiffness distributions within the VFs to uncover if particular stiffness distributions have larger impacts on increasing onset pressure and thus risk for developing PVH.

2. Investigate how modelling separate epithelium and lamina propria (LP) layers differs from modelling a single cover layer and develop a membrane model of the epithelium to reduce computational cost of modelling the epithelium.

3. Develop a model of VF swelling to investigate if/how swelling induced changes in the VFs can trigger a hyperfunctional response and vicious cycle, and thus if swelling can trigger the development of nodules in PVH.

Chapter 2

Background

The following sections provide background information on speech, speech modelling, and inverse analysis. Section 2.1 covers the general speech system, the anatomical terms used to describe locations and orientations of speech structures, and the qualitative physics of speech generation. Section 2.2 discusses the approaches used in literature to model speech generation and in particular, VF vibration. Finally, Section 2.1 discusses background on topics specific to the contained projects.

2.1 Speech background

Speech production is a complex process through which sound is generated with multiple types of sounds and correspondingly different sound generation mechanisms. Likely the most common type of sound, voiced speech (or phonation) correspond to sustained sounds, such as vowels ('a', 'e', 'i', 'o', and 'u') in English, and involves regular vibration of the VFs (further described below). Other types of sounds include fricatives (blowing type sounds as in 'f') and even click consonants (as in 'tsk, tsk') neither of which involves VF vibration. This thesis focuses on the first type, phonation, as the most typical form of sound generation and clinical importance.

2.1.1 Anatomy and function

To describe the locations and orientations of structures in the body, anatomical terms are used as shown in Figure 2.1A, which are introduced here to familiarize the reader.

Three major planes called the, sagittal, transverse, and coronal planes are used to describe orientations of surfaces and cross sections [35, 36]. Similarly, three major directions called, medial-lateral (ML), inferior-superior (IS), and anterior-posterior (AP) are used to describe directions and relative locations of structures.

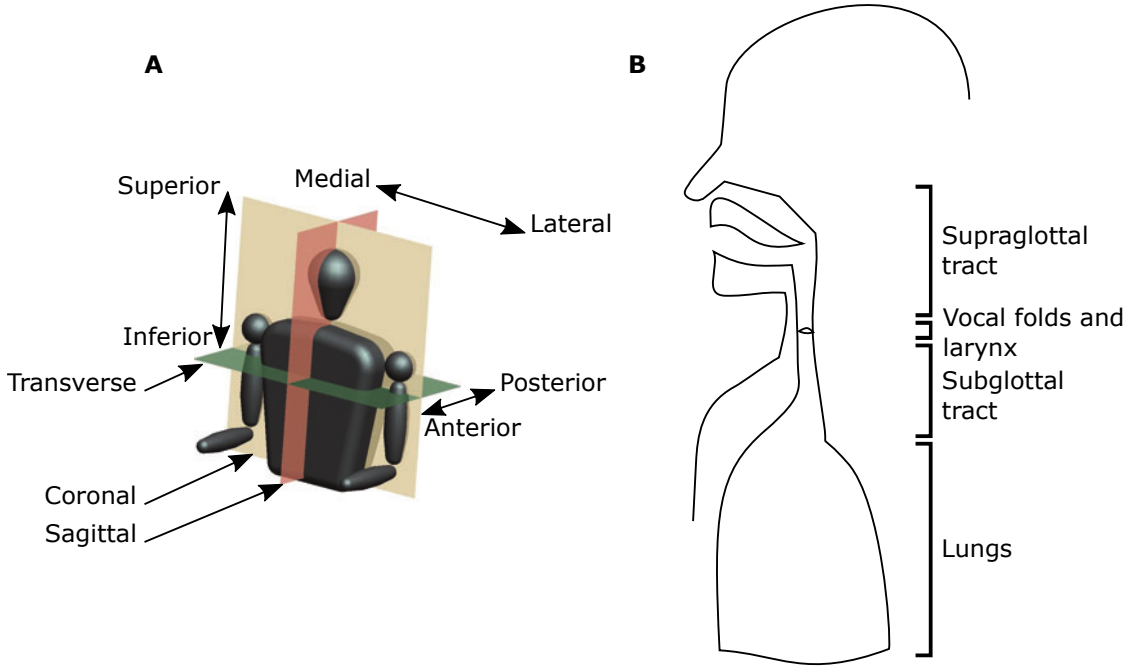

Figure 2.1: (A) Schematic of anatomical directions and planes used to describe locations in the body (adapted from [35]). (B) Summary of major organs that play the most direct role in the physical production of speech. Note the medial and lateral directions point toward and away from the midplane of the body, respectively

Phonation involves a complex system consisting of several structures across the body, for example, neurological control systems, bony supporting structures, and musculature to name a few [36] (we refer the reader to [36] for an in-depth description of the anatomy of the speech system). Here we elaborate on a subset of these structures that play the most direct role in voiced speech production, which span from the lungs to the mouth and nose, as shown in Figure 2.1B. Broadly, these structures are the lungs, trachea, larynx (and VFs), and supraglottal tract, which includes the oral and nasal cavities.

During phonation, each of the organs in the speech system plays a special role working together to produce speech through a process roughly detailed as follows. The lungs

contract which increases pressure and drives air flow through the trachea, larynx and mouth/nose. Inside the larynx the VFs are adducted, which narrows or closes the airway. The forces exerted by the flow on the adducted VFs and their visco-elastic properties lead to a self-sustained oscillation of the VFs on the order of 80 Hz to 220 Hz with men at the lower end of this range and women at the higher end [35]. Musculature and cartilages within the larynx and VFs can also be adjusted to modulate the frequency of amplitude of the VF oscillation. The VF oscillation modulates the flow from the lungs forming a base sound source. By changing the shape of the vocal tract and oronasal cavities (for example by moving the lips or tongue), the 'quality' of the source sound is changed. The overall process can be described as a source-filter [4] where the VF vibration forms a source of sound, and the supraglottal tract shapes it. This allows sounds with the same pitch (or fundamental frequency) to sound different, as in vowels 'a' and 'e', or different instruments playing the same note.

The larynx's role consists of laryngeal musculature and cartilages, as shown in Figure 2.2, which facilitate, for example, VF abduction during phonation and modulation of VF properties. Specifically, motion of the cartilages and changes in muscle tension caused by activations in laryngeal musculature result in changes to the VF length, tension, and position. The resulting modified VF properties lead to changes in the frequency and amplitude of VF motion, which roughly control the pitch and volume of the output sound [37].

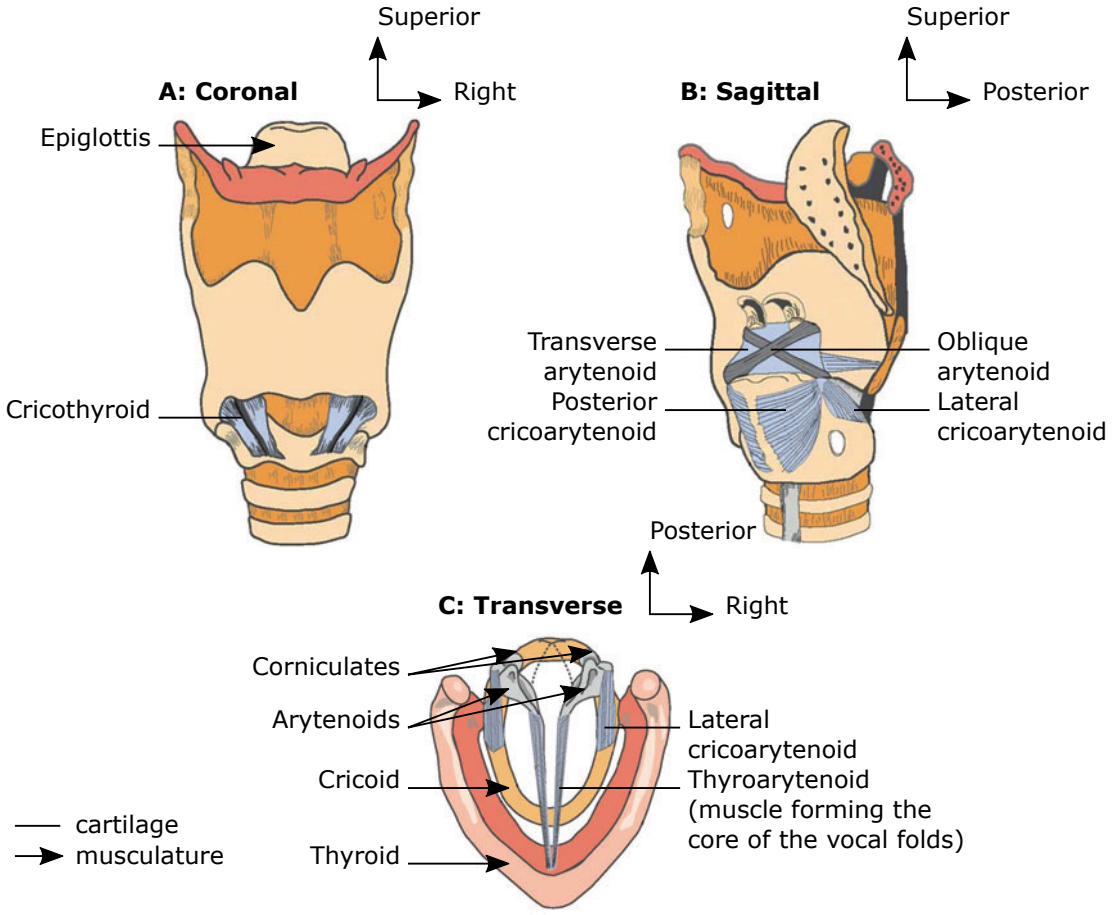

Figure 2.2: (A) Coronal, (B) sagittal, and (C) transverse plane views of the laryngeal cartilages (indicated by lines with arrowheads) and musculature (indicated by plain lines), adapted from [35]. Note the thyroarytenoid muscles form the inner core of the vocal folds

The VFs are attached between the arytenoid and thyroid cartilages (Figure 2.2). The central core of a VF is the thyroarytenoid muscle (muscles are usually named by their attachment points; for example, the thyroarytenoid muscle attaches to the thyroid and arytenoid cartilages). When the VFs are adducted or abducted, the lateral cricoarytenoid muscles activate, twisting the arytenoids about the IS axis, which brings the VFs together. The larynx can also tense and lengthen the VFs, changing the frequency and amplitude of vibration and, therefore, the frequency and volume of the output sound. This is accomplished primarily through the thyroarytenoid and cricothyroid muscles [38]. When the thyroarytenoid tenses, the core of the VFs becomes stiffer, which tends to increase the

frequency of vibration and decrease amplitude. When the cricothyroid tenses, the thyroid cartilage is pulled anteriorly stretching the entire VF (the VFs are stretched due to attachment between the thyroid and arytenoid cartilages as shown in Figure 2.2 C), increasing tension and also tending to increase the frequency of vibration.

The VFs themselves consist of a layered structure with each layer having distinct viscoelastic properties as shown in Figure 2.3.

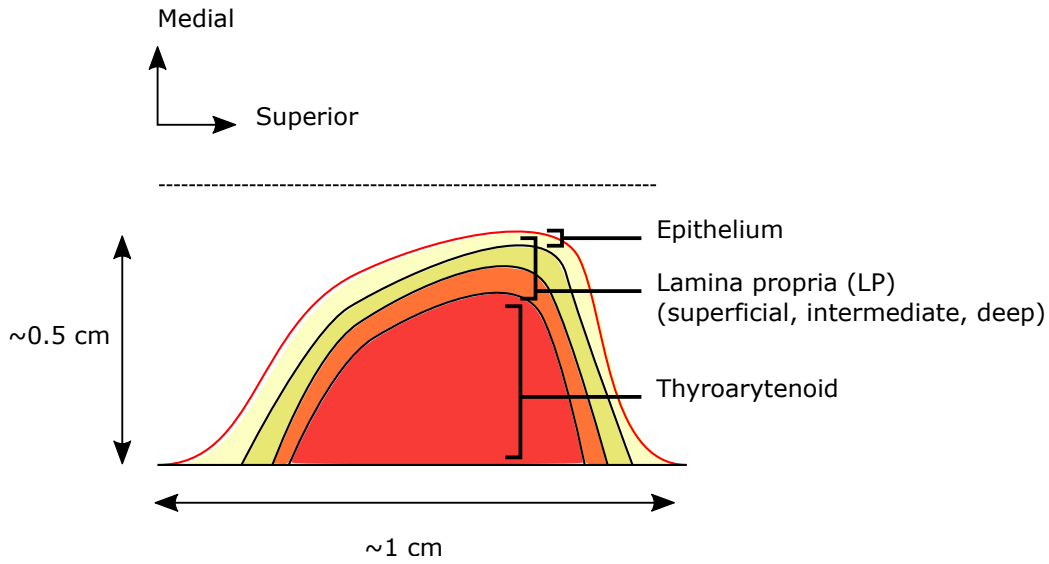

Figure 2.3: A coronal cross section of the vocal folds showing the epithelium, lamina propria (LP) (which is further divided into three layers), and thyroarytenoid layers. Thickness, depth, and length are on the order of 1 cm, 0.5 cm, and 1.6 cm, respectively, but vary with gender and muscle activation [39]

There are a total of five layers consisting of the innermost thyroarytenoid muscle, three layers of the LP and an outermost epithelium. While the inner muscular layer (the thyroarytenoid muscle) and deep LP are stiff, the superficial LP, intermediate LP, and epithelium are loose [40]. This often leads to a further functional classification into the BC grouping, where the 'body' consists of the stiff thyroarytenoid and deep LP and the 'cover' consists of the remaining loose LP layers and epithelium [40].

2.1.2 Speech production control loop and vocal hyperfunction

The biomechanical process of speech production described in the previous sections is embedded within a control loop as shown in Figure 2.4. Starting from the brain (Figure 2.4A)

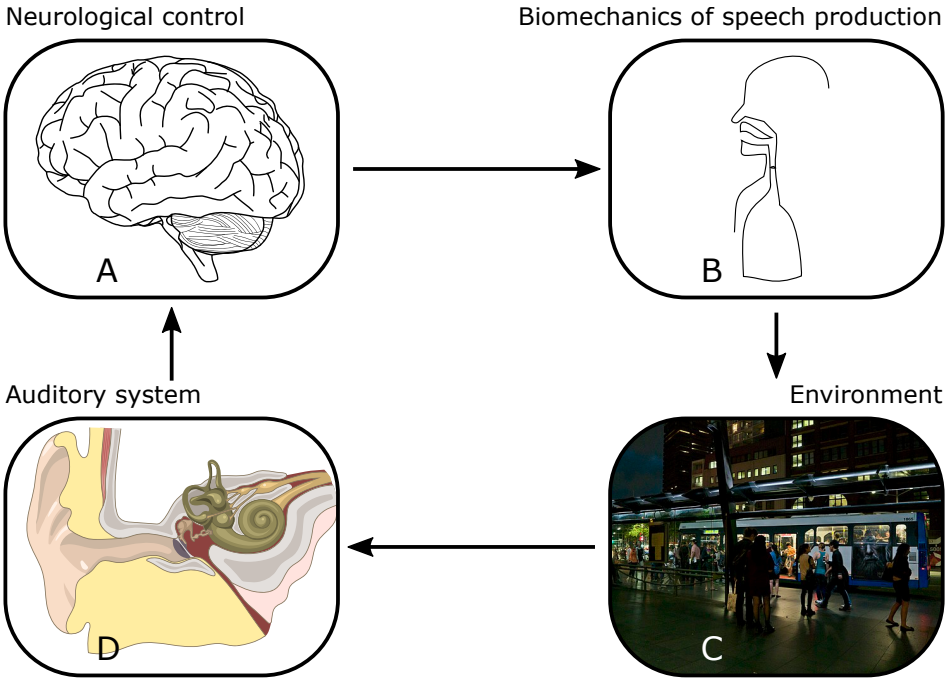

(A) Unknown. Edited to transparent by User:Amousey. (https://commons.wikimedia.org/wiki/File:Brain-outline-lateral.svg), "Brain-outline-lateral", https://creativecommons.org/publicdomain/zero/1.0/legalcode
(C) DataBase Center for Life Science (DBCLS) (https://commons.wikimedia.org/wiki/File:202108_Ear_structure.svg), https://creativecommons.org/licenses/by/4.0/legalcode
(D) John Robert McPherson (https://commons.wikimedia.org/wiki/File:Night_commuters_Railway_Square_bus_station_George_St_Haymarket_City_of_Sydney_L1000518a.jpg), Cropped by Jonathan Deng, https://creativecommons.org/licenses/by-sa/4.0/legalcode

Figure 2.4: An example control loop in speech production showing how a target sound from the brain results in an eventual received sound that is heard. Clockwise from the top right, the categories depict: (A) neurological control, (B) biomechanical sound production, (C) environmental sounds, and (D) the auditory system

signals are sent to the biomechanical organs of speech production to produce a desired

speech output, sound is produced through a physical process, the resulting sound is modified by the environment, and finally interpreted by the auditory system. In this control loop, muscular adjustments are automatically made in order to account for differences between the desired sound output and what an individual ultimately hears [41]. Compensatory muscular adjustments might occur due to changes in any of the depicted categories in Figure 2.4 or others. Types of compensatory muscular adjustments may include, for example, thyroarytenoid and cricothyroid adjustments, or diaphragm adjustments changing lung pressure. A classic example of this is the Lombard effect; the Lombard effect occurs when people speak in loud environments which results in automatically speaking louder to adjust for the louder surroundings [42], for example, by increasing pressure at the lungs.

Vocal hyperfunction is theorized to involve abuse of this compensatory mechanism such that excessive, or hyperfunctional, compensations occur that become pathological [13]. According to Hillman et al. [13] there are numerous potential factors that can play a role in the formation of VH or predispose someone to developing it. To explain different etiologies of VH, Hillman et al. [13] categorizes VH into two forms with multiple potential causes and factors that can precipitate each (for further details, see [13]). In the case of NPVH, hyperfunctional compensation can be triggered by a variety of factors, but phonotraumatic lesions (or nodules) do not appear. In the case of PVH, hyperfunctional compensation can similarly be triggered by a variety of factors, but phonotraumatic lesions do appear. The reason for the difference in presence of phonotraumatic lesions between the two types is thought to include a wide variety of potential factors ranging from differences in personality traits to differences in susceptibility to tissue damage.

A key feature of PVH is that the development of phonotraumatic lesions (for example, nodules) occurs due to a vicious cycle. According to the vicious cycle hypothesis, initial hyperfunctional adjustments trigger changes in speech production that encourage further hyperfunctional compensation. An example of this is the hypothesized role of swelling in triggering such hyperfunctional adjustments. Small amounts of swelling are thought to trigger hyperfunctional adjustments that subsequently encourage further swelling [13] eventually resulting in the development of phonotraumatic lesions.

2.1.3 Phonation physics

Vocal fold motion

Self sustained oscillation of the VFs is explained by the myoelastic-aerodynamic theory of phonation [43], which hypothesizes that VF vibration is the result of interactions between

forces of the glottal flow and the viscoelastic VFs. To broadly illustrate this process, the motion of the VFs is broken down into four main phases as shown in Figure 2.5A [44].

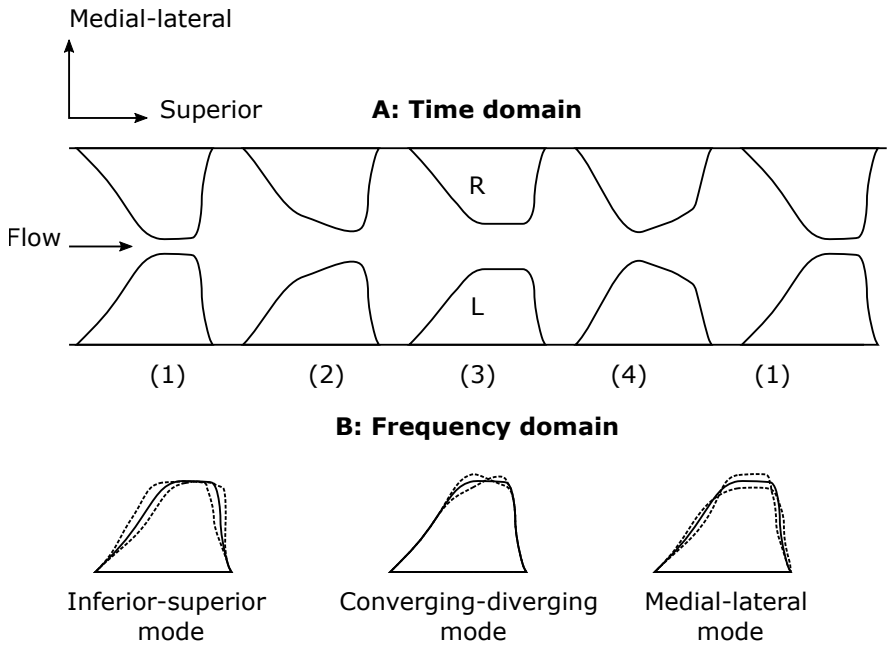

Figure 2.5: (A) Time domain motion of the vocal folds (adapted from [44]) decomposed into closed (1), opening (2), maximal opening (3), and closing (4) phases. (B) Frequency domain motion of the vocal folds (adapted from [45]) decomposed into three normal modes: inferior-superior mode, converging-diverging mode, and a medial-lateral mode. The dotted lines indicate the vibrating extents of the mode

Starting from an initially closed phase (Figure 2.5A (1)), subglottal pressure from the lungs forces the VFs apart. This happens in a converging configuration since the pressure was first applied at the inferior side of the VFs. As the folds move apart, the viscoelastic forces from compression overcome the pressure forces and momentum of the VFs, causing them to begin closing again. If the folds close in a diverging configuration, the pressure loading over the folds is reduced since flow separates somewhere along the diverging channel due to the adverse pressure gradient. This reduces the net pressure force compared to the opening phase and allows the VFs to return to closure. The alternating converging-diverging motion is known as the mucosal wave and is thought to be a key component of VF oscillation since it leads to an asymmetry in the fluid loading between the opening and closing phases [18].

The motion of the VFs during phonation also often be qualitatively decomposed into just a few primary modes of vibration: an IS mode, a converging-diverging mode, and a ML mode, as illustrated in Figure 2.5B [45]. The natural frequency and shape of each mode correspond to 'eigenmodes', which are characteristics of the specific configuration and material properties of the VFs in absence of any fluid forcing (see [45] for a more detailed description of modal analysis of VFs). These simple modes are often qualitatively seen in VF vibration, for example, in the mucosal wave and opening and closing motions of the VFs, which can be decomposed into the ML and converging-diverging modes. The lowest natural frequencies of these eigenmodes also correlate well with oscillation frequencies seen during phonation [45].

Glottal aerodynamics

The glottal flow during phonation varies due to the periodic motion of the VFs (see Figure 2.5). As described above, the flow is driven by a pressure difference from the high pressure at the lungs to atmospheric pressure in the vocal tract with the main pressure drop occuring over the constriction formed by the VFs. Typical lung pressures are on the order of 1000 Pa and lead to mean glottal flow rates of about $100\,\mathrm{mL\,s^{-1}}$ [35]. This corresponds to a Reynolds numbers on the order of 100 to 10 000 when considering the amplitude of VF motion as the length scale (about 1 mm) [35]. During the different phases of VF motion (Figure 2.5), the general flow behaviour changes due to the shape of the glottal channel. When the glottis is open and converging, the flow accelerates in the converging channel causing a drop in pressure along the medial surface. At the superior edge of the VFs, the rapid opening causes an adverse pressure gradient and subequently flow separation. As the VFs begin closing in a diverging configuration, pressures tend to increase along the diverging channel due flow deceleration. This leads to an adverse pressure gradient, which causes flow separation somewhere along diverging channel, reducing the total force on the VFs compared to the converging configuration. Finally near closure, viscous effects of the flow become strong in the thin channel between the VFs slowing the flow and leading to a build up of pressure that starts the cycle again.

There are also numerous complex flow phenomena that occur during the VF motion, as illustrated in Figure 2.6.

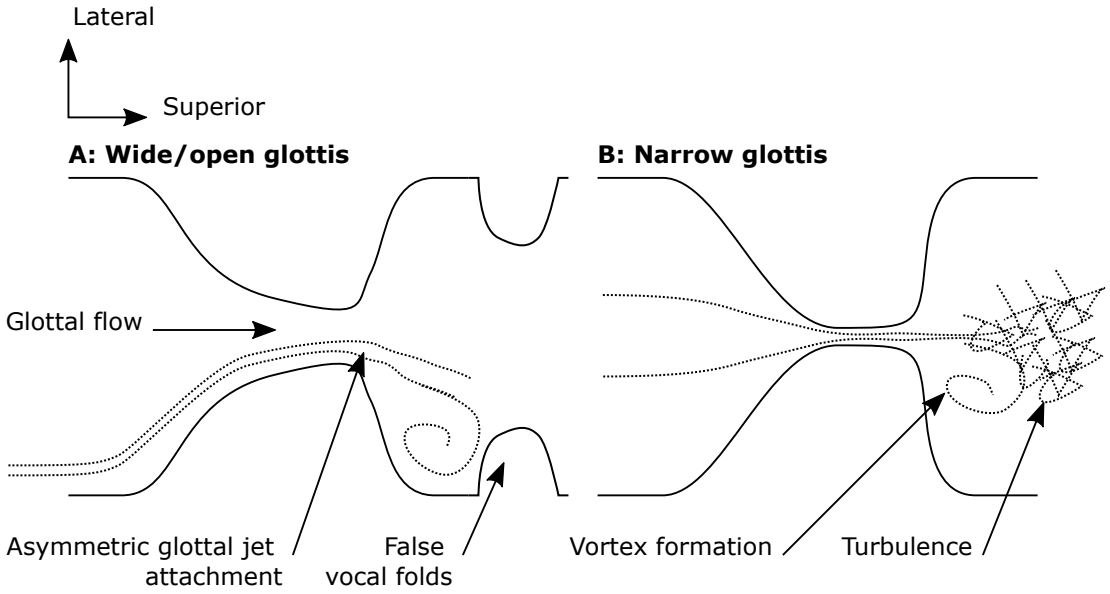

Figure 2.6: Illustration of some complex flow phenomena in (A) a wide (or open) glottis and (B) a narrow glottis

For example, the false VFs, structures located downstream of the true VFs can potentially affect the glottal flow by reducing the pressure drop across the VFs from flow separation [35, 46]. Asymmetries in the flow can also form as the flow separates in the diverging channel, forming a glottal jet that attaches to either the left or right VF [47]. This one-sided attachment can subsequently lead to asymmetric surface pressures between the two VFs that contributes an asymmetric forcing [44]. Further features of the glottal flow include the formation of turbulence in the glottal jet and vortex formation in the glottis, which contribute to sound generation and produce unsteady forces, respectively [35]. These are just a few examples of the complex flow features occurring in the glottis illustrating some of the complex physics involved in VF vibration (for a more comprehensive review of the glottal aerodynamics, see [35]).

Acoustics and filtering

The varying glottal flow and vocal fold motion described previously leads to a production of sound energy though a complex physical process where the bulk flow energy and VF motion is converted to acoustic energy that subsequently propagates through the subglottal and supraglottal tracts. This conversion process can happen through different mechanisms

such as through motion of the walls, and turbulence or vorticity in the flow [35, 48, 49]. The resulting generated sound is often classified in terms of acoustic poles, or idealized point sources of acoustic excitation [50]. Under this classification, the three main sources of sound are monopole, dipole and quadrupole sources [35], which come from different excitations or mechanisms. The monopole source comes from the volume displaced by the VFs, the dipole by the unsteady force of the VFs on the glottal flow, and quadrupole sources from turbulence in the flow [35]. These acoustic sources form a base sound that is modified or filtered as the acoustic waves propagate through the supraglottal and subglottal tracts. Due to the periodic motion of the VFs, the base sound can be decomposed into integer multiples (harmonics) of the fundamental frequency, F_o, which characterizes the pitch of the sound and is the frequency of VF motion. As the acoustic waves travel through the supraglottal tract, the changing area of the tract leads to reflections and transmissions throughout the length. This emphasizes some of the harmonics and reduces others leading to a change in the spectral content of the sound ultimately emitted from the mouth and nose [4, 5]. This process of filtering the base sound is referred to as the source-filter theory [4]. This process also occurs in the subglottal tract although the modulated sounds are less audible.

While the source-filter theory hypothesizes a one-way interaction from the source to the filter, the filtered acoustic waves can also affect the source by influencing the motion of the VFs. The degree of interaction likely depends on the specific sounds being made [51]. Strong interactions have been theorized to happen, for example, if the frequency of vibration is close to that of the first formant (the first harmonic frequency that is emphasized by the supraglottal tract) [51]. Under these strong interactions, VF vibration can potentially be destabilized, leading to nonlinear interaction such as sudden jumps in pitch [51]. In other cases corresponding to a large diameter supraglottal tract above the glottis, the acoustic-source interaction has been theorized to be much weaker [51].

2.2 Numerical models

Modelling phonation is complex due to the combined fluid-structure-acoustic interactions involving acoustics in the supra and subglottal tracts, fluid flow through the glottis, and structural deformations of the viscoelastic VFs. The following sections provide further information on numerical methods used to solve each of the fluid, solid and acoustic domains individually, followed by the coupling conditions.

2.2.1 Vocal fold models

There are two main approaches to model the VFs: those based on continuum physics using the finite element method (FEM), and lumped mass models (LMMs) that model the VFs as a spring-mass-damper system. These model classes take different approaches to capturing the pertinent physics of VF vibration, such as contact, viscoelasticity, and modes of vibration. These are further described in the following sections.

Lumped-mass models

In LMMs, VFs are modelled by a spring-mass damper system such as the two-mass model shown in Figure 2.7 [52]. Discrete masses are used to represent the mass of the VFs, springs and dampers to represent their viscoelastic behaviour, and generally, additional contact springs are used during contact to represent energy storage and release due to VF compression [53]. The dynamics of the masses are governed by Newton's second law.

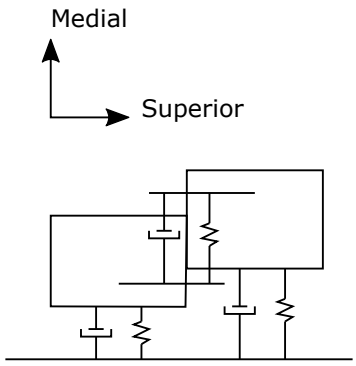

Figure 2.7: A schematic two-mass model [52], an example of a lumped-mass model, with connecting springs and dampers

A variety of LMMs have been proposed mainly consisting of variations in the number of masses used to represent the VFs (see Figure 2.7 illustrating a two-mass model), the form of spring and damping forces used to connect the masses, and the strategies used to model contact [53]. LMMs with greater numbers of masses (and thus degrees of freedom) can represent more vibration modes and therefore more complex motion. Due to the relatively simple form of LMMs, solution procedures for them are also straightforward. The system of spring mass dampers in LMMs results in a system of ordinary differential equations

(ODEs) that can be integrated in time with established methods, such as the family of Runge-Kutta methods (for example, see [54]).

Lumped-mass models have been used extensively to model the VFs. One of the earliest examples is the one-mass model of Flanagan and Landgraf [55], which simulated the VFs as a single vibrating mass. This early approach was unable to capture important physical phenomena, such as the mucosal wave, but nevertheless was able to simulate voiced sounds when coupled with an acoustic tract. Later works developed improved LMMs to better capture the physics of VF vibration. For example, the two mass model of Ishizaka and Flanagan [56] improved on the one-mass model by incorporating an additional mass in the IS direction that allowed the model to capture the mucosal wave. Later works have introduced even further variations of LMMs that aim to improve the captured physics. These variations of LMMs generally consist of choosing different numbers of masses and different connecting elements to capture increasingly complex modes of vibration and material behaviour of the VFs. An example is the 3-mass model of Story and Titze [54], which adds an additional mass under the two mass model, therefore allowing the model to represent the VF body and cover layers.

The simplicity of LMMs leads to small computational costs but comes at the cost of model fidelity. Small computational costs make LMMs suitable for large parametric studies [53], such as investigating the effects of combinations of muscle contraction [38]. The weakness of LMMs is in making direct quantitative comparisons with real VFs [57] and comes from two aspects. Firstly, it is difficult to relate the abstract discrete block parameters of LMM to those of continuous real VFs, making one-to-one comparisons difficult [57, 58]. Secondly, LMMs are likely unable to capture the complex physics of real VFs making their quantitative predictions less accurate [57].

Continuum models

In the continuum approach, the VFs are treated as continuous bodies which are governed by the equations of motion for continua (for an introduction to continuum mechanics see [59]) and constitutive equations are used to model viscoelasticity. Contact in the continuum formulation is an inequality [60] that prevents the VFs from overlapping either each other or some rigid surface. An example continuum model is shown in Figure 2.8.

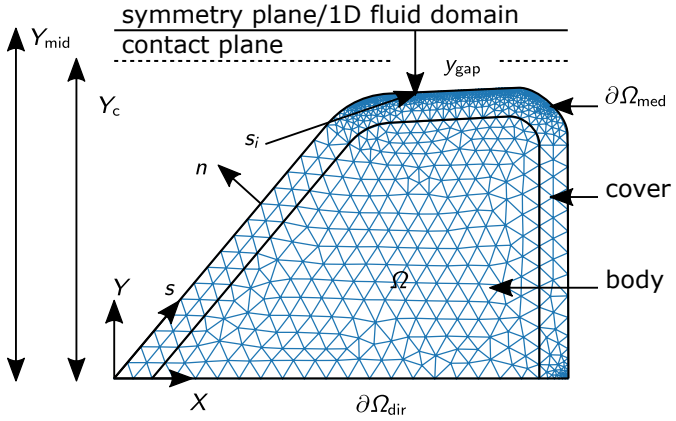

Figure 2.8: An example of a 2D continuum model discretized using a triangular mesh in the reference configuration with coordinates $\boldsymbol{X} = (X, Y)$ and medial surface coordinate, s

A variety of continuum models have been proposed with different choices for the constitutive equation, spatial dimensions (2D or 3D), geometry of the VFs, and assumptions about the physics, such as whether small or large deformations apply, or whether left-right symmetry applies. Generally, more complex constitutive equations (such as nonlinear viscoelastic stress-strain relationships [61]), more physiologically realistic geometries, and fewer assumptions should improve the fidelity of VF models, although this usually comes with increased computational cost.

Continuum models are governed by partial differential equations, which require discretization in space and time to solve, as well as appropriate methods to model the inequality imposed by contact. To solve these continuum models, a common strategy is to discretize the spatial dimension using the FEM method and use one of a few possible contact modelling strategies. This results in a system of ODEs that can then be integrated in time, similar to LMMs. The specific governing equations depend on the assumptions made. Equations for a continuum model assuming a symmetric VF with small deformations and the Kelvin-Voigt constitutive equation are illustrated here, which has been commonly employed for modelling viscoelasticity of biological materials [61, 62]. For the domain illustrated in Figure 2.8 the system is governed by the Navier equations [63, 64]

$$\begin{aligned} \rho_{\text{vf}} \frac{\partial^2 \boldsymbol{u}}{\partial t^2} &= \nabla \cdot \boldsymbol{\sigma} \text{ in } \Omega \\ \boldsymbol{u} &= 0 \text{ on } \partial\Omega_{\text{dir}} \\ \boldsymbol{\sigma} \cdot \boldsymbol{n} &= \boldsymbol{t} \text{ on } \partial\Omega_{\text{med}} \\ \text{such that} \quad Y_{\text{c}} - Y &= Y_{\text{gap}} \geq 0 \text{ on } \partial\Omega_{\text{med}}, \end{aligned} \tag{2.1}$$

where $\boldsymbol{u}(\boldsymbol{X}, t)$ is the displacement vector field, t is time, $\boldsymbol{\sigma}$ is the Cauchy stress tensor, ρ_{vf} is the density of the VFs, $\boldsymbol{t}$ is a surface traction with contributions from the fluid pressure (typically due only to pressure for inviscid flows) and contact, $\boldsymbol{n}$ is the outwards normal to the surface, and $\boldsymbol{X} = (X, Y)$ is the reference configuration coordinate. The deformed configuration $\boldsymbol{x} = (x, y)$ is then given by $\boldsymbol{x} = \boldsymbol{X} + \boldsymbol{u}$, and the inequality on Y_{gap} represents the effect of contact. Equation (2.1) does not specify a constitutive model; for a Kelvin-Voigt constitutive model, $\boldsymbol{\sigma}$ is related to strain through [61]

$$\begin{aligned}
\boldsymbol{\sigma} &= \frac{E\nu}{(1+\nu)(1-2\nu)}\text{Tr}(\boldsymbol{\epsilon})\boldsymbol{I} + 2\frac{E}{2(1+\nu)}\boldsymbol{\epsilon} + \eta\dot{\boldsymbol{\epsilon}}, \\
\boldsymbol{\epsilon} &= \frac{1}{2}\left(\frac{\partial \boldsymbol{u}}{\partial \boldsymbol{X}} + \frac{\partial \boldsymbol{u}}{\partial \boldsymbol{X}}^{\intercal}\right), \\
\dot{\boldsymbol{\epsilon}} &= \frac{1}{2}\left(\frac{\partial \boldsymbol{v}}{\partial \boldsymbol{X}} + \frac{\partial \boldsymbol{v}}{\partial \boldsymbol{X}}^{\intercal}\right),
\end{aligned} \tag{2.2}$$

where Tr is the trace, $\boldsymbol{\epsilon}$ is the infinitesimal strain tensor, E is the Young's modulus, ν is Poisson's ratio, η is the tissue viscosity, $\boldsymbol{v} = \partial \boldsymbol{u}/\partial t$ is the velocity field, $\dot{\boldsymbol{\epsilon}}$ is the strain rate, and $\boldsymbol{I}$ is the identity tensor.

Discretization of Equation (2.1) with FEM is done using the well known displacement based variational formulation as described in [65, Chapters 4 and 6], so is only summarized here. Let $\boldsymbol{V}(\Omega)$ be the space of scalar piecewise linear functions defined over a triangulation (Figure 2.8) and $\boldsymbol{V}_0(\Omega) = \{\delta\boldsymbol{u} \in \boldsymbol{V}(\Omega) : \delta\boldsymbol{u} = 0 \,\text{on}\, \partial\Omega_{\text{dir}}\}$, be the same space but including a homogeneous boundary condition. According to the small displacement assumption, there is little difference between the reference and current configurations so that the two domains are equivalent [65, Section 6.2.1]. Approximating the displacements as $\boldsymbol{u} \in \boldsymbol{V}_0^2(\Omega)$, the displacement based FEM discretization follows a well-established procedure where Equation (2.1) is multiplied by a test function $\delta\boldsymbol{u} \in \boldsymbol{V}_0^2(\Omega)$, integrated over the domain, and integration by parts is conducted on the second order spatial derivative term (for example, see [65, Chapters 4 and 6]). This results in the system of equations

$$\begin{aligned}
&\int_\Omega \rho_{\text{vf}} \frac{\partial^2 \boldsymbol{u}}{\partial t^2} \cdot \delta\boldsymbol{u} - \boldsymbol{\sigma} : \delta\boldsymbol{\epsilon}\, d\boldsymbol{x} - \int_{\partial\Omega_{\text{med}}} \boldsymbol{t} \cdot \delta\boldsymbol{u}\, ds = 0 \\
&\text{for all } \delta\boldsymbol{u} \in \boldsymbol{V}_0^2(\Omega) \\
&\text{such that } Y_{\text{gap}} = Y_{\text{con}} - Y \geq 0 \text{ on } \partial\Omega_{\text{med}},
\end{aligned} \tag{2.3}$$

where : is the double dot product (for matrices (A, B), with components $(A_{i,j}, B_{i,j})$, $A{:}B = \sum_{i,j} A_{i,j}B_{i,j}$), $\delta\boldsymbol{\epsilon} = 1/2(\partial\delta\boldsymbol{u}/\partial\boldsymbol{x} + \partial\delta\boldsymbol{u}/\partial\boldsymbol{x}^{\intercal})$. The inequality on Y_{gap} enforces the contact conditions and leads to contact forces at the contact interface. There are a number of

methods to solve the contact constraints, such as the penalty method, Lagrange multipliers, or Augmented Lagragian methods each with different tradeoffs (see [60] for an introduction to contact mechanics). One intuitive approach is the penalty method where an additional contact traction is added during contact to minimize the constraint violation Y_{gap}. This is enforced by a traction term [60, Section 6.3]

$$\begin{aligned} \boldsymbol{t} &= -p_{\text{con}}\boldsymbol{n} \\ p_{\text{con}} &= \begin{cases} -k_{\text{con}} Y_{\text{gap}} & Y_{\text{gap}} > 0\,, \\ 0 & Y_{\text{gap}} \leq 0 \end{cases} \end{aligned} \tag{2.4}$$

where k_{con} is a contact spring with a large value chosen to minimize Y_{gap}. Equation (2.3) and the contact penalty spring define a system of ODEs that can then be integrated in time.

Numerous FEM models have been employed to model the VFs. One of the first FEM models was proposed by Alipour-Haghighi et al. [66] and consisted of a hybrid 2D/3D simulation. Their approach used multiple coronal slices of the VFs along the AP direction with each slice following a 2D linear elastic, plane strain, small deformation assumption simulated with FEM. Forces between adjacent slices were used to capture 3D effects. A Bernoulli based fluid model with acoustics was used to drive the model, allowing it to achieve self-sustained oscillation. Later studies have developed higher fidelity models, further elucidating the physics of VF oscillation. For example, Zheng et al. [67] developed a 2D FEM model and employed the immersed boundary method allowing high-fidelity fluid simulations to be used to drive the model. The same group later extended their method to a 3D FEM model assuming small deformations and linear viscoelasticity [68]. Their model captured the mucosal wave mode and predicted physiologically realistic flow rates. Other studies have used different modelling assumptions, including large deformations [63], and hyperelastic material behaviour [69].

Models based on FEM overcome many of the drawbacks of LMMs by treating the VFs as a continuum that is generally believed to better reflect the physics of VF motion [62, 66, 67, 70]. Parameters of continuum models such as linear elasticity, or geometry of the VF surface can be directly compared with real VFs, facilitating one-to-one comparisons. These benefits come with increased computational cost making the kinds of large parametric studies possible with LMMs difficult to achieve. However, increased computational cost can also be decreased through the different assumptions used in FEM models. For example, varying geometric dimensionality by simulating only a 2D coronal plane with the plane strain assumption, decreasing mesh density, or simplifications of the governing equations, such as assuming small deformations, and/or using simplified constitutive models of the

VFs all tend to decrease the cost of FEM models with a potential trade-off in the output fidelity.

2.2.2 Fluid models

Similar to solid models of the VFs, there are two broad approaches to modelling the glottal flow: 1D flow models (often taking the form of the steady Bernoulli equation) and flow models in 2D or 3D, which are typically viscous flow models based on the Navier-Stokes (NS) equations. These are further described in the following sections.

1D Fluid models

In 1D flow models the glottal flow is treated as 1D resulting in a flow domain as shown in Figure 2.9.

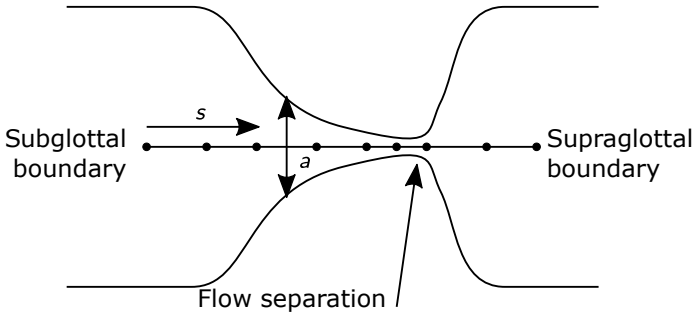

Figure 2.9: An example computational domain for a 1D flow model where the channel area is a and the 1D domain coordinate is s. Flow variables are discretized at the shown points

There are several variants of 1D flow models depending on additional assumptions made. One of the most common is to assume inviscid quasi-steady flow, which results in the Bernoulli equations,

$$p(s) = \begin{cases} p_{\text{sub}} + \frac{\rho_{\text{air}}}{2} q^2 \left(\frac{1}{a_{\text{sub}}^2} - \frac{1}{a(s)^2} \right) & s < s_{\text{sep}} \\ p_{\text{sep}} & s \geq s_{\text{sep}} \end{cases}, \tag{2.5}$$

$$q^2 = \frac{2}{\rho_{\text{air}}} \left(\frac{1}{a_{\text{sep}}^2} - \frac{1}{a_{\text{sub}}^2} \right)^{-1} (p_{\text{sub}} - p_{\text{sep}}), \tag{2.6}$$

where p is the pressure, q is the flow rate through the channel (constant for all sections due to mass conservation), a is the cross sectional area, a_{sub} and a_{sep} are areas at the subglottal and flow separation locations, p_{sub} and p_{sep} are subglottal and separation pressures, ρ_{air} is the air density, and s_{sep} is a point where flow separation occurs and thus Bernoulli no longer applies. This equation is derived by applying the Bernoulli formula between the subglottal boundary and a point s. Since 1D flow models cannot simulate flow separation directly, the separation point, s_{sep}, is usually set to occur when the area reaches an ad hoc ratio over the minimum glottal area such as $a_{\text{sep}}/a_{\text{min}} = 1.2$ [53], where a_{sep} is the area at separation and a_{min} is the minimum glottal area. Other 1D flow models have also been more recently proposed and can model viscous losses using the mechanical energy equation [71] or allow for both viscous losses and time dependent behaviour using the 1D Euler equations [69, 72, 73], based upon a model for flow through collapsible tubes by Cancelli and Pedley [74]. However, separation must still be specified in these more recent models. In general all the 1D models capture bulk phenomena of the glottal flow, such as the "Bernoulli effect" (pressure drops as speed increases in the constriction between the VFs), but do not naturally encode more complicated phenomena such as flow separation and turbulence. Modelling such phenomena require the addition of ad hoc or experimentally based laws.

Solution procedures for 1D flow models are generally simple due to the single spatial dimension. In the 1D Bernoulli flow model, the Bernoulli equation can be applied between the subglottal region and separation point to determine the glottal flow rate. The Bernoulli equation can then be used to solve for the pressure at any point in the glottal channel before separation. Past separation, the potential flow assumption no longer applies (Figure 2.9) and a constant separation pressure must be assumed instead. Slightly more complicated procedures must be applied for the alternative 1D fluid models, particularly those based on the 1D Euler equations since these are governed by 1D partial differential equations (PDEs). As a result, these models must be discretized in space using suitable methods such as the finite difference method, or FEM. If the flow is unsteady, a suitable time-discretization can then be applied, such as Runge-Kutta. Examples of solution procedures for these models are described in [69, 75].

One dimensional fluid models have been used extensively to simulate the glottal flow. Early attempts used the Bernoulli equation as a fluid model, such as Van den Berg who proposed it as the driving force behind sustained oscillation of the VFs according to the myoelastic aerodynamic theory [43]. Later, the Bernoulli model was extensively coupled to different LMMs [52, 54, 56]. These models were able to capture the mechanism by which fluid pressures from the glottal flow sustained oscillation of the VFs [56]. The Bernoulli approach has also been applied as a fluid model when coupled with continuum models of the VFs, with one of the first examples from Alipour-Haghighi and Scherer [76] whose model

was able to achieve self-sustained oscillation. Other studies have also coupled the Bernoulli model with continuum models to investigate a variety of phenomena. For example, Zhang [21] used linear stability analysis to investigate phonation threshold pressure of a Bernoulli driven 2D layered model, and Tao and Jiang [77] modelled AP biphonation, where the anterior and posterior parts of the VF vibrate at different frequencies. More recently, some authors have investigated alternative 1D flow formulations by solving the 1D Euler equations [69, 73, 75]. This formulation allows for modelling viscous losses, and unsteady effects, potentially improving the fidelity of the 1D approach.

One dimensional flow models are computationally inexpensive but are unable to capture complicated flow phenomena. The Bernoulli model, for example, is easily solved but only captures general trends in intraglottal pressures. This was shown by Decker and Thomson [71] who demonstrated that while the Bernoulli model can predict general VF motions that are similar to those predicted by a NS model, some quantities such as the peak glottal flow rate were over predicted by up to 50 %. Detailed flow phenomena such as flow separation, formation of turbulence in the glottal jet, and the effect of viscous boundary layers when the glottis is near closure can contribute to these differences and are not directly encoded by 1D flow models. These phenomena potentially play a large role in the fluid forcing [62] and also contribute sources of sound that are not predicted by 1D flow models [78].

2D and 3D Navier-Stokes models

In 2D and 3D models, the incompressible NS equations are typically solved due to the low Mach number of the glottal flow [35]. An example flow domain for a 2D model is illustrated in Figure 2.10.

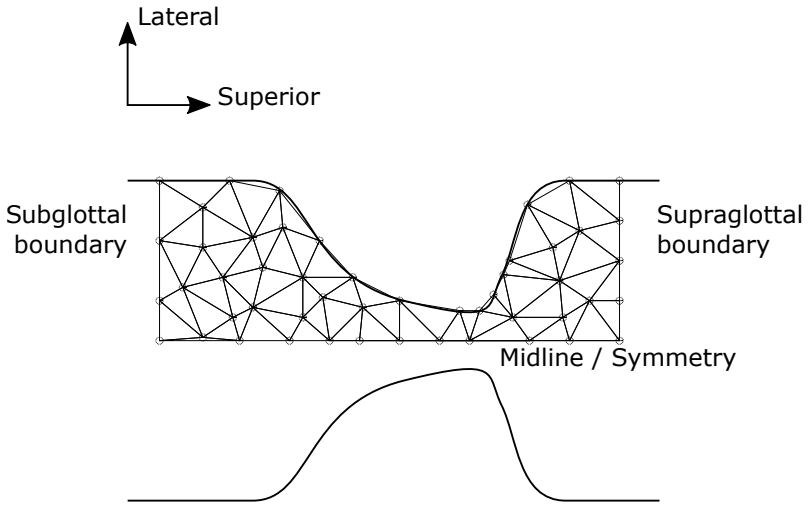

Figure 2.10: A 2D fluid domain in the coronal plane shown with an example mesh used to numerically solve the Navier-Stokes equations. A symmetry boundary condition is applied at the midline to simulate one half of the domain

There are few deviations in governing equations from the NS equations in the majority of 2D and 3D fluid models (see for example [64, 68, 79, 80]). Alternative 2D and 3D fluid models have been proposed, however, one notable example being the compressible NS equations, which also model the propagation of acoustic waves [78, 81]. Some authors have also proposed using Reynolds-averaged NS or large-eddy simulations that can help model turbulence without the fine mesh requirements of the NS equations [82].

Solution procedures for 2D and 3D flow models are often complex since discretization of the NS equations (compressible or incompressible) must be performed in 2D or 3D, increasing the number of discrete points representing the solution (see Figure 2.10 for an example discretization). Furthermore, the NS equations are computationally challenging to solve [35]. As a result, there are a large range of methods used to solve the NS equations; for a comprehensive review of these techniques, see a review of computational fluid dynamics [83]. For a few examples of solution methods, see [63, 64, 82].

Higher fidelity 2D and 3D fluid models have been extensively used to simulate the glottal flow. An early model was studied by Zhao et al. [78] and Zhang et al. [84] who simulated the compressible NS equations in a 2D static glottis configuration to identify sources of sound. Later studies coupled NS fluid models with continuum models of the VFs in order to capture self-sustained oscillations. Examples include Luo et al. [70] who used an immersed-boundary method to capture the 2D fluid-structure interaction between

a NS fluid model and continuum VF model, and Thomson et al. [79] who studied how energy is transferred from the glottal flow to the VFs, also using a 2D NS simulation coupled with 2D continuum VFs. More recent works have extended NS fluid models to 3D [64, 68, 82, 85, 86]. These models have captured complex physics of the glottal flow such as the formation of turbulence and asymmetric attachment of the glottal jet to either the left or right VF [68].

Two and three dimensional fluid models likely capture most of the pertinent physics of the glottal flow, but at the expense of high computational cost. Unlike 1D flow models, the governing equations (NS) naturally encode complex flow phenomena in the glottis, from flow separation to turbulence [67, 86]. This increased fidelity comes at the cost of increased computational expense since simulations of NS are typically difficult to conduct because the NS equations are complex and require a fine discretization to be solved accurately [82]. In addition, NS based fluid models typically represent the dominant cost when compared to the structural deformation of continuum VFs in coupled VF models [69]. These complex flow phenomena contribute additional sound sources [78] and also influence the motion of the VFs although the degree of influence likely depends on the specific case. Some works have suggested that 1D flow models compare reasonably with 2D NS based models in terms of VF motion [71]. If resolving such complex flow phenomena is the focus of the investigation, then high fidelity flow models should be used.

2.2.3 Acoustic models

Models of acoustics have mainly used two approaches: an approximation based on 1D acoustic waves and approaches from the field of aeroacoustics. These two approaches are further described in the following sections.

1D Acoustic models

All 1D acoustic models are based on simulation of the 1D acoustic wave equations [50]

$$\begin{aligned} \frac{\partial p}{\partial s} &= -\frac{\rho_{\text{air}}}{a}\frac{\partial q}{\partial t}, \\ \frac{\partial q}{\partial s} &= -\frac{a}{\rho_{\text{air}} c^2}\frac{\partial q}{\partial t}, \end{aligned} \tag{2.7}$$

where s is the 1D coordinate, p is the acoustic pressure, q the acoustic velocity, a the cross sectional area, ρ_{air} the air density, and c the speed of sound. Numerous boundary conditions

are possible, for example, a closed end of the 1D domain corresponds to $q = 0$ while an open end of the 1D domain corresponds to $p = 0$. More commonly, an end of the 1D domain will neither be perfectly open or closed and and impedance can be used to model frequency dependent relations between acoustic pressure and velocity at the boundary. The domain of the acoustic problem is illustrated in Figure 2.11 where the input flow rate comes from the glottis.

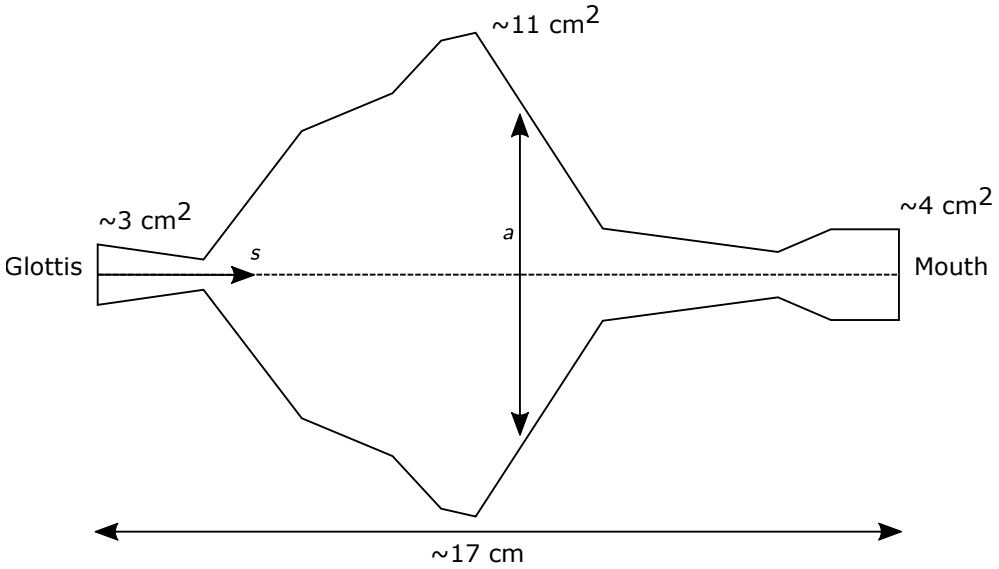

Figure 2.11: A 1D acoustic wave model domain for the supraglottal tract modelled after the /I/ sound from Fant [87]. The cross-sectional area is denoted by a and a coordinate along the tract length by s

At least three variations of 1D acoustic models exist, however, differing in the way the wave equations are solved. These are the electrical transmission line analog, direct discretization of the 1D acoustic wave equations (with a finite difference method, for example), as well as the wave-reflection analog (WRA) [88, pg. 10-20]. In the electrical transmission line analog method, the fact that governing equations of electrical transmission lines are analogous with those of 1D acoustic waves in Equation (2.7) (pressure is analogous to voltage and flow to current) is used to model the acoustics. Specifically, electrical transmission lines can be modelled using a lumped-element approach where the line is broken into discrete lengths modelled by "T-sections" consisting of basic electrical components (capacitors, inductors) [88] that represent the impedance of the given section of line. The varying area in the acoustic wave equations represents an analogous impedance

and can be converted to equivalent "T-sections" that model acoustic wave propagation [88]; see [89] for a more detailed description of this approach. The "T-section" approach was largely used to create physical electrical circuits modelling acoustics, however, can also be modelled on a computer. In the WRA approach, acoustic wave propagation is simulated through a system of discrete tubes with varying areas representing the varying area of the tract. Within each tube, the 1D acoustic wave equations apply (Equation (2.7)) while at tube junctions, continuity of acoustic pressure and flow applies. Continuity at junctions results in reflection and transmission of waves between adjacent tubes [88, pg. 16-20]. This model captures the basic 'filtering' effect of the vocal tract where the varying area of the vocal tract modulates the frequency distribution of the source sound; for further details of this approach see [88]. Finally, direct discretization of the 1D wave equations simply involves well known methods such as finite-differences or FEM that can be used to solve Equation (2.7) on a computer.

The three 1D acoustic model formulations are similar but have specific advantages in some scenarios. Electrical transmission line analogs were advantageous in early investigations since they can be physically constructed. As computers have become increasingly prevalent, however, these analogs seem to be employed less. The WRA approach and direct discretization of the 1D wave equations are both computational methods that have been employed to model the acoustics and are similar. The WRA approach, however, couples the number of discrete tubes and length of each tube with the time between reflections [88]. Specifically, if a tract contains N tubes, the length of tract will be $Nc\Delta t$. As a result, the integration time step Δt cannot be changed without changing the length of the tract. Direct discretization of Equation (2.7) can avoid this problem but involves the solution of a more computationally expensive system [88]. We note, however, the WRA seems to be the dominant approach for simulating 1D acoustics, see for example [38, 51, 54, 75, 80, 90].

Early models of acoustics often used the WRA model to simulate vowel sounds using assumed flow rate inputs [4, 91]. These studies successfully captured the filtering effect of different 'area functions' of the vocal tract and oronasal cavities that lead to different vowel sounds [4]. In later studies, WRA models were coupled with LMMs of phonation so that the time varying flow rate was supplied by the model of the glottis [54, 56, 88] thus simulating the production of sounds from the physical phonation process. Such models have also been used to determine the glottal flow rate based on measurements of the output speech waveform (known as inverse filtering) [92–94] (note that the flow rate at the mouth is modulated by the acoustic pressures in the tract so does not match the flow rate at the VFs).

Aeroacoustics

The second approach to acoustics involves modelling it from physical principles using techniques from the field of aeroacoustics [48]. In contrast to 1D acoustic approaches where the acoustic source comes from the time varying flow rate, aeroacoustic approaches aim to predict the generation of sound from all the potential sources of sound in the glottis such as, movement of the VF walls, turbulence in the glottal jet, and other features in the glottal flow [48]. Specific models or equations used to predict this include aeroacoustic analogies and direct numerical simulation of the compressible flow equations [78]. These models are more complicated than 1D approaches and often require advanced solution techniques [63, 78, 81, 95].

Aeroacoustic approaches to predicting sound generation in the glottis were first explored by McGowan [48], who noted that WRA type models only predict a 'monopole' source of sound. McGowan demonstrated that sound is also created through a 'dipole' source by the unsteady forcing of the VFs on the glottal flow. Later authors have further explored the aeroacoustic approach such as Zhao et al. [78] who calculated acoustic sources in a static glottal configuration using acoustic analogies and direct numerical simulation of compressible flow, or Link et al. [63] who used an acoustic analogy to develop a fluid-structure-acoustic interaction model.

2.2.4 Fluid-Structure-Acoustic coupling

The final aspect needed to describe a complete model of the VFs is the coupling between the 3 physical phenomena of fluid flow, solid deformations of the VFs, and acoustics. The coupling between solid and fluid is well-established and is based on the fact that forces and motions are equal at the interface [66, 67, 70]. Mathematically this is given by

$$\begin{aligned} \boldsymbol{\sigma}_{\text{solid}} \cdot \boldsymbol{n}_{\text{FSI}} &= \boldsymbol{\sigma}_{\text{fluid}} \cdot \boldsymbol{n}_{\text{FSI}} \\ \boldsymbol{u}_{\text{solid}} &= \boldsymbol{u}_{\text{fluid}}, \end{aligned} \tag{2.8}$$

where the conditions are applied at the fluid-solid interface (see $\partial\Omega_{\text{med}}$ in Figure 2.8).

Coupling between acoustic and fluid domains or acoustic and solid domains is comparatively less established and is still a topic of research (see for example [51, 63, 81, 95]). Theoretically, acoustic wave propagation is directly captured by the compressible fluid equations [63] meaning there are only two governing equations in phonation, those for the compressible fluid (capturing the glottal flow and acoustics) and those for the solid (VFs). As a result, acoustics, fluids, and the solid are simultaneously coupled where the

coupling between acoustics and fluids is implicit in the compressible flow equations. Direct simulation of the compressible flow equations to capture acoustics is computationally infeasible, however, due to the large disparity in scale between acoustic flow variables and the bulk flow variables [63]. As a result, most studies treat acoustics as a separate physical phenomena and couple the results with the fluid and/or solid domains. The degree of coupling between acoustics and the solid/fluid domains depends on the choice of acoustic model. In the case of 1D acoustic models, early approaches assumed a linear source-filter assumption meaning that the acoustic pressures have no effect on the source (glottal flow and VF motion) [88] (a one-way coupling from the glottal flow to the acoustics). Later works using 1D acoustic models proposed that the acoustic pressures can influence the source by changing the pressures at the subglottal and supraglottal boundaries of the glottal flow [18]. This coupling condition enforces that acoustic flow variables and bulk flow variables match at the interfaces (Figure 2.8). In this approach, the influence of acoustic pressures on the solid is indirectly captured through coupling with the fluid. Coupling methods using aeroacoustic models are quite complex due to the complexity of the approach but are likely to capture greater fidelity of the phonation process. For example, while the 1D wave reflection analog model considers the acoustic domains and glottal flow domains as distinct regions that interact at surfaces, aeroacoustic approaches involve overlapping acoustic and flow domains that interact throughout their shared volume [63]. This leads to simultaneous interactions between acoustic, fluid and solid domains that is likely more representative of the underlying physics [63]. We refer the reader to [63, 81, 95] for examples of this approach.

2.3 Dynamical systems interpretation of numerical models

A dynamical system is a system that evolves with time and is typically represented by the general formula for a non-linear ODE

$$\dot{X} = F(X; \lambda, P) \tag{2.9}$$

where X is the state of the system, $\dot{X}$ is the state's time derivative given by $F(X; \lambda, P)$, λ is some forcing parameter, such as the amplitude of an external force, and P is a vector of system parameters. Figure 2.12 illustrates an example dynamical system for a VF model consisting of a 1D fluid coupled with a lumped mass model representation of the VFs to demonstrate this.

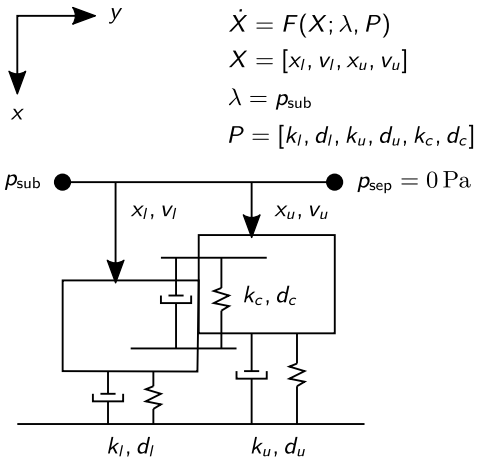

Figure 2.12: Conceptual representation of a vocal fold dynamical system for a two-mass model [52]

The state, X, consists of displacements and velocities of the VF tissue masses $(x_u, v_u, \ldots)$. The forcing parameter, λ, is the subglottal pressure, p_{sub}. The parameters, P, of the system consist of any additional parameters, such as the stiffness and damping of the VF tissue lumped masses $(k_u, d_u, \ldots)$. Note that more complicated models, such as those using FEM representations of the VFs are conceptually identical but usually have higher dimensional states.

2.3.1 Local bifurcations

An important concept in the study of dynamical systems is the phenomenon of local bifurcations, wherein an initially static dynamical system becomes unstable as the forcing parameter, λ, changes leading to a qualitative change in behaviour [96]. Examples of such phenomena are numerous and have important engineering applications. A classic example is in the buckling of slender beams. A beam loaded at its ends supports the load with compressive stresses; however, as the weight of the load increases the static state of the beam can lose stability resulting in buckling [96]. Another example is the phenomenon of vortex shedding behind a bluff body. At low flow speeds, fluid moves smoothly around the body; however, as the flow speed increases and reaches a critical value, the normally smooth stationary flow loses stability and begins to oscillate. As flow speed further increases, these oscillations appear as vortices shed behind the cylinder. Local bifurcations thus correspond to changes in stability of a static state as the system forcing parameter λ crosses a critical value.

Mathematically, local bifurcations of dynamical systems can be identified by considering the stability of a static state, or fixed point. The fixed-point is a static equilibrium state, X_{fp}, satisfying

$$0 = F(X_{\text{fp}}; \lambda, P). \tag{2.10}$$

The stability of the fixed-point is related to the evolution of small perturbations around it. This is characterized by the equation governing the linearized dynamics

$$\begin{aligned} (\dot{X_{\text{fp}}} + \dot{\Delta X}) &\approx F(X_{\text{fp}}; \lambda, P) + \left(\frac{\partial F}{\partial X}\right)_{X_{\text{fp}};\lambda,P} \Delta X \\ \dot{\Delta X} &= \left(\frac{\partial F}{\partial X}\right)_{X_{\text{fp}};\lambda,P} \Delta X \end{aligned} \tag{2.11}$$

where ΔX is a small perturbation to the fixed-point. Considering small perturbations of the form

$$\Delta X = A \exp((\omega_r + \omega_i j)t),$$

where A is a complex amplitude, ω the frequency of the oscillation, and subscripts $()_r, ()_i$ represent real and imaginary parts. Substituting this small perturbation into Equation (2.11) shows that the behaviour of perturbations with time corresponds to eigenvalues of the linearized dynamics operator $\partial F/\partial X(X_{\text{fp}}; \lambda, P)$

$$(\omega_r + \omega_i j)A = \left(\frac{\partial F}{\partial X}\right)_{X_{\text{fp}};\lambda,P} A. \tag{2.12}$$

The eigenvector, A, corresponds to the 'mode' of the perturbation while the eigenvalue $\omega_r + \omega_i j$ determines the mode's behaviour in time. The real part determines the growth of the perturbation. Perturbations with $\omega_r > 0$ grow exponentially with time while those with $\omega_r < 0$ damp exponentially. The imaginary part determines the frequency of the perturbation. Perturbations with $\omega_i = 0$ have no oscillation while those with $\omega_i \neq 0$ have an oscillatory frequency of $|\omega_i|$.

Local bifurcations are categorized by the type of instability that is triggered. For the buckling example described previously, the local bifurcation is termed a pitchfork bifurcation [96, Section 3.4]. In this type of bifurcation, a single fixed point representing the straight beam exists when the control parameter, λ, is less than a critical value. When the control parameter exceeds the critical value, the straight beam static state becomes unstable and two stable fixed points corresponding to buckling to the left and right appear [96, Section 3.4]. For the vortex shedding example described previously, the local bifurcation is termed a Hopf bifurcation [97]. For a Hopf bifurcation, a single stable fixed point exists

when the control parameter is less than the critical value. When the control parameter exceeds the critical value, the fixed point becomes unstable to an oscillatory perturbation [96, Section 8.2], which corresponds to the oscillatory flow seen in vortex-shedding.

2.4 Phonation onset

As described in Section 2.1 vibration of the vocal folds due to the glottal flow leads to the source sound in phonation; the fact that VFs undergo this self-oscillation can be understood from the perspective of dynamical systems as a type of instability and is known as phonation onset. Specifically, phonation onset refers to the condition where the subglottal pressure reaches a critical value such that the VFs begin to self-oscillate under driving pressures from the glottal flow and corresponds to a Hopf bifurcation [18]. This can be illustrated for the example VF model shown in Figure 2.12. Phonation onset occurs when λ reaches a critical value where a neutrally stable oscillatory mode occurs with growth rate $\omega_r = 0$ and frequency ω_i. When p_{sub} is below the critical value, the growth rate is less than 0 causing the VFs to remain stable; when p_{sub} is above the critical value the growth rate is positive and the initially static state becomes unstable to an oscillatory instability. The critical value λ where the oscillatory instability is neutrally stable is known as the phonation onset pressure while the frequency of the instability is the phonation onset frequency.

Phonation onset is important for at least two reasons. Firstly, phonation onset provides a dynamical systems explanation for why VFs self-oscillate during phonation; a type of local bifurcation leads to an oscillatory instability (See below for further explanation). Secondly, phonation onset pressure and phonation onset frequency have important implications for phonation. Phonation onset pressure is related to the 'effort' required to produce speech (high onset pressures require greater pressure from the lungs) while phonation onset frequency is closely related to the frequency of speech [18].

2.4.1 Numerical solution of phonation onset

There are numerous methods for solving for the form of the instability and critical value of the control parameter where a Hopf bifurcation (phonation onset) occurs. Two broad categories are guess-and-check type iterative methods and augmented equation methods.

In guess-and-check type methods, a guess for the critical value of the control parameter, λ, is first made. A fixed point is then solved for via Equation (2.10) and the stability of

the fixed point checked by checking eigenvalues in Equation (2.12). If all eigenvectors have negative real eigenvalues, then the fixed-point is stable while any eigenvalue having a positive real part implies the fixed-point is unstable. Based on the stability of the initial guess for λ, a new guess for the critical λ can be generated until a point where a single unstable eigenvalue satisfying $\omega_r \approx 0$ is found. This guess-and-check method can be performed, for example, using a bisection strategy where an unstable λ and stable λ are iteratively incremented to locate the critical λ. The unstable λ can also be found by computing stabilities over a range or grid of λ values.

In augmented equation methods, a set of non-linear equations characterizing a Hopf bifurcation is formulated that can then be solved using standard methods for non-linear equations. Generally these formulations consist of a coupled set of non-linear equations that simultaneously characterize the fixed-point, critical value of the control parameter (λ), unstable mode shape (eigenvector), and unstable mode frequency (eigenvalue). This is done by combining non-linear equations for the fixed-point, eigenvalue problem, and an eigenvector normalization condition. There are multiple equations that can be formulated depending on the specific strategies chosen to represent each condition (stability condition, fixed-point, etc.), potentially leading to different numerical behaviours. Griewank and Reddien [98], for example, used two equations to represent conditions on the real and imaginary parts of the unstable mode shape (eigenvector) while Roose and Hlavaček [99] combined these two equations into a single equation and also used a different eigenvector normalization condition. These slightly different formulations are generally equivalent but can potentially have different numerical behaviour under special conditions such as, when turning points are near a Hopf bifurcation [99]. Regardless of the specific form of the resulting non-linear system of equations, solutions can be found using standard methods such as Newton's method [98].

2.5 Vocal fold swelling

2.5.1 Physiology of fluid regulation and swelling in vocal folds

Fluid plays a critical role in many tissues of the body including the VFs, (with VF tissue consisting of about 80 % water [100]) and is regulated by fluid exchange between capillaries (blood), interstitial tissue (the spaces in the tissue), and the lymphatic system [101, Section 20.3] as shown schematically in Figure 2.13.

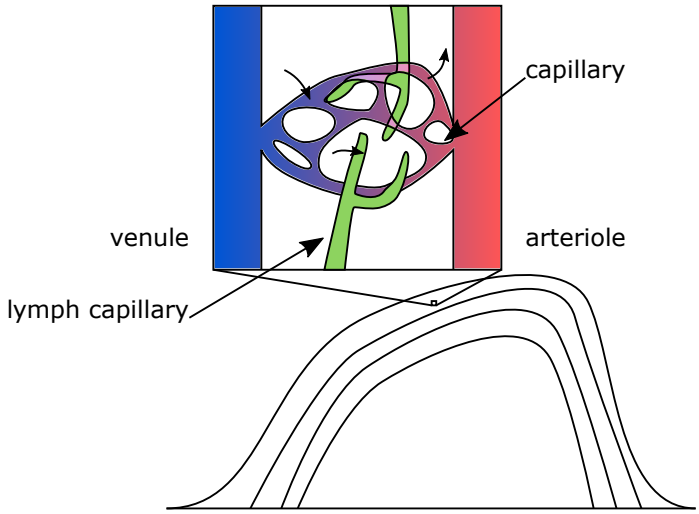

Figure 2.13: Schematic illustration of the micro-circulation system [102]. Directions of flow across the capillary boundary are denoted by lines with small arrowheads

The amount of fluid in tissue is kept constant by balancing the net inflow from the capillaries to the interstitial tissue with the net outflow from the interstitial tissue to the lymphatic network. Fluid exchange from the capillaries to the interstitial tissue happens due to a balance of mechanical (hydrostatic) and osmotic pressure differences between the capillary and interstitial fluid [101, Section 20.3]. While osmotic pressure differences tend to draw fluid from the tissue into the capillary to reduce the concentration of proteins in capillary fluid, hydrostatic pressure tends to drive flow from the capillary to the tissue since the capillary hydrostatic pressure exceeds that of the interstitial fluid. At the arterial end of the capillaries, the net hydrostatic pressure difference exceeds the osmotic pressure difference so net flow from the capillary to the tissue occurs. At the venous end of the capillaries, the net osmotic pressure difference exceeds the hydrostatic pressure difference so net flow from the tissue to the capillary occurs. The reversal in driving pressures at the venous end of the capillaries, is faciliated by loss of fluid as blood flows through the capillary that decreases capillary hydrostatic pressure and increases capillary osmotic pressure [101, Section 20.3]. The net direction of flow is from capillary to tissue since the flow from capillary to tissue at the arterial end exceeds the flow from tissue to capillary at the venous end [1]. The lymphatic system serves to drain this excess flow, estimated at about

[1]This description of reversed capillary flow rate directions at the arterial and venous ends of the capillaries is common in textbooks; however, recent evidence strongly suggests that this description is incomplete and that usually flow rate is directed outwards over the entire capillary length [103].

$4\,\mathrm{L\,d^{-1}}$ [103]. This system consists of a network of thin walled lymph tubes that channel the fluid away from the tissue; fluid is passively drained through these tubes through the action of smooth muscle contractions while flow back into the tissue is prevented by one way valves [101, Section 20.3].

The relation governing fluid transport between capillaries and interstitial tissue is given by Starling's equation [29, 104, 105]

$$Q = K(p_{\mathrm{cap}} - p_{\mathrm{isf}} - \sigma(\pi_{\mathrm{cap}} - \pi_{\mathrm{isf}})), \tag{2.13}$$

where Q is the fluid flux per unit area through the capillary wall into the interstitial fluid, p and π are the hydrostatic and osmotic pressures, respectively, and subscripts $(\cdot)_{\mathrm{isf}}$ and $(\cdot)_{\mathrm{cap}}$ represent interstitial and capillary quantities, respectively. Osmotic pressures, π, are related to concentration of solute (such as proteins, sugars) in the fluid. Material parameters are hydraulic conductivity, K, representing the resistance of the membrane to flow, and the reflection coefficient, σ, where $\sigma < 1$ accounts for imperfect semi-permeability of the membrane to solutes.

While the amount of fluid in tissue is constant under homestatic conditions, accumulation of fluid in the tissue, or swelling, can occur when the fluid flow rate balance between capillaries and interstitial tissue overcomes the normal lymphatic drainage rate [105]. From the perspective of Equation (2.13), swelling can be triggered through any process that varies one or more of the governing parameters K, σ, p, π. Different triggering factors (type of injury, disease) often induce swelling through different mechanisms (that is, changes in parameters of Starling's equation) [105]. For example, in the case of venous obstruction, capillary pressure, p_{cap}, is raised, increasing the flow from capillary to interstitial tissue thus causing swelling. In the case of inflammation, swelling is caused by increased capillary permeability (K, σ) that is facilitated by a breakdown in the endothelial barrier [105, 106]. In several inflammatory reactions Reed et al. [107] notes that a lowering of interstitial fluid pressure, p_{isf}, contributes to swelling. These processes cause transient increases in flow to the tissue but a steady state volume is eventually achieved in swelling through self-regulating mechanisms that balance the flow from the capillaries to the interstitial tissue and from the interstitial tissue to the lymphatic system. For example, as interstitial fluid volume increases, interstitial osmotic pressure drops due to lowered solute concentration while hydrostatic pressure increases due to compression by the surrounding tissue, both of which tend to limit further swelling [107, Section 6].

2.5.2 Mechanical effects of swelling

Swelling of tissues leads to altered mechanical properties, particularly tissue elasticity and viscosity. In the case of VFs, swelling results in softening of the material, as studies have shown that stiffening occurs with dehydration [108, 109]. The precise reason for the softening behaviour with swelling likely depends on the specific material; however, an explanation for softening with swelling in the context of rubbers can be explained by the statistical theory of the long chain molecules constituting rubber [110], and likely partially applies to biological materials that similarly contain fibrous proteins in the extracellular matrix [24, 111]. In rubbers, swelling decreases the number of molecular chains per unit volume and stretches them; further deformation from the swollen state then reduces the relative amount of energy stored in a unit volume by these molecular chains since there are fewer chains, thus resulting in a decrease in elasticity. Similarly, swelling changes viscous properties of the tissue although the precise reason why is not completely understood. Biphasic models suggest one reason is due to the changing fluid/solid fraction of the material [112], while other studies have suggested that changes in the organization of extracellular molecules with swelling may also influence the viscosity [113]. Regardless of the physical mechanisms, the quantitative change in elastic and viscous properties can be significant. For example, Chan and Tayama [108] reported tissue stiffness and viscosity increase by 4 to 7 times with dehydration in a hypertonic solution of 25 % sucrose. Lastly, swelling has an obvious effect on local mass and volume of the swollen area due to the influx of fluid that can alter the dynamics of moving tissues.

2.5.3 Continuum models of swelling

Models of swelling should capture the change in volume induced by fluid accumulation as well as the resulting changes in material properties. Modelling swelling directly from the framework of Starling's equation is a formidable task [29] and there are few continuum models that use this approach; instead, models of swelling typically capture simpler physical mechanisms or employ phenomenological approaches.

One physics-based model of swelling captures swelling induced by osmotic pressure gradients through a triphasic model [114] that includes mechanical, fluid, and electro-chemical effects. In this approach, solid, fluid, and ion phases (representing charged particles) form a set of coupled partial differential equations in a continuum. Swelling in this approach then results from fluid accumulating within the solid phase due to chemical and electrical effects from the ion phase. While this approach captures the physical mechanism of

swelling driven by osmotic pressure effects, the resulting equations are complex and have thus been relegated to models of geometrically simple problems [115].

An alternative phenomenological approach to modelling swelling was proposed by Tsai et al. [116] that avoids modelling the mechanisms that lead to swelling and instead prescribes the amount of swelling directly. This approach involves modifying a hyperelastic strain energy function $w(\boldsymbol{F})$, describing the original material, where $\boldsymbol{F}$ is the deformation gradient tensor, such that the new material 'prefers' a state that corresponds to the prescribed swelling, v, where v is the desired ratio of swollen to original volume. Assuming $\boldsymbol{F}$ is measured with respect to an unstrained and unswollen reference configuration, the original strain energy is minimized when $\boldsymbol{F} = \boldsymbol{I}$, corresponding to a zero deformation state. To ensure the swollen material's strain energy prefers equiaxial expansion (corresponding to swelling) as its minimal strain energy state, Tsai et al. [116] proposed the modified strain energy

$$\bar{w}(\boldsymbol{F}) = m(v)w(v^{-1/3}\boldsymbol{F}),$$

where $m(v)$ is a monotonic function satisfying $m(1) = 1$ that controls change in material stiffness with swelling. This extension ensures that the minimal strain energy state of the modified strain energy, $\bar{w}$, is $\boldsymbol{F} = v^{1/3}\boldsymbol{I}$, which corresponds to equiaxial expansion with volume change v. While this approach no longer captures the physical mechanisms driving swelling, it allows prescription of swelling based on phenomenological observations and exploration of the resulting impacts of swelling on the system.

Chapter 3

Sensitivity of phonation onset pressure to vocal fold stiffness distribution [1]

3.1 Introduction

This chapter explores the sensitivity of onset pressure to stiffness distributions to elucidate what stiffness distributions tend to increase onset pressure, and thus phonatory effort and risk for developing PVH. A sensitivity analysis using a 2^{nd} order Taylor model of onset pressure as a function of stiffness distributions is developed using a coupled VF model that predicts onset pressure. This Taylor model is then analyzed to determine what stiffness distributions have the greatest effect on onset pressure, and thus risk for developing PVH.

The chapter is organized as follows. Section 3.2 discusses the coupled VF model, the numerical method for computing phonation onset and the sensitivity analysis of phonation onset and frequency. Section 3.3 presents the results of the sensitivity analysis. Section 3.4 discusses the sensitivity analysis results and interprets the relative importance of BC and non-layered stiffness variations. Finally Section 3.5 summarizes the main conclusions and limitations.

[1] This work was co-authored by Sean D. Peterson. I developed the code, performed the simulations, analyzed data, generated figures, and wrote the first draft of the manuscript. SDP contributed to conceptualization, supervised the work, and reviewed the manuscript.

3.2 Methods

The implementation described herein is available online at the author's GitHub page and the lab GitHub page https://github.com/jon-deng/vf-fem or https://github.com/UWFluidFlowPhysicsGroup/vf-fem and https://github.com/jon-deng/vf-onset-sensitivity or https://github.com/UWFluidFlowPhysicsGroup/vf-onset-sensitivity.

3.2.1 Vocal fold and glottal flow models

The VF model consists of a two-dimensional (2D) finite-element method (FEM) based representation coupled with a 1D Bernoulli-based glottal flow model, as illustrated in Figure 3.1. Such a model configuration has been extensively used in past studies for both investigating the onset behaviour of the VFs [20–22] as well as for studies of transient VF motion [66, 117, 118]. The VF external geometry is based on the M5 geometry [119] and

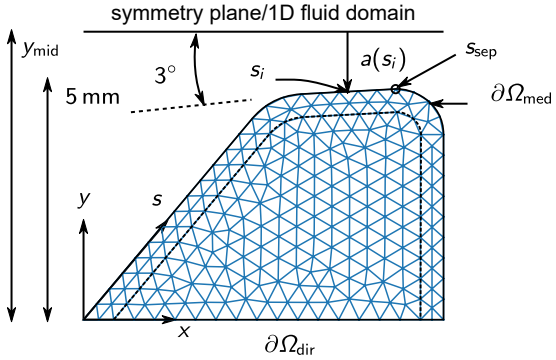

Figure 3.1: Schematic of the coupled vocal fold and glottal flow models. A dashed line delineates the typical body-cover layers

is shown in Figure 3.1 in the reference configuration with coordinates $\boldsymbol{X} = (x, y)$ and a surface coordinate along the medial surface s. Left-right symmetry about the medial plane at Y_{mid} is assumed, thus reducing the computational domain to a single fold.

The governing equations for the VF model are derived from the weak form of the conservation of linear momentum for small deformations using the standard approach for the displacement-based formulation (see [65, Section 4.2] for a detailed example). Displacement, $\boldsymbol{u}$, and velocity, $\boldsymbol{v}$, as well as their time derivatives, $(\dot{\boldsymbol{u}}, \dot{\boldsymbol{v}})$, are approximated in a vector-valued piecewise linear function space, $\boldsymbol{V}^2(\Omega)$, while the stiffness field, E, is approximated in a cellwise constant function space, $\boldsymbol{W}(\Omega)$, where Ω and $\partial\Omega$ are the VF domain

and boundary (see Figure 3.1). The infinitesimal strain tensor and deformation gradient are given by $\boldsymbol{\epsilon} = 1/2(\partial \boldsymbol{u}/\partial \boldsymbol{X} + \partial \boldsymbol{u}/\partial \boldsymbol{X}^\intercal)$ and $\boldsymbol{F} = \boldsymbol{I} + \partial \boldsymbol{u}/\partial \boldsymbol{X}$, respectively, where $\boldsymbol{I}$ is the identity tensor. The medial surface pressure $p \in \boldsymbol{V}(\Omega)$ is given by the glottal flow. The resulting residual equations for the conservation of linear momentum are given by

$$\begin{aligned} f_{\boldsymbol{u}}(\boldsymbol{u}, \boldsymbol{v}, \dot{\boldsymbol{v}}, p, E; \delta \boldsymbol{u}) = &\int_\Omega \rho \dot{\boldsymbol{v}} \cdot \delta \boldsymbol{u} + \boldsymbol{\sigma}(\boldsymbol{\epsilon}, \dot{\boldsymbol{\epsilon}}; E) : \delta \boldsymbol{\epsilon} \, d\boldsymbol{X} \\ &- \int_{\partial \Omega_{\text{med}}} -p \det \boldsymbol{F} \boldsymbol{F}^{-\intercal} \boldsymbol{n} \cdot \delta \boldsymbol{u} \, ds, \end{aligned} \tag{3.1a}$$

$$f_{\boldsymbol{v}}(\boldsymbol{v}, \dot{\boldsymbol{u}}; \delta \boldsymbol{v}) = \int_\Omega (\dot{\boldsymbol{u}} - \boldsymbol{v}) \cdot \delta \boldsymbol{v}, \tag{3.1b}$$

where $\delta \boldsymbol{u} \in \boldsymbol{V}^2(\Omega)$ and $\delta \boldsymbol{v} \in \boldsymbol{V}^2(\Omega)$ are test functions, $\delta \boldsymbol{\epsilon} = 1/2(\partial \delta \boldsymbol{u}/\partial \boldsymbol{X} + \partial \delta \boldsymbol{u}/\partial \boldsymbol{X}^\intercal)$ is the virtual strain, and $\boldsymbol{n}$ is the medial surface outward pointing normal vector. Solution of these equations for an unknown $(\dot{\boldsymbol{u}}, \dot{\boldsymbol{v}})$ with known remaining parameters requires finding $(\dot{\boldsymbol{u}}, \dot{\boldsymbol{v}})$ such that $(f_{\boldsymbol{u}}, f_{\boldsymbol{v}}) = 0$ for all $\delta \boldsymbol{u}, \delta \boldsymbol{v} \in \boldsymbol{V}^2(\Omega)$. For the Cauchy stress tensor, $\boldsymbol{\sigma}$, we assume a Kelvin-Voigt viscoelastic material [67, 120] resulting in the constitutive equation

$$\boldsymbol{\sigma}(\boldsymbol{\epsilon}, \dot{\boldsymbol{\epsilon}}; E) = \frac{E\nu}{(1+\nu)(1-2\nu)} (\text{Tr}\boldsymbol{\epsilon}) \boldsymbol{I} + \frac{E}{1+\nu} \boldsymbol{\epsilon} + \eta \dot{\boldsymbol{\epsilon}},$$

where $\text{Tr}(\cdot)$ is the tensor trace, ν is Poisson's ratio, and η is viscosity. The combined set of two equations form a non-linear residual representing an ordinary differential equation governing the dynamics of the VFs through a relationship between the state $(\boldsymbol{u}, \boldsymbol{v})$ and the state's time derivative $(\dot{\boldsymbol{u}}, \dot{\boldsymbol{v}})$.

The glottal flow is given by a Bernoulli-based model with a prescribed separation point. The Bernoulli pressure, p_{b}, and flow rate, q_{b}, are given by

$$p_b(s, p_{\text{sub}}) = \begin{cases} p_{\text{sub}} + \frac{\rho_{\text{air}}}{2} q^2 \left(a_{\text{sub}}^{-2} - a(s)^{-2} \right) & s < s_{\text{sep}} \\ p_{\text{sep}} & s \geq s_{\text{sep}} \end{cases}, \tag{3.2}$$

$$q_b^2 = \frac{2}{\rho_{\text{air}}} (p_{\text{sub}} - p_{\text{sep}}) \left(a(s_{\text{sep}})^{-2} - a_{\text{sub}}^{-2} \right)^{-1}, \tag{3.3}$$

where a is the channel cross-sectional area (see Figure 3.1), ρ_{air} the air density, p_{sub} the subglottal pressure, p_{sep} the pressure at the location of prescribed flow separation, s_{sep} (a fixed vertex shown in Figure 3.1), and $a_{\text{sub}} = \infty$ is the subglottal area.

3.2.2 Numerical solution

Equation (3.1a) and Equation (3.1b), are discretized into a matrix form by a FEM assembly procedure using coefficients of the functions with respect to a basis, which we implemented using the FEM library FEniCS [121, 122]. Let a basis of hat functions for $\boldsymbol{V}^2(\Omega)$ be given by $\{\boldsymbol{\phi}_i\}_{i=1}^{2n}$, where n is the total number of vertices (two hat functions associated with each 2D vector component are present for each vertex), and a basis for $\boldsymbol{W}(\Omega)$ be given by $\{\psi_i\}_{i=1}^{m}$, where m is the total number of cells (one function is associated with each cell centre). The functions are then represented as $\boldsymbol{u} = \sum_{i=1}^{2n} U[i]\boldsymbol{\phi}_i$ (with similar definitions for the velocity), $p = \sum_{i=1}^{n} P[i]\phi_i$, and $E = \sum_{i=1}^{m} E[i]\psi_i$, where $(\cdot)[i]$ denotes the i^{th} entry of the vector. The discretized residual then corresponds to a column vector with one entry for each test basis function and depends on coefficients of the state and stiffness

$$F_U[i] = f_{\boldsymbol{u}}(\boldsymbol{u}, \boldsymbol{v}, \dot{\boldsymbol{v}}, p, E; \boldsymbol{\phi}_i) \tag{3.4a}$$

$$F_V[i] = \dot{U}[i] - V[i]. \tag{3.4b}$$

Similar to the VF model, we can derive a matrix representation of the glottal flow equation residuals. Because the Bernoulli equations can be solved explicitly for the pressure at every medial surface node, the residual form simply involves evaluating Equation (3.2) and Equation (3.3) at vertices

$$F_P[i] = P[i] - p_{\text{b}}(s_i, p_{\text{sub}}), \tag{3.5}$$

$$F_Q = Q - q_b. \tag{3.6}$$

where Q, P are vectors of coefficients for the discretized flow rate and pressure. In the case of flow rate, which is a single scalar, Q is a vector with a single entry.

Combining the residuals for both VF and glottal flow results in a dynamical system for the coupled model with a combined state, X, represented in block form as

$$F(X, \dot{X}; E, p_{\text{sub}}) = \begin{pmatrix} F_U & F_V & F_Q & F_P \end{pmatrix}^\intercal, \tag{3.7}$$

$$X = \begin{pmatrix} U & V & Q & P \end{pmatrix}^\intercal. \tag{3.8}$$

The glottal flow and VF residual are coupled through the glottal area, a, and glottal flow pressure, p, respectively.

Fixed parameters for the model were chosen based on past studies and physiological measurements [66, 123], and are summarized in Table 3.1. The symmetry plane location, Y_{mid}, results in a prephonatory gap of 1 mm and was chosen to reduce the effects of the separation point model as further described in Appendix A.2.

Table 3.1: Constant parameters for the coupled model

Parameter	Value
ρ	$1\,\mathrm{g/cm^3}$
ν	0.45
η	5 poise
Y_{mid}	0.55 cm (see Figure 3.1)
p_{sep}	0 Pa
ρ_{air}	$1.293 \times 10^{-3}\,\mathrm{g/cm^3}$

3.2.3 Taylor model of phonation onset pressure

To determine when phonation onset occurs, the system residual (Equation (3.7)) is augmented by the system of equations proposed by Griewank and Reddien [98], henceforth referred to as the Griewank-Reddien equations. This approach has been applied in past studies to investigate Hopf bifurcations in physical phenomena such as vortex shedding [97, 124]. Here we outline the final equations from the sensitivity model; further details on how we computed these are given in Appendix A.1.

Using the Griewank-Reddien equations we compute a second-order Taylor approximation of onset pressure with respect to stiffness distribution [125],

$$p_{\mathrm{on}} \approx p_{\mathrm{on}}(E_0) + \frac{\partial p_{\mathrm{on}}}{\partial E}(E - E_0) + \frac{1}{2}(E - E_0)^{\intercal}\frac{\partial^2 p_{\mathrm{on}}}{\partial E^2}(E - E_0), \tag{3.9}$$

where E_0 is the stiffness linearization point, p_{on} is the onset pressure, $\partial p_{\mathrm{on}}/\partial E$ is the first order sensitivity to stiffness and $\partial^2 p_{\mathrm{on}}/\partial E^2$ is the second order sensitivity. We further decompose this Taylor model using an eigenvalue decomposition of $\partial^2 p_{\mathrm{on}}/\partial E^2$ and by locating a minimum onset pressure. The Taylor model can then be expressed in the form

$$p_{\mathrm{on}} \approx {p_{\mathrm{on}}}^* + \sum_{i=1}^{n} \Lambda_i \left(\Delta {E_i}^{\intercal}(E - E^*)\right)^2 + \Lambda_0 \Delta {E_0}^{\intercal}(E - E^*), \tag{3.10}$$

where ΔE_i and Λ_i $(i \geq 1)$ are eigenvectors and eigenvalues of $\partial^2 p_{\mathrm{on}}/\partial E^2$, ordered by descending absolute value, respectively, and a superscript $(\cdot)^*$ indicates the critical point where $(\partial p_{\mathrm{on}}/\partial E)_{E^*} = 0$ (see Appendix A.2 for details). Eigenvectors are normalized such that $||\Delta E_i||_2 = \sqrt{\sum_{k=1}^{n} (\Delta E_i[k])^2} = 1$. The terms ΔE_0 and Λ_0 denote a normalized gradient, $(\partial p_{\mathrm{on}}/\partial E)/||\partial p_{\mathrm{on}}/\partial E||_2$, and its norm, $||\partial p_{\mathrm{on}}/\partial E||_2$, (see Appendix A.2 for details).

Eigenvectors corresponding to eigenvalues with large absolute values represent stiffness perturbations that have large quadratic effects on onset pressure.

To compare the effects of smooth non-layered stiffness variations against idealized layered stiffness variations on onset pressure, we project the onset pressure sensitivity results onto various subspaces as illustrated in Figure 3.2. The three considered subspaces then

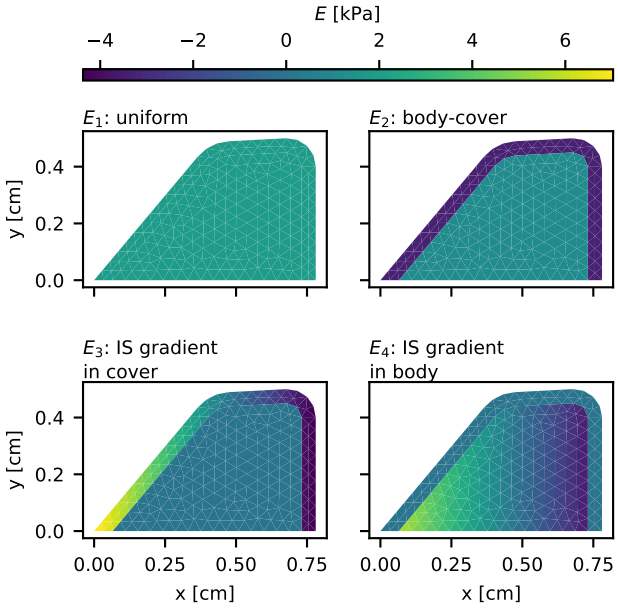

Figure 3.2: Structured basis vectors representing different idealized stiffness variations commonly used to represent vocal fold stiffnesses. The structured basis vectors capture changes in bulk stiffness (E_1), body-cover stiffness differences (E_2), and inferior-superior stiffness gradients in the cover (E_3), and body (E_4) layers, respectively

consists of spans of different sets of basis vectors, as summarized in Table 3.2. For each subspace we determine the restricted sensitivity by considering projected gradients and Hessians with the orthogonal projector for the subspace

$$P = AA^\intercal,$$

where A is a matrix with columns consisting of orthogonal vectors spanning the subspace.

Table 3.2: Summary of layered stiffness subspaces

Name	Basis vectors	Description
BC	(E_1, E_2)	variable body and cover stiffness
BC-C	(E_1, E_2, E_3)	variable body and cover stiffness with an IS gradient in the cover
BC-CB	(E_1, E_2, E_3, E_4)	variable body and cover stiffness with IS gradients in the cover and body
non-layered		full dimensional subspace with variable stiffness for each cell

The projected gradient and Hessian are given by

$$\begin{aligned}\frac{\partial G}{\partial E}_P &= \frac{\partial G}{\partial E}P,\\ \frac{\partial^2 G}{\partial E^2}_P &= P\frac{\partial^2 G}{\partial E^2}P,\end{aligned}$$

where $(\cdot)_P$ denotes the projected version of a sensitivity. These represent the sensitivities when stiffness perturbations are constrained to a subspace.

Comparing the effect of different stiffness perturbations on onset pressure also depends on the stiffness perturbation's magnitude, which depends on the norm being used. Consider travelling along an eigenvector, $\alpha\widehat{\Delta E_i}$, with step size α, where the eigenvector is normalized such that $\widehat{\Delta E_i} = \Delta E_i/||\Delta E_i|| = 1$ and $||\cdot||$ is a generic norm. Substitution into Equation (3.10) results in

$$\begin{aligned}p_{\text{on}} - {p_{\text{on}}}^* &\approx (\Lambda_i)\left(\Delta {E_i}^\intercal \alpha\widehat{\Delta E_i}\right)^2 + \Lambda_0 \Delta {E_0}^\intercal \alpha\widehat{\Delta E_i}\\ &= \frac{\Lambda_i}{||\Delta E_i||^2}\alpha^2 + \Lambda_0 \Delta {E_0}^\intercal \widehat{\Delta E_i}\alpha.\end{aligned} \tag{3.11}$$

Along this direction, the curvature with respect to α then appears to be

$$\Lambda_i / ||\Delta E_i||^2. \tag{3.12}$$

Therefore, to illustrate the effect of different norms, we compute these norm-adjusted eigenvalues for two norms defined by

$$||\Delta E||_{l_2(\Omega)} = \sqrt{\int_\Omega \left(\sum_{i=1}^{m} E[i]\psi_i \right)^2 d\boldsymbol{X}} \tag{3.13}$$

$$||\Delta E||_\infty = \max_i |\Delta E[i]|. \tag{3.14}$$

The former represents an integral of squared stiffnesses over the VF, while the latter is the largest created stiffness difference.

3.3 Results

3.3.1 Onset pressure sensitivity models for non-layered stiffness variations

This section presents sensitivity models for onset pressure at two different linearization points. Each linearization point, E_0, consists of discrete moduli in the body and cover regions (E_b, E_c). A total of 4 body to cover stiffness ratios of 1:1, 2:1, 3:1, and 4:1 were considered for $E_\text{b} = 6\,\text{kPa}$. Only the 1:1 and 2:1 cases are shown herein for brevity, as other cases showed similar qualitative features.

Figure 3.3 shows the 2$^{\text{nd}}$ order Taylor model described in Equation (3.10) at the 1:1 linearization point $E_0 = (E_\text{b}, E_\text{c}) = (6\,\text{kPa}, 6\,\text{kPa})$. Figure 3.3 A shows the resulting quadratic contours in onset pressure as a function of stiffness. Stiffness changes are represented by perturbations along the most significant eigenvectors, $\Delta E_1, \Delta E_2$ (Figure 3.3 B), about the critical point E^* (Figure 3.3 C), which are determined as explained in Appendix A.1. The larger the associated eigenvalue, the greater the curvature apparent in the onset pressure contours. The linear trend in onset pressure with stiffness change is given by $\Delta E_0, \Lambda_0$ but is not captured in the contours since the two dimensions both illustrate quadratic effects. Perturbations in stiffness along the ΔE_0 direction would simply shift each pictured pressure contour by a constant value. Finally, the linearization point, E_0, is also shown as a point in the onset pressure contours and the corresponding stiffness distribution shown in Figure 3.3 C.

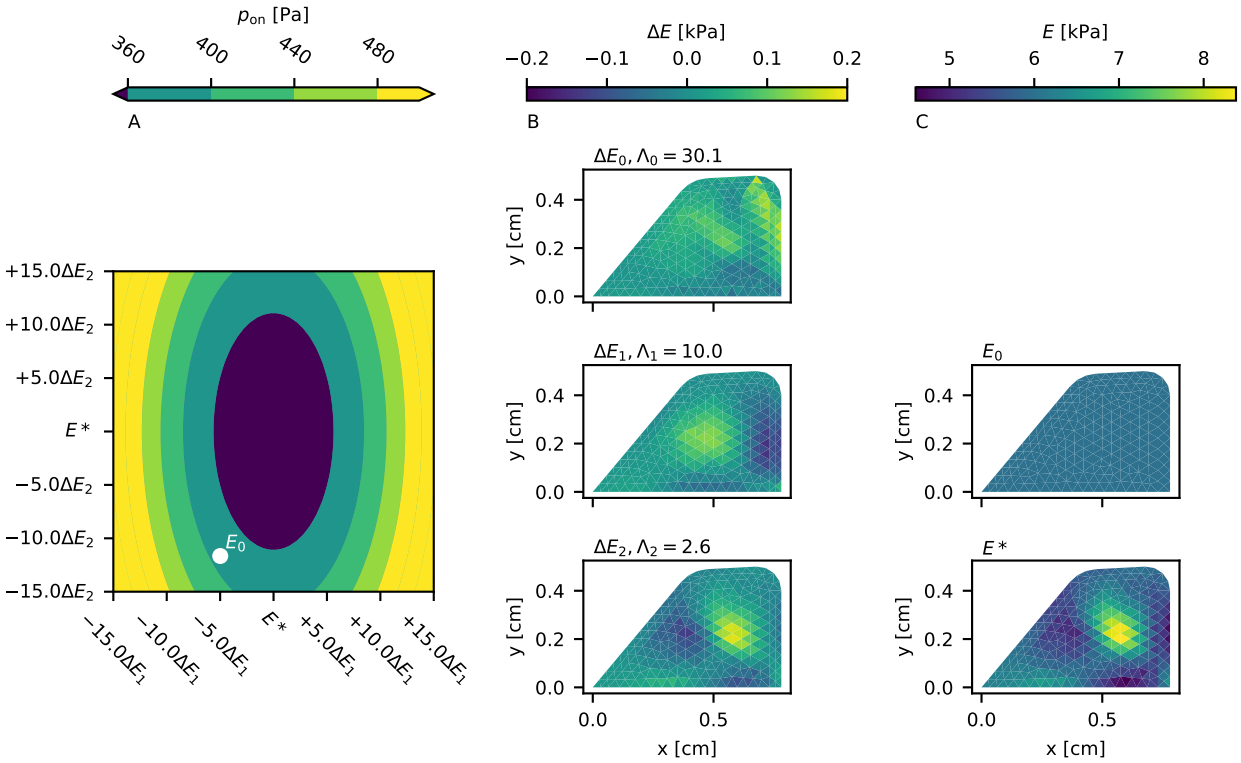

Figure 3.3: Taylor model of onset pressure for the linearization point $(E_b, E_c) = (6\,\text{kPa}, 6\,\text{kPa})$. Columns depict, (A) contours of onset pressure along significant orthogonal stiffness perturbations (B) orthogonal stiffness perturbations, and (C) the linearization and critical points

The two smooth eigenvectors, $(\Delta E_1, \Delta E_2)$, pictured were found to have the strongest effect on onset pressure, with remaining eigenvectors having smaller associated eigenvalues (low curvature) and high spatial frequencies in stiffness. These were deemed to be non-physical as further described in Appendix A.2. Interestingly, although we did not a priori prescribe the stiffness to vary in any particular manner, the eigenvectors qualitatively resemble reported variations in VF stiffness. The most impactful direction, ΔE_1, roughly creates stiffness differences between a 'body' and 'cover' region along with smooth gradients in stiffness in the IS and ML directions. As such, this eigenvector is referred to herein as BC-like. The second most impactful direction, ΔE_2, roughly creates stiffness differences between the inferior and superior aspects of the 'body'. Such a stiffness gradient has not been reported in literature although could exist since internal stiffness variations are diffi-

cult to measure in practice. Because both the eigenvectors have positive eigenvalues, the Taylor model shows that the critical point, E^*, minimizes onset pressure.

Figure 3.4 shows a similar Taylor model but for the 2:1 linearization point $E_0 = (E_b, E_c) = (6\,\text{kPa}, 3\,\text{kPa})$. While small differences exist compared to Figure 3.3 due to

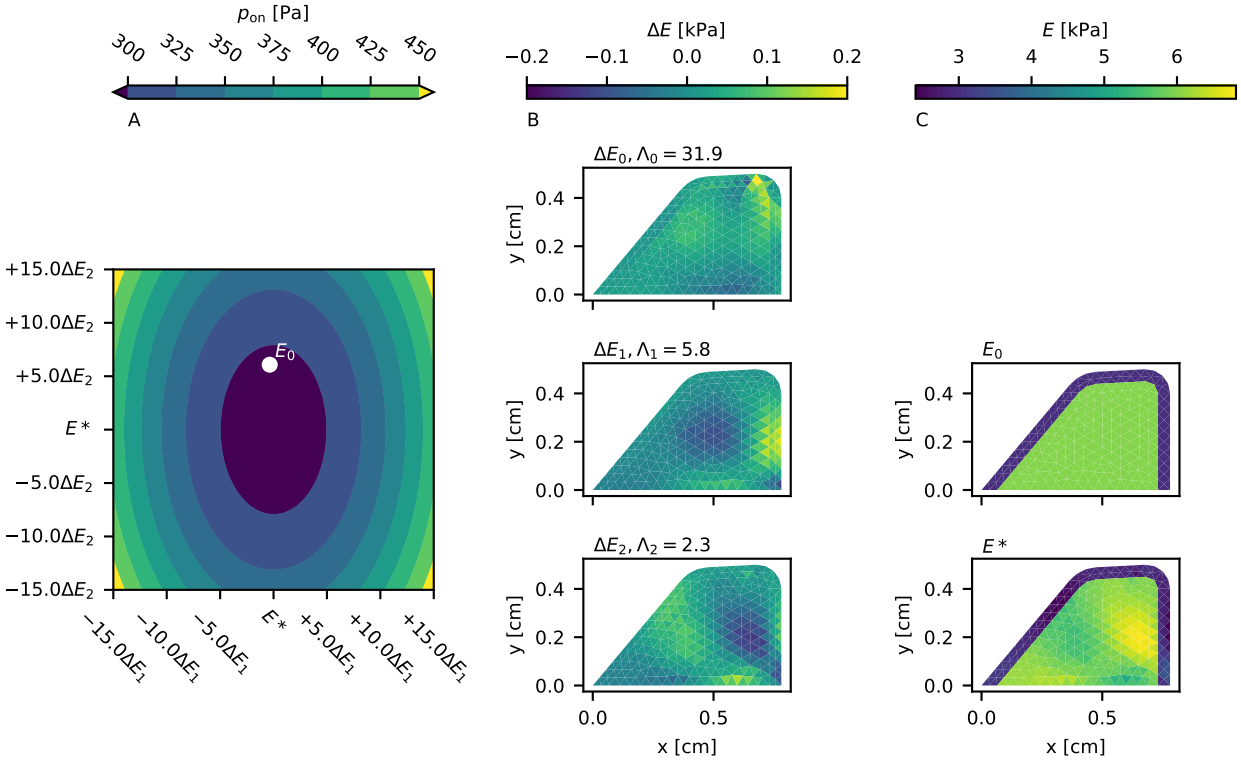

Figure 3.4: Taylor model of onset pressure for the linearization point $(E_b, E_c) = (6\,\text{kPa}, 3\,\text{kPa})$. Columns depict, (A) contours of onset pressure along significant orthogonal stiffness perturbations (B) orthogonal stiffness perturbations, and (C) the linearization and critical points

the different linearization point, the two cases share many qualitative similarities. For example, the two eigenvectors show similar stiffness distributions (BC-like and IS-like) and have associated positive curvatures. Quantitatively, eigenvalue magnitudes are reduced compared to those in Figure 3.3, indicating lower sensitivity of the critical value to the eigenvector directions. Finally, there are obvious differences in the linearization and critical points between the two cases.

Similarly, for both linearization points, the linear effect on onset pressure consists of

qualitatively similar stiffness perturbations along ΔE_0 (comparing ΔE_0 between Figure 3.3 B and Figure 3.4 B, both stiffness perturbations roughly involve increasing stiffness by about 0.1 kPa throughout the VF). For either linearization point, the linear effect direction roughly represents a uniform increase in stiffness. Since increasing the stiffness of a material tends to increase natural frequency, this linear increase in onset pressure along uniform-like stiffnesses is linked to associated increases in onset frequency. Uniform-like stiffness variations can be roughly related to increases in tension through the entire VF, such as by cricothyroid muscle activation which tenses and lengthens the entire VF [3].

The largest difference between the two linearization points is in the critical stiffness, E^*, which minimizes onset pressure. While Figure 3.3 C shows a smooth critical distribution, Figure 3.4 C shows a layered discontinuity in the critical stiffness, due to the layered linearization point. Additionally, while the critical point in Figure 3.3 A involves perturbations along both ΔE_1 and ΔE_2, the critical point in Figure 3.4 A involves a perturbation primarily along ΔE_2 (E_0 is approximately located at E^* along the ΔE_2 axis). This is likely due to the shifted linearization point. The Taylor model for the uniform linearization point (Figure 3.3) shows that a body to cover stiffness ratio of roughly 2:1 (in an average sense) is required to minimize onset pressure from the uniform stiffness distribution. This is qualitatively seen since E^* in Figure 3.3 has a stiffness of about 8 kPa in the core body region, and a stiffness of about 5 kPa in the outer cover region. Since the second linearization point (Figure 3.4) already achieves this ratio, no BC stiffness change is required and so no perturbation along ΔE_1 arises. Similarly, for the 3:1 linearization point, $E_0 = (E_\mathrm{b}, E_\mathrm{c}) = (6\,\mathrm{kPa}, 2\,\mathrm{kPa})$ (not shown), we found the critical distribution required stiffening the cover and loosening the body by moving along the ΔE_1 direction, consistent with the finding that a 2:1 stiffness ratio minimizes onset pressure.

3.3.2 Onset pressure models for layered stiffness variations

Figure 3.5 shows the onset pressure Taylor model at the linearization point $E_0 = (E_\mathrm{b}, E_\mathrm{c}) = (6\,\mathrm{kPa}, 6\,\mathrm{kPa})$ when stiffness perturbations are projected to the layered subspace. Although sensitivity models for all subspaces in Table 3.2 were computed, only the model for BC-CB is shown since results for all subspaces were qualitatively similar. Similar to the sensitivity models for the unrestricted stiffness variations (Figure 3.3), Figure 3.5 A shows contours of onset pressure, albeit with different axes. Whereas Figure 3.3 A has axes $(\Delta E_1, \Delta E_2)$ (both associated with quadratic effects on onset pressure), Figure 3.5 A has axes $(\Delta E_0, \Delta E_1)$ (associated with one linear and one quadratic effect on onset pressure, respectively). This is because only a single significant eigenvector was found for the layered subspaces, as

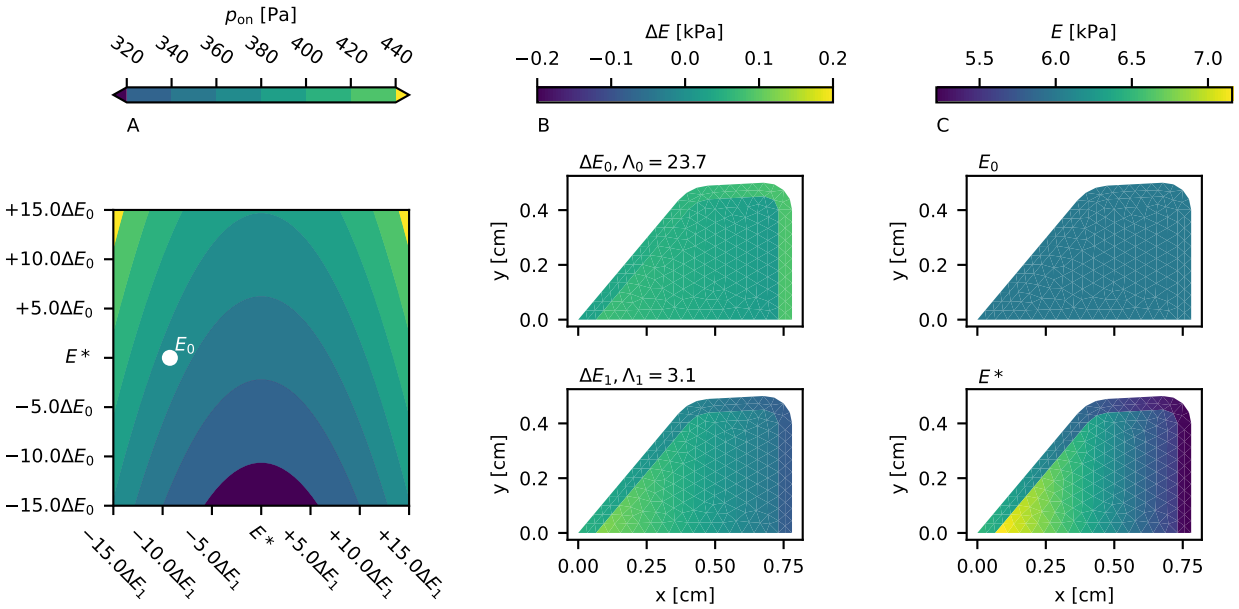

Figure 3.5: Taylor model of onset pressure for the linearization point $(E_b, E_c) = (6\,\text{kPa}, 6\,\text{kPa})$. Columns depict, (A) contours of onset pressure along significant orthogonal stiffness perturbations (B) orthogonal stiffness perturbations, and (C) the linearization and critical points The stiffness variations are constrained to vectors in the subspace 'BC-CB'

shown in Figure 3.5 B. Figure 3.5 C presents the linearization and critical points. Due to the subspace restriction, these points show purely layered stiffnesses.

There are a few qualitative similarities between the Taylor model in Figure 3.5 and the one for arbitrary stiffness variations (Figure 3.3). In both cases, the linear trend in onset pressure, ΔE_0, involves a nearly uniform increase in stiffness. The most significant eigenvector, ΔE_1, is also similar between the two. In both cases perturbing stiffness along this eigenvector creates a BC stiffness difference with gradients in stiffness along the IS direction. Finally, in both cases, the critical point, E^*, clearly corresponds to a stiffer body and looser cover along with an IS gradient in the body and cover layers, where stiffness decreases towards the superior end.

There are notable differences between the sensitivity models for arbitrary stiffness (Figure 3.3) and layered stiffness variations (Figure 3.5), however. The most obvious difference is that eigenvectors and critical points for the layered subspace show only layered variations, which is a consequence of the subspace choice. Furthermore, while the case with a non-layered basis (Figure 3.3) showed two eigenpairs with significant eigenvalues, when

stiffness variations are restricted to a layered subspace, we find that only one eigenpair is significant. The reason this occurs is likely because the layered subspace cannot represent the IS-like stiffness perturbation (ΔE_2 in Figure 3.3) which contains stiffness changes within the body layer. As a result the minimum onset pressure at the critical point also changes for the layered subspace.

Table 3.3 summarizes differences in eigenvalues and the minimum onset pressure achievable for each of the subspaces given in Table 3.2. As seen in Figure 3.5 only a single eigen-

Table 3.3: Comparison of eigenvalue magnitudes and minimum onset pressures when stiffness is constrained to different subspaces, for the linearization point $(E_\mathrm{b}, E_\mathrm{c}) = (6\,\mathrm{kPa}, 6\,\mathrm{kPa})$. Note the onset pressure at this linearization point is 358 Pa

Basis	Λ_1	Λ_2	${p_\mathrm{on}}^*$ [Pa]	$p_{\mathrm{on},0} - {p_\mathrm{on}}^*$ [Pa]
unstructured	10.0	2.6	328.5	29.8
BC-CB	3.1		345.2	13.1
BC-C	1.6		336.1	22.2
BC	0.8		337.3	21.0

pair is significant for the layered subspace. The most notable difference is that a priori layered subspaces have greatly reduced eigenvalue magnitudes. This indicates that variations in onset pressure are decreased when stiffness is restricted to idealized layers; for example, for the same magnitude step along an eigenvector direction, a smooth distribution decreases onset pressure over 10 times more compared to a pure BC perturbation (the ratio of Λ_1 for the unstructured subspace to the BC subspace). Correspondingly, Table 3.3 also shows that the minimum achievable onset pressure for layered subspaces is greater than for the non-layered smooth variations.

How quickly a smooth BC-like stiffness distribution impacts onset pressure compared to layered BC stiffness distributions also depends on how the "magnitude" of the stiffness distributions are measured. To illustrate this, different norms of ΔE_1 are given in Table 3.4. A summary of effective eigenvalues (Equation (3.12)) for each norm is given in Table 3.5. Since the 2-norm and l_2 norm have similar magnitudes across all subspaces, the relative sensitivities in these cases are similar; that is smooth BC-like stiffness changes will result in larger onset pressure changes compared to layered ones. The $\infty-$norm shows the greatest disparity across subspaces and as a result relative sensitivities change; however, smooth BC-like stiffness changes still result in larger onset pressure changes compared to layered ones but only by a factor of $364/260 = 1.4$.

To better illustrate the difference in sensitivity of onset pressure based on eigenvalues

Table 3.4: Comparison of eigenvector norms when stiffness is constrained to different subspaces, for the linearization point $(E_b, E_c) = (6\,\text{kPa}, 6\,\text{kPa})$

Basis	$\|\|E_1\|\|_2$	$\|\|E_1\|\|_{l_2(\Omega)}$	$\|\|E_1\|\|_\infty$
unstructured	1.000	0.028	0.141
BC-CB	1.000	0.026	0.125
BC-C	1.000	0.024	0.121
BC	1.000	0.025	0.070

Table 3.5: Comparison of norm-adjusted eigenvalues for different norms (shown in parentheses) when stiffness is constrained to different subspaces, for the linearization point $(E_b, E_c) = (6\,\text{kPa}, 6\,\text{kPa})$

Basis	Λ_1 $(\|\| \cdot \|\|_2)$	Λ_1 $(\|\| \cdot \|\|_{l_2(\Omega)})$	Λ_1 $(\|\| \cdot \|\|_\infty)$
unstructured	10.0	12892.0	497.9
BC-CB	3.1	4488.6	195.2
BC-C	1.6	2678.6	109.0
BC	0.8	1265.4	164.9

in Table 3.3, Figure 3.6 shows the onset pressure variation as stiffness perturbs along ΔE_1. Considering the point $-15\Delta E_1$, for example, the change in stiffness has the same size ($||\Delta E_1||_2 = 1$ for each subspace) for each subspace but onset pressure varies greatly. While onset pressure for the layered subspaces is typically decreasing (along the $-\Delta E_1$ direction) at this point, the onset pressure for the unstructured subspaces begins to rapidly increase again.

3.4 Discussion

3.4.1 Utility of the Taylor model

The second order Taylor model for onset pressure decomposes the generally complicated effects of VF stiffness on onset pressure into three important stiffness variations, making the effect of stiffness variations easier to interpret. Stiffness changes correlated with the directions $(\Delta E_1, \Delta E_2)$ (Figure 3.3) result in quadratic increases in onset pressure and resemble a smooth BC-like stiffness change and a smooth IS-like stiffness change, concentrated in the body layer, respectively. Stiffness changes correlated with the direction ΔE_0

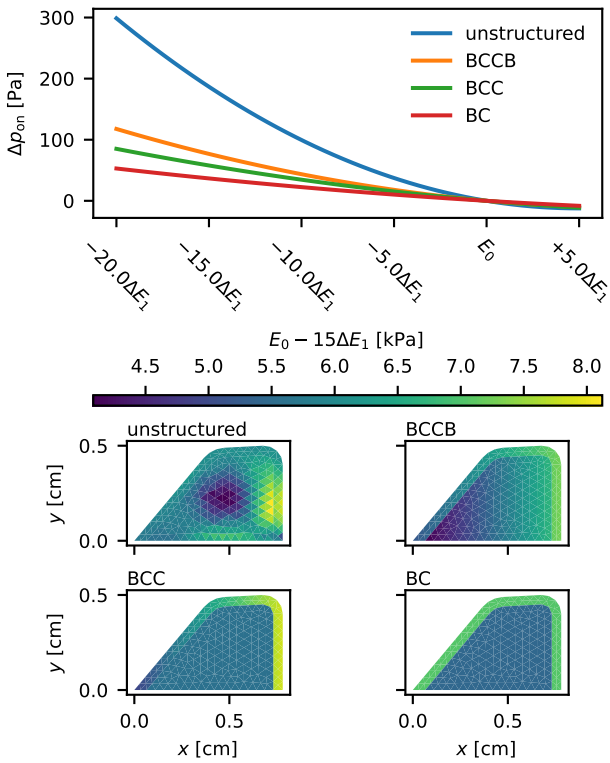

Figure 3.6: Onset pressure predicted by the Taylor model when stiffness is perturbed along ΔE_1 for each subspace

result in a linear increase in onset pressure. Equation (3.10) shows that the combined effect of simultaneous changes along all three directions is simply the sum of each individual effect, making it easy to interpret the end result. While the linear direction roughly results in a uniform increase in stiffness, changes along the quadratic directions involve reduced changes in average stiffness since stiffness is increased in some regions and decreased in others. Since the average stiffness does not change for the quadratic directions these have a minor impact on the frequency of oscillation. This gives the qualitative picture that increasing average stiffness of the VFs increases onset frequency and the onset pressure, whereas changing the BC-like and IS-like stiffness distributions about this average stiffness can raise or lower the onset pressure for the given frequency. For the case of an average stiffness of 6 kPa, Figure 3.3 shows a smooth distribution with a looser cover, stiffer body, and gradual changes in stiffness throughout can reduce onset pressure by about 30 Pa compared to a uniform BC distribution (Table 3.3).

The Taylor model also allows us to interpret the combined effects of previously reported stiffness variations, specifically, the IS cover stiffness gradient and BC stiffness. While previous studies have shown that changes in either one independently tends to reduce onset pressure [18, 21, 25] the Taylor model (Figures 3.3 and 3.5) shows that both changes can be interpreted as projections of the same quadratic effect due to stiffness changes along ΔE_1. Perturbing either the IS cover stiffness gradient or BC stiffness difference alone will only capture part of the change in onset pressure given by ΔE_1. Instead, perturbing both together (to correlate with the distribution ΔE_1) will result in a greater change in onset pressure for a similar magnitude of stiffness change. This is important since it is likely that IS stiffness gradients and BC stiffness differences are correlated in real VFs.

3.4.2 Effect of different linearization points on the Taylor model

While the Taylor model shows that a smooth BC-like, IS-like, and uniform stiffness change have the strongest effects on onset pressure, this only applies to 'small' deviations about the linearization point. As stiffness distributions change significantly from this linearization point, non-linear behaviours could become significant, potentially resulting in smooth stiffness distributions different from the BC-like and IS-like distributions reported having the strongest effects on onset pressure. To determine if this is a strong limitation, we tested several linearization points. Four linearization points consisting of body to cover stiffness ratios of $1{:}1, 2{:}1, 3{:}1,$ and $4{:}1$ were tested with the 1:1 and 2:1 cases shown in Figures 3.3 and 3.4. Although the eigenvalue magnitudes changed with linearization point, we found qualitative similarities in the eigenvectors across all the linearization points, which suggests these stiffness perturbations capture some global effect of stiffness on onset pressure. This could be due to stiffness changes along these eigenvectors playing a role in the onset instability; for each linearization point, we found that onset involved the commonly seen mode synchronization between a ML vibration and a mucosal wave vibration [21] so we hypothesize that the eigenvectors affect onset through altering the physics of interaction between these modes. If a linearization point involved different onset physics, for example through synchronization of more than two modes or different modes, then it is likely the eigenvectors found here would change.

3.4.3 Importance of non-layered stiffness on onset pressure and frequency

Comparing sensitivity models for non-layered versus layered stiffness variations illustrates the limitations of using idealized layered variations to study onset pressure in real VFs. Consider varying stiffness along the first eigenvector, ΔE_1, which resembles a BC-like stiffness change for both the non-layered and layered subspaces (see Figures 3.3 and 3.5). For the same unit step along ΔE_1, onset pressure changes by over 3 times more along the smooth BC-like stiffness compared to the layered BC-like stiffness change (Table 3.3) despite the fact the two stiffness distributions look qualitatively similar. This shows that the smooth gradations in stiffness, present for the unstructured subspace eigenvector, play an important role in the onset physics. Considering that stiffness in the VFs can be roughly linked to muscle activation, this implies, for example, that smooth stiffness variations can model large changes in onset pressure with small changes in stiffness. This could mean that smaller muscle activations are needed to decrease onset pressure with smooth VFs stiffness, which would be beneficial for preventing muscular fatigue. Similarly, allowing stiffness variations along the smooth unstructured subspace eigenvectors results in a lower minimum achievable onset pressure (Table 3.3). While the difference in minimum onset pressure is relatively small (approximately 10 %), these differences could play a large role in voicing over sustained periods and may also be larger at different voicing conditions not investigated here.

One limitation of this comparison is that the difference in onset pressure models between the non-layered and layered subspaces is not necessarily the same as the difference between 'physiological' and layered stiffness variations. As mentioned previously, while smooth gradations in material properties are known to occur in VFs, what these variations exactly are is unclear due to the numerous difficulties in measuring VF properties. The eigenvectors obtained for the non-layered subspace represent the smooth variations in stiffness that have the greatest impact on onset pressure and therefore are a best case comparison. If physiological smooth variations in stiffness are well correlated with those obtained for the non-layered subspace (see ΔE_1 Figures 3.3 and 3.4) then our findings show that idealized BC stiffness distributions, despite their qualitative resemblance to smooth reported VF stiffness distributions, will be a poor model for exploring the effect of stiffness changes on onset pressure in real VFs.

3.4.4 Relation to other findings on effects of stiffness

Our results provides an alternative interpretation for those of Titze [18], who found that the higher the mucosal wave velocity, the higher the onset pressure. Assuming that mucosal wave velocity increases with cover stiffness suggests that decreasing cover stiffness consistently decreases onset pressure. Our results somewhat agree with this as we find that lower cover stiffness generally decreases onset pressure; however, this is decomposed into two effects. Along a direction where cover stiffness decreases while body stiffness increases, we find onset pressure has a quadratic effect with large positive curvature (Figure 3.3) which means onset pressure can either increase or decrease depending on where the stiffness is located along the quadratic curve. Along a direction where average stiffness decreases, onset pressure decreases approximately linearly due to the linear trend in our Taylor model. Purely decreasing cover stiffness changes the body to cover ratio while also decreasing the average VF stiffness which would generally decrease onset pressure. Our model suggests the possibility, however, that quadratic increases in onset pressure (from changing the BC stiffness difference) can potentially exceed linear decreases in onset pressure (from decreasing the average stiffness), which would result in increases in onset pressure with decreasing cover stiffness.

Our results also mostly agree with those from Zhang [21]. In the case of decreasing both body and cover stiffness, Zhang [21] found that onset pressure generally decreases, which is also predicted in our study from the uniform linearization point (Figure 3.3). Contours in Figure 15 b from [21] show a negative curvature for high body to cover stiffness ratios along a BC stiffness change (increasing body stiffness with decreasing cover stiffness). Using our model to explore onset pressure for high body to cover stiffness ratios, we found similar behaviour. For body to cover stiffness ratios near 1:1 we found a positive curvature which suggests that an optimal body and cover stiffness minimizes onset pressure. This curvature is not as apparent in [21, Figure 15 b], but could be related to differences in modelling approaches, model parameters, or VF geometry, to name a few. For example, Zhang [21] used a constant flow boundary condition while a constant pressure boundary condition was used herein. To test if the constant flow boundary condition could account for the difference in results, we implemented a subglottal flow driven Bernoulli fluid model and found similar contours for 1:1 body to cover stiffness ratios which suggests this could be the reason for the discrepancy. We employed the constant pressure boundary condition since this more closely resembles the constant subglottal pressure provided by the lungs.

Finally our results extend those of Geng et al. [25] who used a 3D continuum model to investigate the effect of an IS stiffness gradient (where the superior side is softer than the inferior side). Geng et al. [25] found that increasing the IS gradient increased sound

intensity and peak flow rate while lowering onset pressure. Our results suggest that changing the IS stiffness gradient while not changing the BC ratio has a quadratic effect on onset pressure due to the positive curvature shown in Figure 3.5. Starting from the uniform linearization point shown in Figure 3.5, increasing the IS gradient (travelling along the $+\Delta E_1$ direction) would tend to initially decrease onset pressure, as found by Geng et al. [25], until the critical stiffness, E^*, is reached where a minimum in onset pressure is achieved. Continually increasing the IS gradient past this point will increase onset pressure again provided non-linear effects do not become dominant.

3.4.5 Limitations

Our study has a few important limitations. The sensitivity analysis is local so it is likely that the behaviour of onset pressure at different linearization points can change. We attempted to ameliorate this by computing sensitivities over a variety of reasonable linearization points and found similar qualitative patterns, which suggests that our analysis applies somewhat globally. Nevertheless, it is possible that other linearization points could exhibit different sensitivities, for example, under changes in the VF geometry or layer shapes.

We employed a finite-difference method to approximate the action of the Hessian for computing eigendecompositions. This method is subject to numerical error due to the finite-difference step size which could influence the predicted eigenvectors. We experimented with different step sizes and found that the eigenvectors with largest eigenvalues were minimally affected, suggesting these are accurate (see Appendix A.3); however, eigenvectors with small absolute eigenvalues could still be impacted.

We used a 1D Bernoulli glottal flow with an ad hoc imposed separation point. As shown in Appendix A.2, the 1D Bernoulli flow and imposed separation point can lead to strong discontinuities in sensitivities for large IS stiffness ratios. To illustrate that this is a numerical effect, we showed that moving the imposed separation point location does not changes the form of the smooth Hessian eigenvectors, which suggests that the smooth eigenvectors are affected by the bulk coupled forcing between glottal flow and VF, rather than the specific separation point location. Future studies, however, should employ a more physical separation point model to avoid this effect.

We used a 2D VF model for simplicity which can affect the dynamical behaviour of the coupled VF model. For long VFs where the plane strain condition is approximately satisfied, we expect our results may be minimally affected. However, three-dimensional VFs can also incorporate transversely isotropic properties and may have anterior-posterior

mode variations which could introduce different structures compared to the sensitivity analysis presented here. Future work should therefore aim to use 3D VF models.

3.5 Conclusions

This work presented the results of a sensitivity analysis of onset pressure resulting in a low-dimensional model that showed the complicated effects of stiffness variations on onset pressure can be decomposed into just three core components: a quadratic change in onset pressure from stiffness changes along BC-like and IS-like stiffness perturbations, and a linear increase in onset pressure due to uniform increases in stiffness. These three core stiffness variations represent the stiffness perturbations with the greatest impact on onset pressure and consist of smooth gradients in stiffness (Figure 3.3) that resemble reported stiffness variations from histology. Considering that increases in average stiffness are associated with increases in natural frequency, the Taylor model roughly suggests that uniform stiffness increases result in increased onset pressure associated with increased onset frequency, and that for a given onset frequency a particular BC-like and IS-like stiffness change can minimize onset pressure. Using this Taylor model also facilitates extending results from past studies on the effects of different stiffness variations. For example, previous studies have found that increasing the BC stiffness difference (making the cover softer) and increasing the IS stiffness gradient tends to reduce onset pressure; the Taylor model shows that these two effects are projections of a quadratic change in onset pressure along a stiffness perturbation direction that combines aspects of both changes.

Comparing onset pressure sensitivity models when stiffness is allowed to vary smoothly and arbitrarily to onset pressure sensitivity models where stiffness varies according to an a priori layered structure shows that layered stiffness changes might not capture the magnitude of onset pressure variability seen for smooth stiffness changes in real VFs. Perturbing stiffness with smooth spatial distributions, as observed histologically, results in larger changes in onset pressure compared to perturbing with discretely layered stiffness distributions, as commonly done in computational studies. Lower minimum onset pressures (of about 10 Pa for the considered case) are also achievable when stiffness variations are smoothly varying compared to layered. This makes modelling smooth physiological stiffness variations important because these variations increase the variability in onset pressure with changes in stiffness. By relating muscle activation to stiffness change, for example, this suggests small muscle activations could produce large changes in onset pressure which would be important for vocal fatigue.

Chapter 4

Examining the influence of epithelium layer modeling approaches on vocal fold kinematics and kinetics [1]

4.1 Introduction

This chapter presents the development and analysis of a thin-structure model for the epithelium layer of the VFs. The development of a thin-structure model for the epithelium layer is important for reducing computational cost since a large number of small mesh elements is required otherwise, thus increasing computational cost. While the epithelium and superficial lamina propria are commonly modeled as a lumped cover, this chapter uses the developed epithelium layer model to compare this approach against modeling the layers separately. Accurate modeling of the cover layer is important for the investigation of swelling in Chapter 5 since swelling is primarily observed in the cover layer. In fact, due to the significant difference between modeling separate layers and modeling a lumped cover, the developed model is subsequently used in Chapter 5.

[1] This work was co-authored by Sean D. Peterson. I developed the code, performed the simulations, analyzed data, generated figures, and wrote the first draft of the manuscript. SDP contributed to conceptualization, supervised the work, and reviewed the manuscript. Part of this chapter was published as an article in Biomechanics and Modeling in Mechanobiology [1].

The chapter is organized as follows. Section 4.2 outlines the FEM VF model and epithelium treatments, as well as the numerical solution strategy and study design. Section 4.3 discusses the membrane epithelium model and its validation. Sections 4.4 and 4.5 report and discuss the results, including study limitations. Finally, Section 4.6 summarizes the main conclusions of the study.

4.2 Methods

4.2.1 Vocal fold model

The two-dimensional VF model employed herein is based upon the medial surface of the M5 geometry [119, Figure 1], see Figure 4.1. Note that the medial-lateral dimension is smaller (when scaled) than that of the physical full M5 model used by Scherer et al. [119]. Internal layers correspond to the body and cover histological layers. Treatment of the epithelial layer varies, as described in Section 4.2.3. A Cartesian coordinate system is defined with the x-axis pointing in the superior direction and the y-axis pointing medially. A curvilinear coordinate s is also defined along the VF surface. The origin of the coordinate system is at the tracheal wall at the inferior margin of the VF, as shown in Figure 4.1.

Assuming small displacements and plane-strain, the governing conservation of linear momentum equation for the VF dynamics can be written in the weak form as

$$\begin{aligned}\int_{\Omega} &\left(\rho\ddot{\boldsymbol{u}}(\boldsymbol{X},t)\cdot\delta\boldsymbol{u}(\boldsymbol{X},t) + \boldsymbol{\sigma}(\boldsymbol{X},t):\boldsymbol{\epsilon}(\delta\boldsymbol{u}(\boldsymbol{X},t))\right)\, d\boldsymbol{X} \\ &= \int_{\partial\Omega_{\mathrm{n}}} \boldsymbol{t}(\boldsymbol{X},t)\cdot\delta\boldsymbol{u}(\boldsymbol{X},t)\, ds \text{ for all } \delta\boldsymbol{u}\in\boldsymbol{V}^2(\Omega),\end{aligned} \tag{4.1}$$

where $\boldsymbol{X} = (x, y)$ is a position vector in the material domain Ω with boundary $\partial\Omega$, t is time, ρ is the material density, $\boldsymbol{V}(\Omega)$ is the space of scalar valued piece-wise linear functions over Ω equal to 0 on $\partial\Omega_{\mathrm{d}}$ with nodal basis functions $\phi_i(\boldsymbol{X})$ $i \in 1, 2..., N$, $\boldsymbol{V}^2(\Omega)$ is the associated vector valued function space, $\boldsymbol{u} \in \boldsymbol{V}^2(\Omega)$ is the displacement vector, $\delta\boldsymbol{u} \in \boldsymbol{V}^2(\Omega)$ is a test vector, $\boldsymbol{\epsilon}(\boldsymbol{u}) = 1/2\,(\partial\boldsymbol{u}/\partial\boldsymbol{X} + \partial\boldsymbol{u}/\partial\boldsymbol{X}^{\intercal})$ is the infinitesimal strain tensor with superscript $(\cdot)^{\intercal}$ indicating transposition, $\boldsymbol{\sigma}$ is the Cauchy stress tensor, and $\boldsymbol{t}$ is the surface traction. The operator $\dot{(\,)}$ indicates differentiation with respect to time. Note that the domain boundary is decomposed into two regions, the fixed region $\partial\Omega_{\mathrm{d}}$ and the medial surface $\partial\Omega_{\mathrm{n}}$, as shown in Figure 4.1. Assuming linear, isotropic (due to the 2D

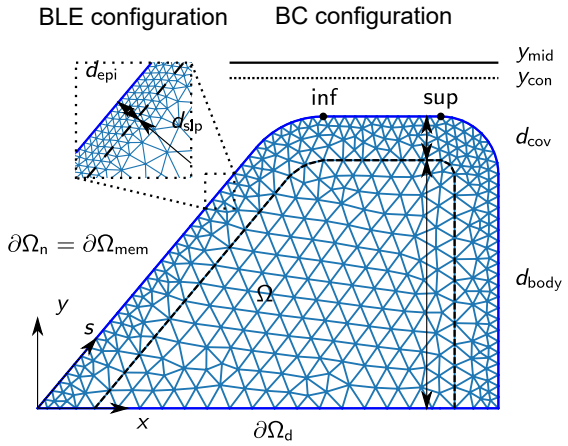

Figure 4.1: Schematic of the vocal fold geometry comprising body and cover internal layers and the discretization ($d_{\text{cov}} = 0.075\,\text{cm}$ case shown). Layers consist of uniform depth projections from the medial surface. Two variations of the internal layer geometry are shown as the body-SLP-epithelium (BLE) and body-cover (BC), the former of which is used to model the epithelium as a distinct layer of finite thickness, and the latter used for all other epithelium treatments

model), Kelvin-Voigt viscoelastic media, the Cauchy stress tensor can be written as [67]

$$\boldsymbol{\sigma} = \frac{E\nu}{(1+\nu)(1-2\nu)}\text{Tr}(\boldsymbol{\epsilon})\boldsymbol{I} + \frac{E}{1+\nu}\boldsymbol{\epsilon} + \eta\dot{\boldsymbol{\epsilon}}, \tag{4.2}$$

where E and ν are Young's modulus and Poisson's ratio, respectively, η is a viscous damping coefficient, and $\boldsymbol{I}$ is the identity tensor. In general the material properties change between layers, with E_{body}, E_{cover}, E_{slp}, and E_{epi} corresponding to the Young's moduli of the body, cover, SLP, and epithelium layers, respectively. This subscript notation for the various layers will be used for the remainder of the manuscript.

Surface traction consists of a contact component, modeled by the penalty method [60, Section 6.3.2], and an external pressure due to the glottal flow, given by

$$\boldsymbol{t} = -p\det\boldsymbol{F}\boldsymbol{F}^{-\intercal}\boldsymbol{n} - p_{\text{con}}\boldsymbol{n}_{\text{con}}, \tag{4.3}$$

$$p_{\text{con}}(\boldsymbol{X}) = k_{\text{con}}\left(\frac{\max\{g(\boldsymbol{X}),0\}}{2}\right)^3, \tag{4.4}$$

$$g(\boldsymbol{X}) = y(\boldsymbol{X}) - Y_{\text{con}}, \tag{4.5}$$

where p is the applied aerodynamic pressure, p_{con} is the pressure arising due to collision between the opposing folds, $\boldsymbol{n}$ is the unit outward-pointing normal vector from $\partial\Omega_{\text{n}}$, $\boldsymbol{F} =$

$\boldsymbol{I}+\partial\boldsymbol{u}/\partial\boldsymbol{X}$ is the deformation gradient tensor, k_{con} is the penalty spring constant, and $\boldsymbol{n}_{\text{con}}$ is the contact plane normal vector. Herein, symmetric VFs and oscillations are assumed such that only one VF need be considered (see Figure 4.1) and thus the contact plane orientation is $\boldsymbol{n}_{\text{con}} = (0, 1)$. Note that $g(\boldsymbol{X})$ is positive when the folds are colliding.

4.2.2 Glottal flow model

Glottal aerodynamics are modeled using one-dimensional Bernoulli flow with an *ad hoc* flow separation criteria, see for example, Story and Titze [54], Alipour-Haghighi et al. [66], and Decker and Thomson [71]. Prior studies have shown that Bernoulli flow reasonably captures the first-order fluid loading effects driving VF motion [71]. As the current study focuses on modeling the epithelium, a higher fidelity fluid model and the associated computational expense is eschewed.

The aerodynamic pressure p and glottal flow rate q are given by

$$p(s) = \begin{cases} p_{\text{sub}} + \frac{\rho_{\text{air}}}{2} q^2 \left(\frac{1}{a_{\text{sub}}^2} - \frac{1}{a(s)^2} \right) & s < s_{\text{sep}} \\ p_{\text{sep}} & s \geq s_{\text{sep}} \end{cases} \tag{4.6}$$

$$q^2 = \frac{2}{\rho_{\text{air}}} \left(\frac{1}{a_{\text{sep}}^2} - \frac{1}{a_{\text{sub}}^2} \right)^{-1} (p_{\text{sub}} - p_{\text{sep}}) \tag{4.7}$$

where ρ_{air} is the air density and $a(s) = 2(Y_{\text{mid}} - y(s))$ is the glottal area (per unit-length) at location s. Subscripts $(\cdot)_{\text{sub}}$ and $(\cdot)_{\text{sep}}$ denote subglottal and separation quantities, respectively. The flow separation condition is prescribed *a priori* via separation area ratio, r_{sep}. The minimum glottal area and its position are determined as

$$\begin{aligned} a_{\text{min}} &= \min_s a(s), \\ s_{\text{min}} &= \arg\min_s a(s) \end{aligned} \tag{4.8}$$

from which the area and location of separation are found as

$$\begin{aligned} a_{\text{sep}} &= r_{\text{sep}} a_{\text{min}} \\ s_{\text{sep}} &= \arg\min_{s \geq s_{\text{min}}} |a(s) - r_{\text{sep}} a_{\text{min}}|. \end{aligned} \tag{4.9}$$

Following Anderson et al. [72], in practice a "safe" area is employed to prevent negative areas that can occur due to the penalty collision method. As such, $a(s)$ in Equation (4.6)

is replaced by $a_{\text{safe}}(s)$, where

$$a_{\text{safe}}(s) = \begin{cases} a(s) & a(s) > a_{\text{lb}} \\ a_{\text{lb}} & a(s) \leq a_{\text{lb}} \end{cases} \tag{4.10}$$

and $a_{\text{lb}} = 2(Y_{\text{mid}} - Y_{\text{con}})$ is a small value separating the midplane from the collision plane, see Figure 4.1.

4.2.3 Epithelium models

Two epithelium treatments are considered, denoted as Integrated and Distinct. For Integrated, the epithelium and SLP are combined into a single cover layer, whereas with Distinct, the epithelium and SLP are modeled as separate layers. For each epithelium treatment, two models are developed as summarized in Table 4.1 and described below.

Table 4.1: Summary of epithelium model treatments and the four models used in this study

Treatment	Description	Model	Description
Integrated	epithelium and SLP integrated into a single cover layer	AE	weighted average of the epithelium and SLP properties for the cover
		NE	use only SLP properties for the cover
Distinct	epithelium and SLP treated as distinct layers	FTE	epithelium meshed as a finite thickness layer
		ME	epithelium treated using a membrane approximation

The Integrated treatment yields the No Epithelium (NE) and Averaged Epithelium (AE) models. In the former, the epithelium is neglected and the cover stiffness is set as the SLP stiffness, $E_{\text{cover}} = E_{\text{slp}}$. For the latter, the cover layer stiffness is set as the layer thickness-weighted average of the epithelium and SLP Young's moduli, $E_{\text{cover}} = \left(d_{\text{epi}}E_{\text{epi}} + d_{\text{slp}}E_{\text{slp}}\right)/d_{\text{cov}}$, where $d_{\text{cov}} = d_{\text{epi}} + d_{\text{slp}}$.

The Distinct treatment yields the Finite-Thickness Epithelium (FTE) and Membrane Epithelium (ME) models. For the FTE model, the epithelial layer has non-zero thickness

d_{epi} and stiffness E_{epi}, while the SLP layer has stiffness E_{slp}. The ME model treats the epithelium with the membrane model (introduced in Section 4.3) with stiffness $E_{\text{mem}} = E_{\text{epi}}$, $d_{\text{mem}} = d_{\text{epi}}$, and the cover layer stiffness is given by $E_{\text{cover}} = E_{\text{slp}}$.

4.2.4 Solution method and analysis

The coupled system described in Sections 4.2.1 and 4.2.2 is solved as follows. The domain Ω is discretized using triangular elements as shown in Figure 4.1. The figure introduces two internal layer configurations, the body-cover (BC) and body-SLP-epithelium (BLE). The BLE configuration, which is used in the FTE model, contains 'epi', 'slp', and 'body' layers representing the epithelium, SLP and body, respectively. On the other hand, the BC configuration contains only a 'cov' and 'body' layer, representing the cover and body layers, respectively, and is used for all other epithelium models (AE, NE, and ME). The 'epi' layer of the BLE configuration allows an epithelium to be explicitly modeled by prescribing appropriate material properties of the 'epi' layer but at the cost of a high mesh density. In contrast, the BC configuration can only model the effects of an epithelium layer using a membrane model as described later in Section 4.3, but generally requires a lower mesh density.

With the domain discretized, Equation (4.1) is solved in discrete form using the FEM library *FEniCS* [121]. The fluid and solid domains are coupled by treating the pressure on the boundary $\partial\Omega_{\text{n}}$ as piece-wise linear with nodal values evaluated from Equation (4.6). The VF is coupled explicitly in time with the glottal flow [67]. Equation (4.1) is integrated in time using Newmark's method [126] with parameters $\gamma = 0.5$ and $\beta = 0.25$ for 2^{nd} order accuracy and unconditional stability.

Parameter values for the model are summarized in Table 4.2. The VF density was that of water and Poisson's ratio was set such that the VF was nearly incompressible. The damping coefficient, η, was chosen based on previous studies [62, 66]. The body layer and SLP stiffnesses were based on past studies and experimental measurements [19, 66, 81, 127–129]. Two SLP stiffnesses are considered, denoted herein as stiff $(E_{\text{slp}}, p_{\text{sub}}) = (4\,\text{kPa}, 1.5\,\text{kPa})$, and soft $(E_{\text{slp}}, p_{\text{sub}}) = (0.5\,\text{kPa}, 0.8\,\text{kPa})$. Note that p_{sub} varies across the two cases to ensure reasonable VF displacements. The three epithelium moduli were chosen to cover a wide range centered on the reported value of 100 kPa [130]. The three cover depths, d_{cov}, were chosen based on ranges from previously reported data [17] and computational studies [85]. The collision penalty parameter, k_{con}, was chosen to balance increasing ill-conditioning of the stiffness matrix with minimization of over-penetration during contact [60]. The separation area ratio r_{sep} was chosen based on previous studies [54,

Table 4.2: Summary of model parameter values. Top block: vocal fold properties; middle block: contact and mid-plane properties; bottom block: fluid model properties

Parameter	Units	Value(s)
E_{body}	kPa	15
E_{slp}	kPa	0.5, 4
E_{epi}	kPa	50, 100, 200
d_{body}	cm	0.5 - d_{slp}
d_{slp}	cm	0.025, 0.05, 0.075
d_{epi}	cm	0.005
η	poise	5
ρ	g/cm^3	1
ν	-	0.45
Y_{mid}	cm	0.505
Y_{con}	cm	Y_{mid} - 1×10^{-5}
k_{con}	Pa/cm^3	1×10^{16}
ρ_{air}	g/cm^3	1.225×10^{-3}
p_{sub}	kPa	0.8 (soft SLP), 1.5 (stiff SLP)
p_{sep}	kPa	0
r_{sep}	-	1.2
a_{lb}	cm	1×10^{-5}

57, 131]. Table 4.3 presents the resulting cover stiffness employed for the AE model for each considered case. Note that for the range of epithelium stiffness and cover depth considered, the resulting cover stiffness for the AE model is tabulated in Table 4.3. The resulting cover stiffnesses are large due to the high epithelium stiffness contribution in the average. For example, for $d_{\text{cov}} = 0.05\,\text{cm}$, the epithelium occupies 10 % of the cover and it follows that $E_{\text{cover}} \geq 0.1 \times 100\,\text{kPa} = 10\,\text{kPa}$ at $E_{\text{epi}} = 100\,\text{kPa}$.

To explore the impact of epithelium model selection, the ME model (Distinct) was compared against the AE and NE models (Integrated) over all variations in cover depth (d_{slp}), stiffness (E_{cover}), and epithelium stiffness (E_{epi}) for a total of 18 conditions [2]. Variations in epithelium stiffness and cover thickness were explored to elucidate the effects of differing epithelium-to-SLP thickness and stiffness. Specifically, as the epithelium stiffness or relative depth in the cover increases, its effect on the cover dynamics is expected to increase.

[2]With a soft SLP the NE model did not self-oscillate, so only the ME and AE models are compared in these cases.

Table 4.3: Summary of E_{cover} values for the AE model for varying d_{cov} and E_{epi} for the stiff/soft conditions

	E_{epi}[kPa]		
d_{cov}[cm]	50	100	200
0.025	10.4 kPa/13.2 kPa	20.4 kPa/23.2 kPa	40.4 kPa/43.2 kPa
0.050	5.5 kPa/8.6 kPa	10.5 kPa/13.6 kPa	20.5 kPa/23.6 kPa
0.075	3.8 kPa/7.1 kPa	7.1 kPa/10.4 kPa	13.8 kPa/17.1 kPa

To compare results, a combination of modal analysis and time domain simulations were used. For modal analysis, the generalized eigenvalue problem

$$\boldsymbol{M}\boldsymbol{B} = \frac{1}{\omega^2}\boldsymbol{K}\boldsymbol{B}$$

was solved, where $\boldsymbol{B}$ is a mode vector of nodal values such that $\boldsymbol{b} = \sum_i \phi_i B_{i,x}\hat{\boldsymbol{e}}_x + \phi_i B_{i,y}\hat{\boldsymbol{e}}_y$ is the associated function where subscripts $(\cdot)_x$ and $(\cdot)_y$ denote x and y components and $\hat{\boldsymbol{e}}$ is a unit vector. Matrices $\boldsymbol{M}$ and $\boldsymbol{K}$ are mass and stiffness matrices (derived from Equation (4.1) with nodal basis functions ϕ), respectively, and ω is the modal frequency. Mode shapes were normalized such that their maximum displacement component was 0.2 cm. For quantitative comparison of mode shape errors, a relative error is defined as

$$\text{err}\,(\boldsymbol{b}_1, \boldsymbol{b}_2) = \frac{||\boldsymbol{b}_1 - \boldsymbol{b}_2||_{l_2(\Omega)}}{||\boldsymbol{b}_1||_{l_2(\Omega)}} \tag{4.11}$$

where $||\cdot||_{l_2(\Omega)}$ indicates the L2 norm.

Time dependent simulations were conducted over a total of 1.0 s with the first 0.5 s using a time step of $\Delta t = 2 \times 10^{-5}$ s to resolve the initial transient behavior and the final 0.5 s using a model-dependent time step. Only the final 0.5 s was used for analysis. To compare transient simulations we compute the glottal width defined by

$$y_{\text{gw}} = \min_s a_{\text{safe}}(s), \tag{4.12}$$

which represents the area between the vocal folds. A number of clinically relevant measures were also computed from y_{gw} to compare the models. The open quotient (OQ; percentage of T during which the glottal width is nonzero), speed quotient (SQ; ratio of opening to closing time of the folds), and maximum area declination rate (MADR; maximum slope of the glottal width waveform during the VF closing phase) [132], were extracted from

the glottal area waveform. In addition, inferior-superior displacement, contact pressure, viscous dissipation, and the average von Mises stress in the SLP layer, given by

$$u_{\text{inf-sup}} = \max_{\boldsymbol{X}} u_x(\boldsymbol{X}, t), \tag{4.13}$$

$$p_{\text{coll}} = \frac{\int_{\partial\Omega_{\text{n}}} p_{\text{con}} ds}{\int_{\partial\Omega_{\text{n}}} ds}, \tag{4.14}$$

$$w_{\text{visc}} = \int_{\Omega_{\text{slp}}} \eta \dot{\boldsymbol{\epsilon}} : \dot{\boldsymbol{\epsilon}} d\boldsymbol{X}, \tag{4.15}$$

$$\sigma_{\text{vm}} = \frac{\int_{\Omega_{\text{slp}}} \sqrt{3 \det(\boldsymbol{\sigma}_{\text{dev}})} d\boldsymbol{X}}{\int_{\Omega_{\text{slp}}} d\boldsymbol{X}}, \tag{4.16}$$

respectively, were computed, where $\boldsymbol{\sigma}_{\text{dev}} = \boldsymbol{\sigma} - (\text{Tr}(\boldsymbol{\sigma})/3)\boldsymbol{I}$ is the deviatoric part of the stress tensor. To summarize these quantities, we also compute means and maxima over time and denote them by $\overline{(\cdot)}$ and $\max(\cdot)$, respectively. In the case of contact pressure, p_{coll}, the mean over time only includes times during which contact occurs. Finally we computed the mucosal wave phase difference, $\Delta\Phi_{\text{inf-sup}}$, and wave speed, c_{mucosal}, based on computed phases from the discrete Fourier transform of vertical displacements at predefined inferior and superior points on the medial surface (see Figure 4.1) and following formulae given by Titze et al. [133].

The mesh sizes and time steps used in the discretized equations were based on mesh and time step independence studies. Figure 4.2 illustrates a mesh independence study $(E_{\text{slp}}, d_{\text{cov}}) = (4\,\text{kPa}, 0.05\,\text{cm})$ comparing the ME and FTE models through modal frequencies as a function of uniform mesh cell size refinement. Errors were generally less than 2 % at our chosen mesh refinement level (level 1). Figure 4.3 shows a time step independence study comparing the AE, NE, and ME models for $(E_{\text{epi}}, d_{\text{cov}}) = (100\,\text{kPa}, 0.05\,\text{cm})$ for two pertinent measures w_{visc} and $\Delta\Phi_{\text{inf-sup}}$. A time step of 1×10^{-5} s results in less than 2 % error for the NE and AE models while a time step of 2.5×10^{-6} s (refinement factor of 4) is required to achieve a similar level of error for the ME model. Therefore $\Delta t = 1 \times 10^{-5}$ s was used for the NE and AE models while $\Delta t = 2.5 \times 10^{-6}$ s was used for the FTE and ME models.

4.3 Membrane epithelium model

The epithelium, which ranges from 50 µm to 80 µm in thickness [130], generally comprises less than 10 % of the cover layer. In this section we present the Membrane Epithelium

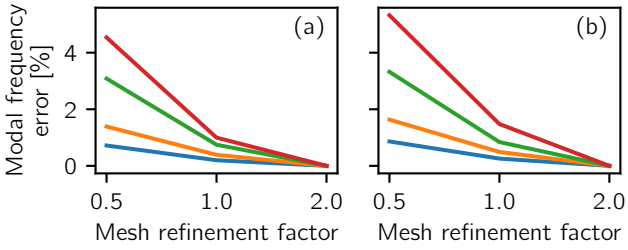

Figure 4.2: Modal frequency dependence on mesh cell size factor for $(E_{\text{epi}}, d_{\text{cov}}) = (100\,\text{kPa}, 0.05\,\text{cm})$ for the (a) FTE, and (b) ME models. A mesh refinement factor of 1 corresponds to mesh densities similar to those shown in Figure 4.1. For the nominal cell size h_0 and refinement factor f, the corresponding cell size is h_0/f

framework, which reduces the layer in the FEM model to zero thickness (that is, the FEM epithelium layer is a one-dimensional surface). For very thin structures, in-plane tangential stresses dominate [134] so that structures obey the plane-stress assumption [135]. Given the small epithelial layer thickness, it is hypothesized to behave as a membrane, which allows the plane-stress assumption to be applied. In this section the ME model will be introduced and validated against a direct approach that models the epithelium using a fine mesh (the FTE model).

4.3.1 Membrane model development

Following the approaches of Hansbo and Larson [136] and Delfour and Zolésio [137, 138], the membrane epithelium is implemented as an additional strain energy over the VF surface $\partial\Omega_{\text{mem}}$, see Figure 4.1 (note that the membrane surface $\partial\Omega_{\text{mem}}$ here is equivalent to $\partial\Omega_{\text{n}}$). The strain tensor in the membrane consists of in-plane and normal components (due to Poisson's ratio) with negligible shear strain and is given by

$$\begin{aligned}\boldsymbol{\epsilon}_{\text{mem}} &= \boldsymbol{N}^{\perp}\boldsymbol{\epsilon}(\boldsymbol{u})\boldsymbol{N}^{\perp} + \hat{\boldsymbol{\epsilon}}_{\text{nn}}\boldsymbol{N} \\ &= \boldsymbol{\epsilon}_{\text{pp}} + \hat{\boldsymbol{\epsilon}}_{\text{nn}}\boldsymbol{N},\end{aligned} \tag{4.17}$$

where $\boldsymbol{N} = \boldsymbol{n}\boldsymbol{n}^{\intercal}$ and $\boldsymbol{N}^{\perp} = \boldsymbol{I} - \boldsymbol{N}$ are normal and in-plane projectors with $\boldsymbol{n}$ being the membrane surface normal vector [136], $\hat{\boldsymbol{\epsilon}}_{\text{nn}}$ is the normal strain component in the normal direction, and $\boldsymbol{\epsilon}_{\text{pp}} = \boldsymbol{N}^{\perp}\boldsymbol{\epsilon}\boldsymbol{N}^{\perp}$ is the in-plane strain. The unknown $\hat{\boldsymbol{\epsilon}}_{\text{nn}}$ is determined by applying the plane-stress assumption to the normal component of stress, which yields

$$\hat{\boldsymbol{\epsilon}}_{\text{nn}} = \frac{-\lambda}{\lambda + 2\mu}\text{Tr}(\boldsymbol{\epsilon}_{\text{pp}}). \tag{4.18}$$

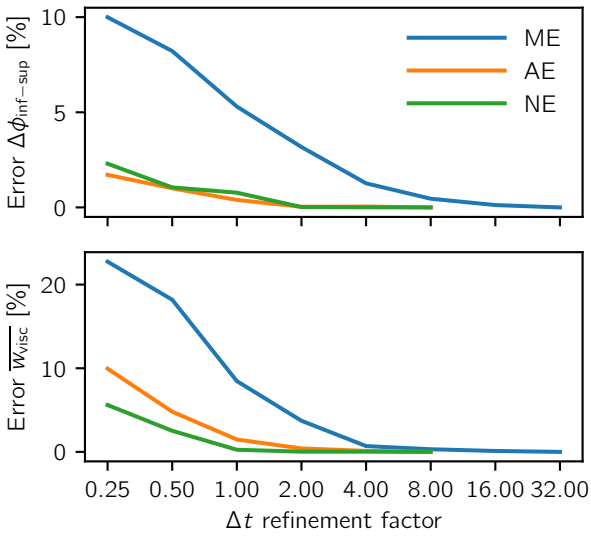

Figure 4.3: Viscous dissipation and mucosal wave phase shift dependence on time step refinement. A refinement factor f corresponds to a time step $\Delta t = 1 \times 10^{-5}\,\text{s}/f$

The constitutive relation for a thin plane-stress membrane then becomes

$$\boldsymbol{\sigma}_{\text{mem}} = 2\mu\boldsymbol{\epsilon}_{\text{pp}} + \frac{2\mu\lambda}{\lambda + 2\mu}\text{Tr}(\boldsymbol{\epsilon}_{\text{pp}})\boldsymbol{N}^{\perp} \tag{4.19}$$

where $\mu = E_{\text{mem}}/(2(1+\nu_{\text{mem}}))$, $\lambda = E_{\text{mem}}\nu_{\text{mem}}/((1+\nu_{\text{mem}})(1-2\nu_{\text{mem}}))$, and E_{mem} and ν_{mem} are the Young's modulus and Poisson's ratio used to parameterize Equation (4.19). The strain energy contribution of the membrane is finally given by

$$\int_{\partial\Omega_{\text{mem}}} \boldsymbol{\sigma}_{\text{mem}}{:}\boldsymbol{\epsilon}_{\text{pp}}(\delta\boldsymbol{u}) d_{\text{mem}}\,\text{d}s \tag{4.20}$$

where d_{mem} is the thickness of the membrane. To incorporate the effect of the membrane, Equation (4.20) is added to the left hand side of Equation (4.1).

Note that the membrane/plane-stress assumption reduces a 3D state to effectively 2D within the plane of the membrane. Further application of the plane-strain approximation results in an effectively 1D state for the membrane. In the discussion above, the stresses and strains ($\boldsymbol{\epsilon}$, $\boldsymbol{\sigma}$) follow the plane-strain assumption (effectively 2D) so the membrane approximation reduces the epithelium to a 1D effect.

4.3.2 Membrane model validation

The membrane model is validated against the FTE model, considered herein as the "ground truth". Validation simulations were conducted for $d_{\text{cov}} = 0.025\,\text{cm}$, $0.05\,\text{cm}$, and $0.075\,\text{cm}$, $E_{\text{slp}} = 4\,\text{kPa}$ and $E_{\text{epi}} = 100\,\text{kPa}$. Figure 4.4 compares the mode shapes for the ME and FTE models for $d_{\text{cov}} = 0.05\,\text{cm}$, and Table 4.4 presents quantitative data on the modal frequencies for all cases. Agreement between the FTE and ME models is excellent,

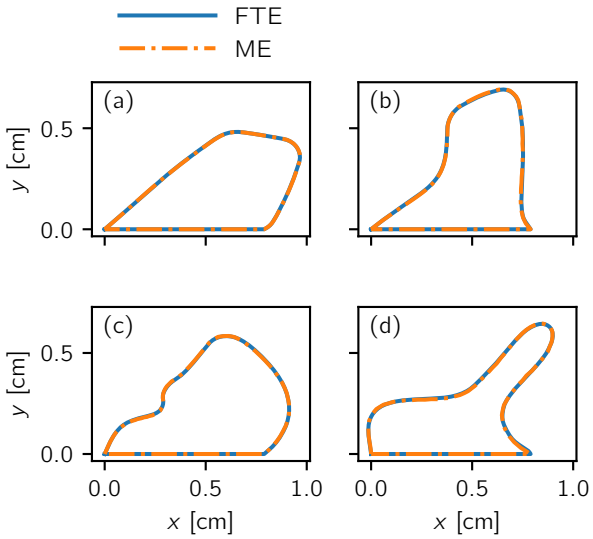

Figure 4.4: Modes (a) 1, (b) 2, (c) 3, and (d) 4 for the FTE and ME epithelium models at $(E_{\text{slp}}, E_{\text{epi}}, d_{\text{cov}}) = (4\,\text{kPa}, 100\,\text{kPa}, 0.05\,\text{cm})$. Mode shapes overlap each other so as to be nearly indistinguishable. Note that only positive eigenmode shapes are shown for clarity

with frequency differences typically less than 2 Hz for Mode 1 and indistinguishable mode shapes. A steady-state oscillation simulation was also conducted and resulted in similar glottal width waveforms (omitted here for brevity). Frequencies derived from the FTE and ME glottal width signals for the steady-state oscillations with $d_{\text{cov}} = 0.05\,\text{cm}$ were both 270 Hz, which aligns well with the modal analysis results.

As a comparison of computational time improvement, on a Ryzen Threadripper 2950x processor with 125 GB of RAM, solution of the FTE model took approximately 3200 min while the ME model took approximately 240 min. The ME model improves simulation

Table 4.4: Modal frequency comparison for the FTE and ME epithelium models for $(E_{\text{slp}}, E_{\text{epi}}, d_{\text{cov}}) = (4\,\text{kPa}, 100\,\text{kPa}, 0.05\,\text{cm})$

	d_{cov}[cm]	Units	Mode 1	Mode 2	Mode 3	Mode 4
FTE	0.025	Hz	118.3	238.9	268.2	375.8
ME			118.6	239.7	269.5	377.0
FTE	0.050	Hz	113.4	231.7	258.7	364.7
ME			113.6	232.1	259.5	365.3
FTE	0.075	Hz	108.1	222.0	246.4	342.5
ME			108.4	222.5	247.2	343.5

times due to lower mesh density requirements at the epithelium layer, so the exact speedup will depend on the specific mesh used and geometry of the problem.

4.4 Results

Herein we present results on the influence of epithelium treatment on VF kinematics and kinetics. An exemplar case is first considered to compare modeling strategies, followed by a parametric study considering a range of epithelium stiffness and thickness values. Specifically, in the first section a detailed comparison of all three epithelium treatments (AE, ME, NE) is presented. The second and third sections present changes between the AE and ME models over parameter variations in terms of kinematic and kinetic quantities for the stiff and soft SLP conditions, respectively. We note that the ME model is employed in lieu of the more computationally expensive FTE model when considering discrete treatment of the epithelium since it was found previously that these two frameworks agree well (see Section 4.3).

4.4.1 Comparison of epithelium modeling strategies

In this section we compare the ME, AE, and NE epithelium models for a single case with $(E_{\text{epi}}, d_{\text{cov}}) = (100\,\text{kPa}, 0.05\,\text{cm})$ for the stiff SLP ($E_{\text{slp}} = 0.5\,\text{kPa}$) condition. Figure 4.5 shows results from modal analysis, comparing the Distinct representation (ME model) with the Integrated representations (NE and AE models). While the first mode shape is very similar across models, higher modes tend to deviate more. Qualitatively, the AE and ME models show greater similarity than the NE and ME models, which is unsurprising, as

the NE model completely neglects the epithelium and thus has considerably lower overall system stiffness.

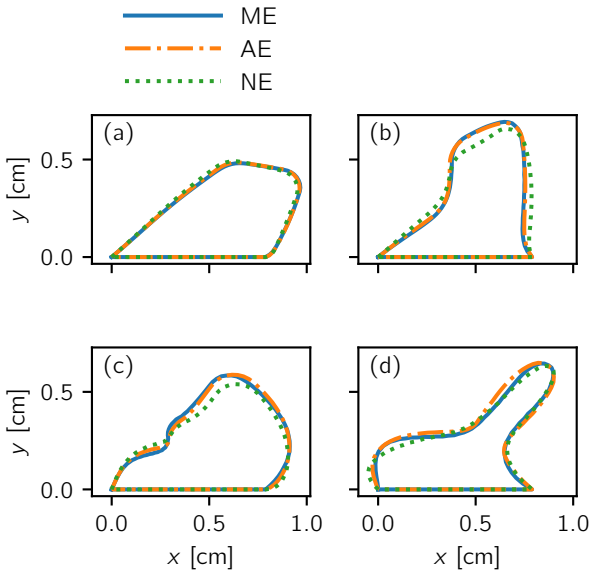

Figure 4.5: Modes (a) 1, (b) 2, (c) 3, and (d) 4 of the ME, AE, and NE models. Note that only positive eigenmode shapes are shown for clarity

Table 4.5 summarizes modal frequencies and the relative error between mode shapes of the models, which confirm the trends of Figure 4.5. In terms of both mode shapes and frequencies, the AE model generally compares reasonably well with the ME model, with the first two modes having errors of under 8 %. The mode shapes of all three models also qualitatively agree with modes seen in previous studies, with the first mode showing an inferior-superior motion, the second mode a medial-lateral motion, and the third mode a converging-diverging motion [66].

Figure 4.6 shows phase-aligned period-normalized glottal width signals of the three models during steady-state oscillations[3]. While all three cases have qualitatively similar glottal width waveforms, fundamental frequencies and waveform shapes differ. Specifically, the AE model has the highest fundamental frequency, followed by ME then NE, which agrees with the results from modal analysis.

[3]The signals are aligned such that the cross-correlation between signal pairs is maximized.

Table 4.5: Modal frequencies and nodal errors between mode shapes.

	Units	Mode 1	Mode 2	Mode 3	Mode 4
ME	Hz	113.6	232.1	259.5	365.3
AE	Hz	114.6	233.9	262.5	375.4
NE	Hz	103.8	214.3	245.3	355.9
err $(\boldsymbol{b}_{\mathrm{ME}}, \boldsymbol{b}_{\mathrm{AE}})$	%	3.7	7.8	9.6	11.7
err $(\boldsymbol{b}_{\mathrm{ME}}, \boldsymbol{b}_{\mathrm{NE}})$	%	12.3	40.1	32.2	15.0

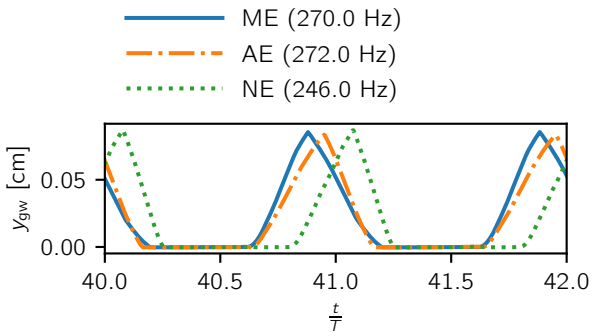

Figure 4.6: Comparison of the glottal width signals for the ME, AE, and NE models over two oscillation cycles, where T is the oscillation period

Table 4.6 quantitatively compares salient glottal width waveform features and kinetic quantities for the ME, AE, and NE models. Evident from Figure 4.6 and borne out in the quantitative results, all three models have similar glottal width amplitudes. In terms of kinematics, however, Figure 4.6 shows that the NE model has the shortest open time. The ME model has the smallest speed quotient, which differs from the other two models by about a factor of two. This also influences MADR, for which the ME model has the lowest magnitude. The inferior-superior excursion of the models, max $u_{\text{inf-sup}}$, is considerably more pronounced for the NE model. Values for OQ are roughly comparable with normative values observed in past studies while SQ is noticeably smaller for all models, and the ME model in particular [132]. In terms of medial surface motion, the mucosal wave phase shift is smallest for the ME model, followed by the AE, then NE models. The mucosal wave speed follows the reverse trend with ME having the highest mucosal wave speed, followed by AE, then NE. Values for mucosal wave phase difference agree with the range of phase differences reported for canine larynges in past studies [133]. In contrast, values for mucosal wave speed are generally larger than reported values from the same study; however, mucosal

wave speed generally increases with increasing fundamental frequency and the fundamental frequencies in this study exceed those observed for the reported values [133].

Measures associated with VF kinetics generally differ across the three models. Viscous dissipation, w_{visc}, is considerably lower for the AE model, whereas mean contact pressure and von Mises stresses are the highest for this model.

Table 4.6: Common clinical measures and other kinematic and dynamic quantities computed from the self-oscillating simulations. Normative values for OQ, SQ represent the range of values between the average male and female speaker in [132, Table A1 and Table A2]. Normative values for $\Delta\phi_{\text{inf}-\text{sup}}, c_{\text{mucosa}}$ represent the range between minimum and maximum values in Titze et al. [133, Table 1] for canine larynges

	Unit	ME	AE	NE	Normative values
OQ	-	0.552	0.508	0.432	0.6 – 0.76
SQ	-	0.792	1.4	1.5	1.65 – 1.82
MADR	$\text{cm}\,\text{s}^{-2}$	98.1	126.0	141.8	-
amplitude	cm	0.087	0.084	0.087	-
$\Delta\phi_{\text{inf}-\text{sup}}$	$^\circ\,\text{cm}^{-1}$	326.6	352.2	494.5	245 – 610
c_{mucosa}	$\text{cm}\,\text{s}^{-1}$	297.6	278.0	179.1	58.7 – 217.7
max $u_{\text{inf-sup}}$	cm	0.089	0.099	0.131	-
$\overline{w_{\text{visc}}}$	erg	13624	8349	16098	-
$\overline{p_{\text{coll}}}$	kPa	1.7	2.3	1.4	-
$\overline{\sigma_{\text{vm}}}$	kPa	0.492	1.0	0.575	-

4.4.2 Parametric study of epithelium stiffness and cover depth for a stiff SLP

In this section we compare behaviors of the ME and AE models, the latter of which is commonly employed in FEM simulations of the VFs, across a range of epithelium stiffness, E_{epi}, and cover thickness, d_{cov}, values for $E_{\text{slp}} = 4\,\text{kPa}$ (stiff SLP).

Kinematic quantities are summarized in Figure 4.7. Figure 4.7(a) shows that fundamental frequency, F_{o}, increases with epithelium stiffness and decreases with cover layer thickness for both models. The AE model exhibits a larger increase in F_{o} with E_{epi} and has higher F_{o} for the same d_{cov} in comparison with the ME model. Figure 4.7(b) presents the open quotient, which generally increases with epithelium stiffness for both models. The

open quotient for the AE model is more sensitive to cover layer thickness than is the ME model, as evidenced by the greater spread in open quotient for a given epithelial stiffness. For the thickest cover, $d_{\text{cov}} = 0.075\,\text{cm}$, the AE model exhibits a smaller open quotient than the ME model for all stiffnesses. Notably, across both (a) and (b), the AE model with $(E_{\text{epi}}, d_{\text{cov}}) = (200\,\text{kPa}, 0.025\,\text{cm})$ diverges from the trends of other cases, exhibiting by far the highest F_{o} and an open quotient near unity due to lack of self-oscillation in this case.

Figure 4.7(c) shows the maximum inferior-superior displacement of the VFs. For both ME and AE models, increasing cover depth consistently leads to larger inferior-superior displacements, while increasing epithelial stiffness decreases the excursions. Displacements between the two models are similar, with the largest departure occurring for the aforementioned lack of self-oscillation of the AE model when $(E_{\text{epi}}, d_{\text{cov}}) = (200\,\text{kPa}, 0.025\,\text{cm})$.

Figure 4.7(d) shows the mucosal wave phase differences. Similar to the inferior-superior displacement, increasing cover depth increases the mucosal wave phase difference while increasing epithelium stiffness decreases the phase difference. Medial surface profile snapshots through one oscillation cycle for varying epithelium stiffness are also shown in Figure 4.8.

Figure 4.9 summarizes dynamic quantities. Figure 4.9(a) presents average contact pressure over the duration of contact. Differences between the ME and AE models in terms of contact pressure are generally consistent, with the ME model typically exhibiting lower contact pressures for a given parameter set. The noted exception is for $(E_{\text{epi}}, d_{\text{cov}}) = (200\,\text{kPa}, 0.025\,\text{cm})$, for which the contact pressure of the AE model is nearly zero, in line with the near unity open quotient for this case shown in Figure 4.7(b). Figure 4.9(b) shows the ME model consistently has higher average viscous dissipation, indicating that more energy is damped in the SLP layer. Interestingly, viscous dissipation decreases with increasing epithelium stiffness for the AE model, while remaining relatively unchanged for the ME model. Figure 4.9(c) shows the average von Mises stress in the SLP also follows a consistent trend where values from the AE model are larger and more strongly dependent on cover thickness than those for the ME model.

4.4.3 Parametric study of epithelium stiffness and cover depth for a soft SLP

Analogous to Figure 4.7, Figure 4.10 presents kinematic quantities for the ME and AE models, but for the soft SLP case ($E_{\text{slp}} = 0.5\,\text{kPa}$). General trends and relations between the ME and AE models are similar to those identified for the stiff SLP in Figure 4.7. For F_{o},

increasing epithelium stiffness generally increases F_o, and F_o for the AE model is greater than for the ME model, except at $(E_{epi}, d_{slp}) = (50\,\text{kPa}, 0.075\,\text{cm})$. In this case the vocal folds did not self-oscillate resulting in deviations in trends for the other measures as well. Similar to the stiff SLP condition, open quotient generally increases with increasing E_{epi}, and greater spread between d_{cov} values for the AE model is observed. Inferior-superior displacement and mucosal wave phase difference also tend to decrease with increasing epithelium stiffness or decreasing cover depth for both ME and AE models.

Figure 4.11 shows dynamic quantities for the soft SLP case, analogous to Figure 4.9 for the stiff SLP. Dynamic trends are likewise similar to those in Figure 4.9. For p_{coll} (Figure 4.11(a)) increasing epithelium stiffness or decreasing cover depth tends to increase mean collision pressures. In addition, for a given epithelium stiffness, the AE model tends to have a higher contact pressure, as also seen in Figure 4.9(a). In the case of w_{visc}, Figure 4.11(b) shows that the ME model has greater viscous dissipation than the AE model (similarly seen in Figure 4.9(b)). Interestingly, Figure 4.11(b) does not show a spread in viscous dissipation for the AE model with cover depth as seen in Figure 4.9(b), which could be a product of the lower subglottal pressure used in the soft SLP condition. For the mean von Mises stress (Figure 4.11(c)), the AE model again has greater stress magnitudes compared to the ME model, as also seen in Figure 4.9(c).

4.5 Discussion

Treating the epithelium as an infinitesimally thin layer using the membrane model results in nearly identical mode shapes and modal frequencies as arise with a thin-but-finite epithelial layer (see Figure 4.4 and Table 4.4). The FTE treatment is more computationally expensive, as it requires small elements to resolve the epithelial layer and is thus susceptible to shear-locking [65, Section 5.4]. Modeling thin structures as plates/shells is a common strategy in solid mechanics, including, for example, Kirchhoff-Love and Reisnner-Mindlin plate models [134], which include both bending and membrane type effects in the plate. Application to VF modeling enables a computationally efficient manner in which to include a discrete epithelium. We note that there does exist a small geometric discrepancy between the membrane approximation and a finite epithelium thickness. While this can be ameliorated by moving the membrane mid-surface away from VF surface, we chose the current treatment to ensure identical external geometries between the ME and AE/NE models to facilitate quantitative comparison between mode shapes. The FTE treatment, by virtue of a finite-yet-small epithelium thickness, has a slightly thinner SLP layer, which may contribute to the minor differences between the two models in Table 4.4.

Neglecting the epithelium entirely (NE model) significantly alters the VF dynamics. The NE model exhibits consistently lower frequencies in both modal analysis and the glottal width signal compared to the Distinct models (see Figure 4.6 and Table 4.5), likely due, in part, to the reduction in overall system stiffness. Furthermore, the mode shapes are notably different from the ME model, particularly for the higher modes, as noted by the NE modal errors in Table 4.5. Likely due to the lower system stiffness, it exhibits the most significant levels of inferior-superior excursion, shows the greatest mucosal wave phase difference, and lowest mucosal wave speed (see Table 4.6). These results agree with prior studies using silicone VF models, wherein incorporating an epithelium was found to reduce inferior-superior motion and increase glottal closure [139–142].

Accounting for the epithelium by integrating it into the cover layer (Integrated; AE model) results in mode shapes and modal frequencies that better align with the Distinct ME model behavior (Figure 4.5 and Table 4.5). The modal frequencies are slightly higher (about 1.0 % for modes 1 to 3) and the error in the first three mode shapes is less than 10 %. The frequency of the glottal width signal in Figure 4.6 is 1 % higher for the AE model while amplitudes are similar. The inferior-superior excursion for the AE model is within 11 % of the ME model (Table 4.6). Contact pressure and viscous dissipation for the AE model are significantly different (an increase of 35 % and decrease of 39 % respectively compared to the ME model), however. Mean von Mises stress for the AE model is also different, with an increase of 100 % compared to the ME model. These parameters are associated with details of the strain and stress fields within the SLP (see Equations 4.15 and 4.16), which are impacted by the change in SLP stiffness associated with the AE model. Thus, while the global dynamics are similar with the Distinct representation, the Integrated methodology does alter local details, which may have implications in certain scenarios, such as stress-induced fluid migration within the folds [143], and dose measures for VF damage, including collision and dissipation dose [144–146].

Though the Distinct and Integrated epithelium methods yield similar modal analysis results, details of the kinematics and kinetics of the ME (Distinct) and AE (Integrated) models differ with epithelium stiffness and cover thickness. As expected, fundamental frequency in both frameworks generally increases with epithelium stiffness, but the effect is more pronounced for the AE model (Figure 4.7(a) and Figure 4.10(a)). The thinner cover layer cases have higher overall stiffness due to a shift in the relative contribution of the epithelium in the weighted average, thus also increasing fundamental frequency. Interestingly, the same does not occur for the ME model, despite the same nominal overall stiffness. Mucosal wave phase differences for the ME and AE models generally appear similar for most conditions, although this effect is also mediated by cover depth and SLP thickness. For the thickest cover layer and soft SLP condition, the ME model demonstrated

a noticeably larger inferior-superior displacement (see Figure 4.10(c)), likely due to the extreme pliability of the SLP in this condition.

Consistent differences in kinetic quantities further differentiate the AE and ME models and are hypothesized to be the result of the difference in SLP stiffness between the ME and AE models. Specifically, due to the averaging in the AE model, it has a stiffer SLP than the ME model and the difference increases as the epithelium becomes stiffer and the cover thins. The ME model has consistently lower contact pressures than the AE model, which is consistent with the findings of Gunter [147] that lower SLP stiffness led to lower contact force. This suggests SLP stiffness could play a role in VF injury risk [147].

The von Mises stress in the SLP (Figure 4.9(c) and Figure 4.11(c)) for the ME model was also lower than for the AE model, which is consistent with the findings of Gunter [147]. The ME model had greater viscous dissipation in the SLP (Figure 4.9(b) and Figure 4.11(b)) than the AE model due to the softer SLP leading to larger deformations under similar external forces. These results suggest that modeling a discrete epithelium is important when considering internal stresses and strains, and surface contact pressures.

Comparing predicted values to normative values reported in the literature in Table 4.6, we observe reasonable agreement in terms of OQ, but predict consistently lower SQ for all models, with the ME model having the lowest value. One reason for this is the lack of acoustics in our model which can prolong the opening phase and shorten the closing phase to increase the speed quotient by delaying the peak of the flow pulse [51]. This could also indicate our selection of model parameters and geometry resulted in a non-ideal modal voice. Lastly while the SQ in our studies is lower than reported physiological ranges, some silicone VF studies conducted with an epithelium have also shown low speed quotients ([141, Figure 5] and [140, Figure 11]) suggesting this could be a feature of modeling an epithelium for some model parameter/geometry combinations.

There are a few limitations of the current work worth noting. (i) Acoustics were not included in this study. Preliminary studies conducted using a wave-reflection-analog approach (not shown) found that acoustic coupling effects were sensitive to fundamental frequency of the flow waveform. Since the discrete SLP/epithelium and integrated cover models display consistent differences in frequencies, this often led to larger discrepancies between the models. Acoustics were not included here so as not to obscure the influence of the epithelium modeling approach. (ii) The choice of model used here was also limited. A 2D model with 1D glottal flow was selected for simplicity. Notably, 3D geometries will have different mode shapes from similar 2D geometries. This could impact our results if, for example, a 3D geometry led to different qualitative mode shape motions between the ME, AE, and NE models. In the current study, each mode number corresponded to the same

qualitative motion (for all of the ME, AE, and NE, mode 1 was an inferior-superior mode, mode 2 a medial-lateral mode, etc). For example, Xue et al. [148] found that changes in cover thickness for a 3D model based on the M5 geometry could lead to changes in the mode order, which suggests similar changes could also happen for variations in layer stiffness between the ME, AE, and NE models. The resulting differences between the three models in these conditions requires further investigation. (iii) A single VF geometry (M5) was investigated. A silicone VF study found model geometry can significantly impact the resulting dynamics [127, 149]. As a result, it is likely that for specific parameter sets and geometries there could be large differences between the epithelium models due to, for example, a bifurcation where a Distinct model converges to a qualitatively different oscillation from Integrated models. For modal oscillations where the different epithelium modeling approaches all experience typical modal oscillations, we expect the models to reflect the general trends here since they are mostly related to the difference in SLP stiffness rather than the particular motion of the VF. However, more physiologically-representative motion may be obtained for a given epithelium model by considering an alternate VF geometry, and as such the robustness of the findings herein to VF geometry should be considered in future studies. (iv) We found increasing contact pressure with increasing epithelium stiffness; however, this is likely not a general observation since contact pressure depends on numerous factors, including VF internal layer shapes, surface geometry, and material properties, to name a few. This is shown, for example, by Zhang [150] who noted that contact pressure can either increase or decrease with decreasing glottal gap depending on VF cover thickness, glottal angle, and subglottal pressure. For different model parameters contact pressure trends may vary.

4.6 Conclusions

Vocal fold models that include the SLP and epithelium as distinct layers of the cover have important differences compared to those that integrate the two layers into a single cover. When the epithelium stiffness is neglected in the single cover, fundamental frequency tends to be lower, inferior-superior motion higher, and significant qualitative changes in kinematics are also apparent. In contrast, when the epithelium and SLP are averaged into a single cover, fundamental frequency, inferior-superior motion and qualitative kinematics show greater agreement with the distinct layer models. However, clinically relevant parameters, including contact pressure and internal SLP stresses, tend to differ depending on epithelium treatment, with the integrated epithelium models tending to predict larger internal stresses and contact pressures. Differences between integrated and distinct epithelial mod-

els can also be exacerbated by changes in epithelial stiffness and cover depth. Thus, if the aim of a finite element study is to explore or utilize internal stresses/strains in the vocal folds, as for vocal dose measures, care should be taken in treating the epithelium. When considering a distinct epithelium treatment, the membrane model introduced in the manuscript can be employed with minimal additional computational cost.

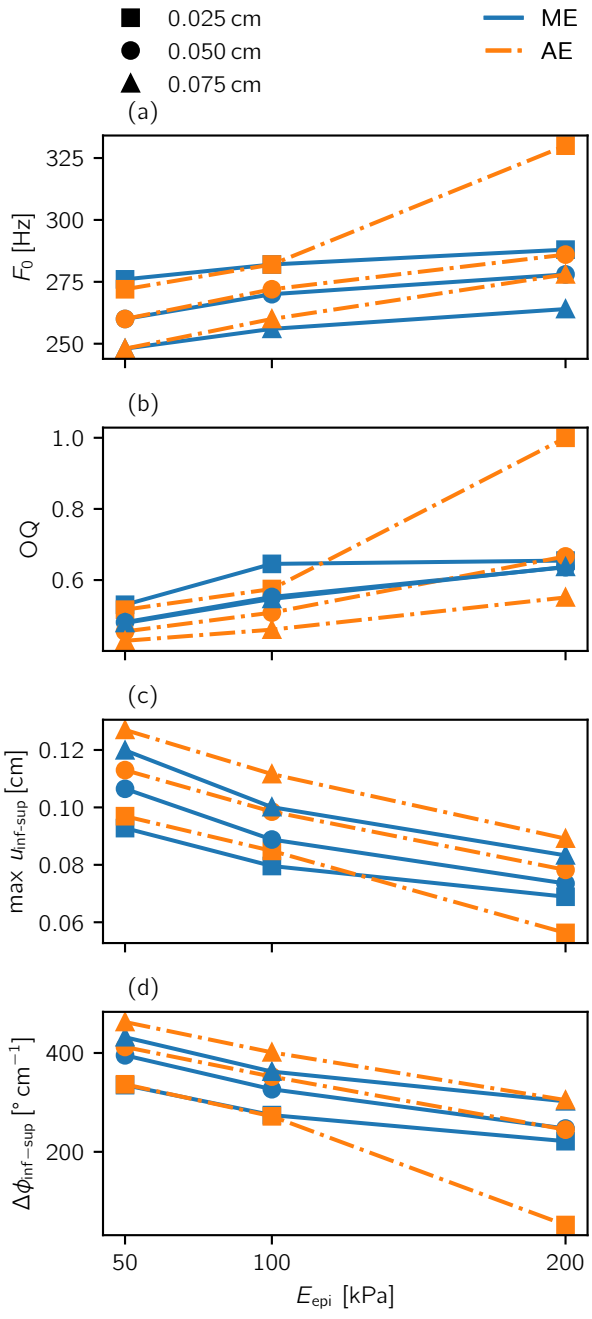

Figure 4.7: Comparison of (a) fundamental frequency, (b) open quotient, (c) maximum inferior-superior displacement, and (d) mucosal wave phase difference over the range of epithelium stiffness and cover thickness values for the ME and AE models for $E_{\text{slp}} = 4\,\text{kPa}$

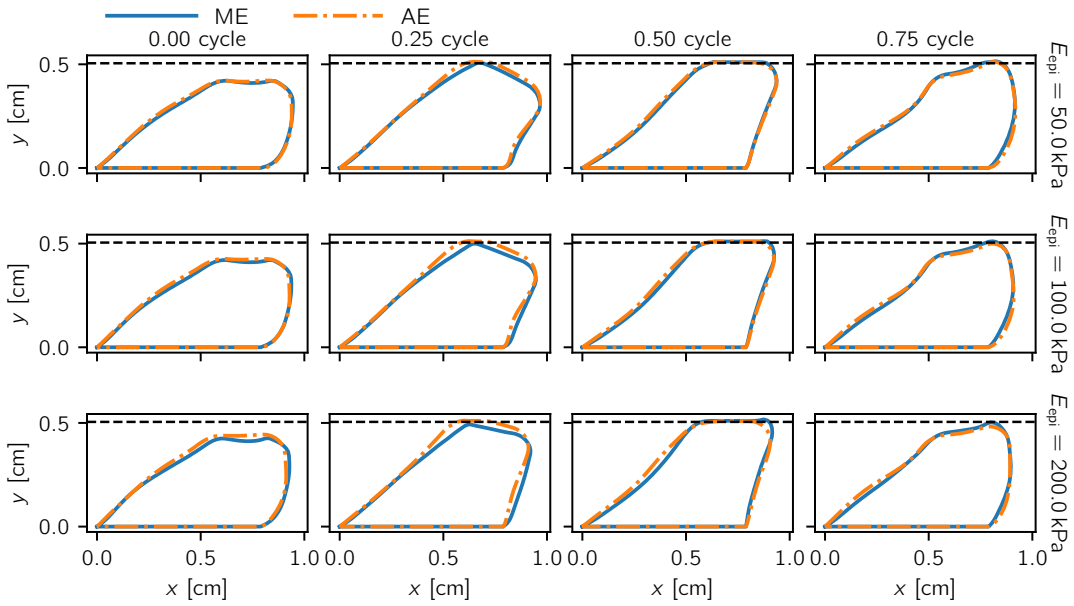

Figure 4.8: Snapshots at 4 instances throughout one steady state oscillation cycle of the ME and AE models at $d_{\text{cov}} = 0.05\,\text{cm}$ and $E_{\text{slp}} = 4\,\text{kPa}$. The start point of each cycle corresponds to the time of the maximum glottal width

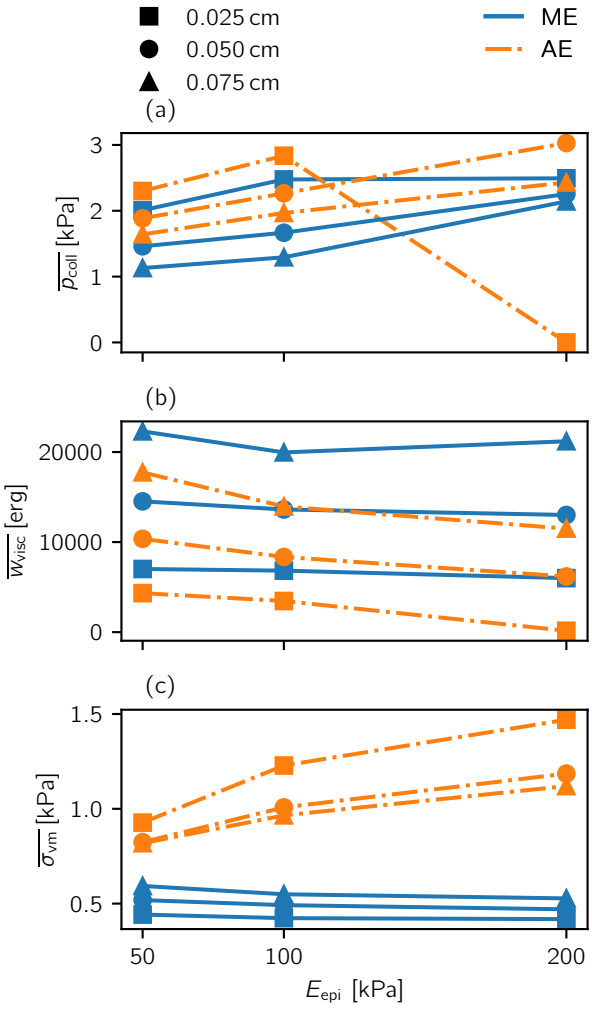

Figure 4.9: Comparison of average (a) contact pressure, (b) viscous energy dissipation in the SLP, and (c) von Mises stress over a range of epithelium stiffness and cover thickness values for the ME and AE models for $E_{\text{slp}} = 4\,\text{kPa}$

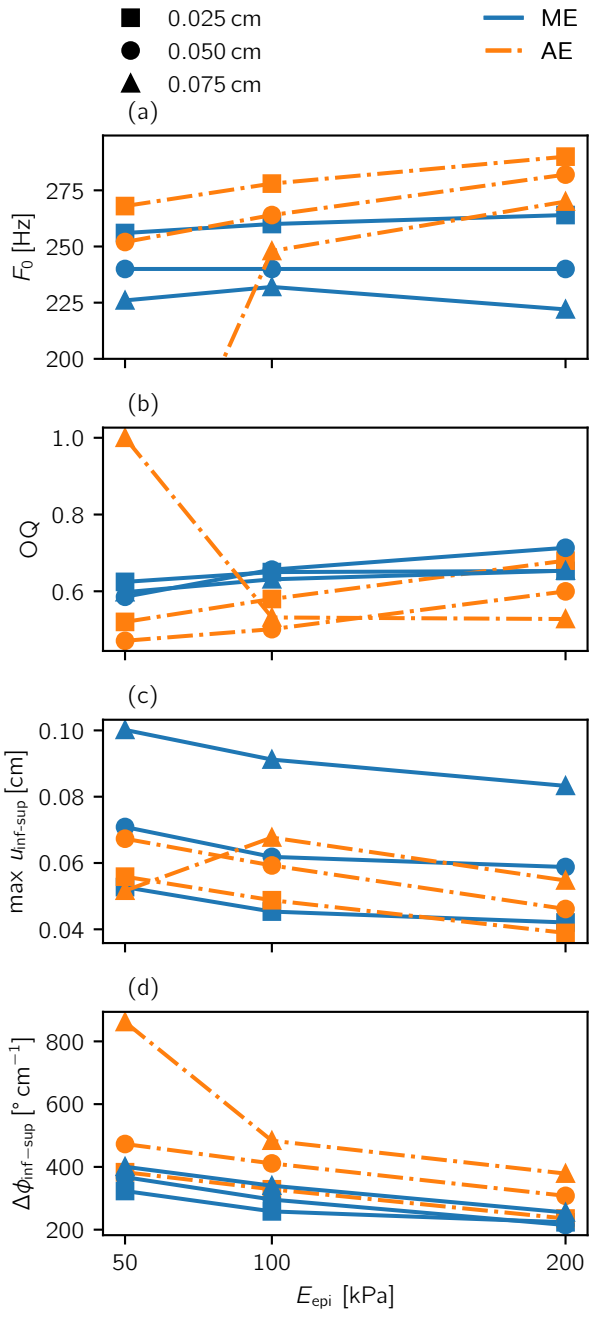

Figure 4.10: Comparison of (a) fundamental frequency, (b) open quotient, (c) maximum inferior-superior displacement, and (d) mucosal wave phase difference over the range of epithelium stiffness and cover thickness values for the ME and AE models for $E_{\text{slp}} = 0.5\,\text{kPa}$

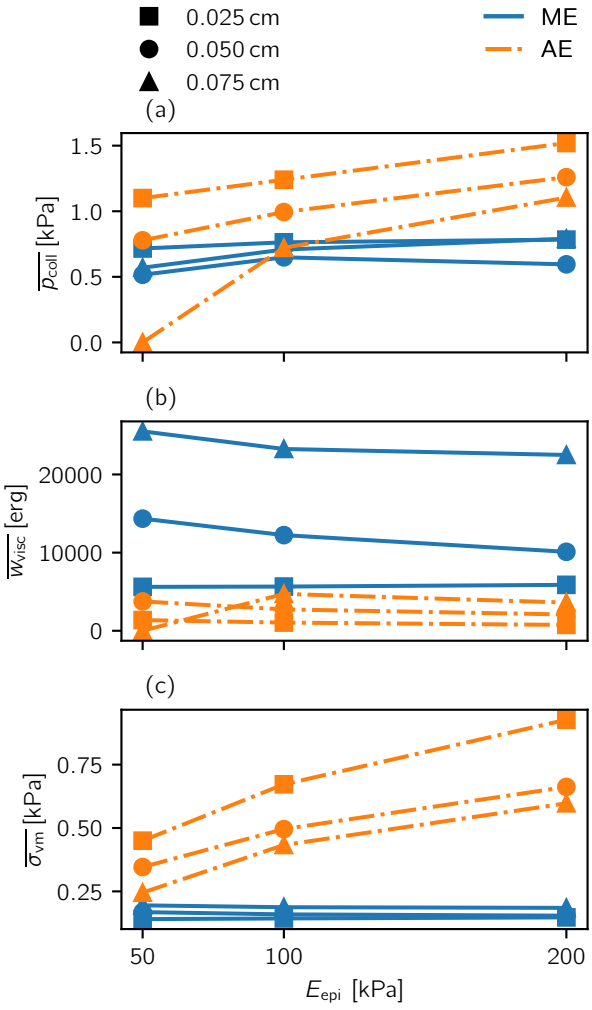

Figure 4.11: Comparison of average (a) contact pressure, (b) viscous energy dissipation in the SLP, and (c) von Mises stress over a range of epithelium stiffness and cover thickness values for the ME and AE models for $E_{\text{slp}} = 0.5\,\text{kPa}$

Chapter 5

The effect of swelling on vocal fold kinematics and dynamics [1]

5.1 Introduction

This chapter presents the development of a finite element VF swelling model and its analysis to explore the effects of fluid retention in the VFs on phonotrauma and voice outputs. The developed model is used to study how swelling changes voice outputs and phonotrauma to gauge whether and how swelling could incur a vicious cycle that leads to PVH. Specifically it is hypothesized that if swelling increases phonotrauma and results in detrimental voice output changes, then a vicious cycle can form through mutually reinforcing compensatory adjustments for voice output changes and increased phonotrauma with the resulting swelling.

The chapter is organized as follows. Section 5.2 discusses the model setup, study design, and swelling model implementation; further details on the derivation of the swelling model are given in Appendix B.1. Section 5.3 presents the simulation results. Section 5.4 discusses the significance of the results, analyzes why swelling leads to the observed results,

[1] This work was co-authored by Sean D. Peterson (my advisor), Byron D. Erath, and Matías Zañartu. I developed the code, performed the simulations, analyzed data, generated figures, and wrote the first draft of the manuscript. BDE and MZ contributed to conceptualization and reviewed the manuscript. SDP contributed to conceptualization, supervised the work, and reviewed the manuscript. Part of this chapter was published as an article to Biomechanics and Modeling in Mechanobiology [2].

and discusses study limitations. Finally, Section 5.5 summarizes salient findings from this work.

5.2 Methodology

Herein we consider a two-dimensional (2D) representation of the VFs, as shown in Figure 5.1, discretized with the finite element method (FEM), which has been shown to compare well with experimental silicone VF studies [118]. The VF geometry is based upon the M5 model [119] (note the VF thickness is 5 mm, which is shorter than the physical model shown in [119]) and left-right symmetry is assumed, such that only one VF need be considered. The internal VF structure is divided into body, cover, and epithelium layers [40], each with distinct nominal Young's moduli given by E_{body}, E_{cover}, and E_{epi}, respectively. This subscript convention is used throughout the remainder of the manuscript. All layers share the same nominal density ρ_{vf}. The internal VF domain is denoted Ω with boundary $\partial\Omega$. The body and cover domains are denoted Ω_{body} and Ω_{cover}, respectively, such that $\Omega = \Omega_{\text{body}} \cup \Omega_{\text{cover}}$. The epithelium is treated as a membrane and thus has zero area [1].

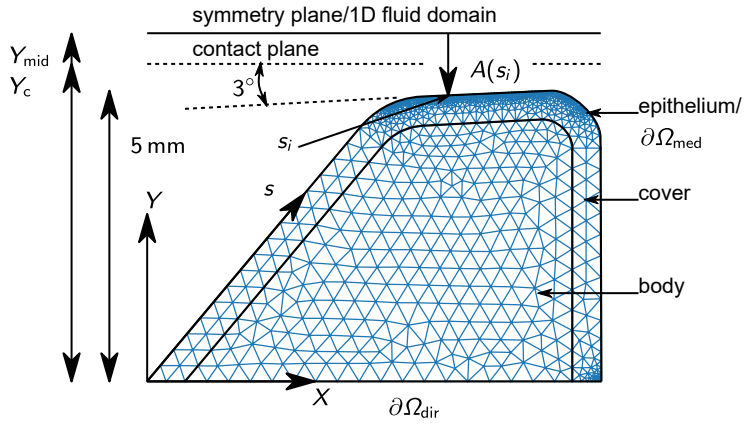

Figure 5.1: Schematic of the vocal fold geometry in the reference configuration with representative finite-element discretization. Two finite thickness layers are indicated by 'body' and 'cover' whereas the 'epithelium' layer is treated as a membrane (infinitesimally thin) along the surface $\partial\Omega_{\text{med}}$. Material coordinates $\boldsymbol{X} = (X, Y)$ and s indicate 2D coordinates and medial surface/1D fluid domain coordinates, respectively; i denotes nodal indices along the medial surface. The glottal area is denoted by a (half the glottal area is shown due to symmetry)

A Cartesian coordinate system for the reference configuration, $\boldsymbol{X} \in \mathcal{R}^2$, is defined with origin on the tracheal wall at the inferior margin of the VF as shown in Figure 5.1. An additional surface coordinate, $s \in \mathcal{R}$, is defined along the VF boundary that is contact with the fluid, denoted as $\partial\Omega_{\text{med}}$ (note, this corresponds to the surface comprising the epithelium membrane). The fixed (Dirichlet) VF boundary region at the interface with the tracheal wall is denoted $\partial\Omega_{\text{dir}}$ such that $\partial\Omega = \partial\Omega_{\text{dir}} \cup \partial\Omega_{\text{med}}$.

Aerodynamic loading on the VF assumes the driving flow to be inviscid, incompressible, quasi-steady, and one-dimensional (1D) such that Bernoulli's equation can be computed along the centerline streamline then imposed upon the VF surface. The influence of acoustic loading on the VF dynamics is assumed negligible, *i.e.*, only level 1 interactions [51] are considered.

Models for the glottal flow and VFs were chosen as a balance of fidelity and computational simplicity, to make parametric studies feasible with available resources. A 2D model, while it will not capture 3D effects, has been shown to compare well with experimental silicone VF studies [118] and likely is applicable to situations with long VFs where the plane-strain assumption approximately applies. Similarly, 1D models of the glottal flow are computationally simple but compare qualitatively well with more complicated 2D Navier-Stokes based models [71]. These simplifications were considered reasonable since the focus of our study is to determine if general effects of swelling can trigger a vicious cycle, rather than to make accurate quantitative predictions.

5.2.1 Finite element formulation

Let the reference configuration (Figure 5.1) with coordinates $\boldsymbol{X}$ correspond to the unswollen, unstressed state of the VFs. While deformations of the VFs are normally small enough to justify the small strain assumption, the constitutive model for swelling (described in detail in Appendix B.1) results in pre-stress for the material constitutive response in the reference configuration, which invalidates the small-strain assumption. As a result, we assume large deformations for the material strain energy (which includes the effect of swelling) and small deformations for remaining terms; the weak form of conservation of linear momentum for the solid domain Ω then follows from the principle of virtual work, see Bathe [65, Chapter

4 and Chapter 6], for example. In the present case this yields

$$\begin{aligned}&\int_{\Omega} \rho(v)\ddot{\boldsymbol{u}}\cdot\delta\boldsymbol{u} + \boldsymbol{S}(\boldsymbol{E},v):\delta\boldsymbol{E} + \eta\dot{\boldsymbol{\epsilon}}:\delta\boldsymbol{\epsilon}\, d\boldsymbol{X}\\ &+ \int_{\partial\Omega_{\text{med}}} \boldsymbol{\sigma}_{\text{epi}}:\delta\boldsymbol{\epsilon}_{\text{epi}} d_{\text{epi}}\, ds\\ &\quad = \int_{\partial\Omega_{\text{med}}} \boldsymbol{t}\cdot\delta\boldsymbol{u}\, ds \text{ for all } \delta\boldsymbol{u} \in \boldsymbol{V}^2(\Omega),\end{aligned} \tag{5.1}$$

where $\boldsymbol{V}(\Omega)$ is the space of scalar piece-wise linear functions over a triangular mesh (shown in Figure 5.1) equal to 0 on $\partial\Omega_{\text{dir}}$, $\boldsymbol{u}, \boldsymbol{v}, \boldsymbol{a} \in \boldsymbol{V}^2(\Omega)$ are the displacement, velocity, and acceleration vectors, respectively, and $\delta\boldsymbol{u} \in \boldsymbol{V}^2(\Omega)$ is a virtual displacement. Strain tensors $\boldsymbol{E} = 1/2(\boldsymbol{F}^T\boldsymbol{F} - \boldsymbol{I})$ and $\boldsymbol{\epsilon} = 1/2(\boldsymbol{F} + \boldsymbol{F}^T) - \boldsymbol{I}$ are the Green strain and the small strain tensor, respectively, where $\boldsymbol{F} = \partial\boldsymbol{u}/\partial\boldsymbol{X} + \boldsymbol{I}$ is the deformation gradient. Similarly, virtual strains are given by $\delta\boldsymbol{E} = 1/2\left(\delta\boldsymbol{F}^T\boldsymbol{F} + \boldsymbol{F}^T\delta\boldsymbol{F}\right)$ and $\delta\boldsymbol{\epsilon} = 1/2(\delta\boldsymbol{F} + \delta\boldsymbol{F}^T)$, where $\delta\boldsymbol{F} = \partial\delta\boldsymbol{u}/\partial\boldsymbol{X}$ is the virtual deformation gradient. The corresponding stress tensors are the second Piola-Kirchhoff stress tensor, $\boldsymbol{S}$, and the Cauchy stress tensor, $\boldsymbol{\sigma}$.

The strain energy terms $\int_{\Omega} \boldsymbol{S}(\boldsymbol{E},v):\delta\boldsymbol{E} + \eta\dot{\boldsymbol{\epsilon}}:\delta\boldsymbol{\epsilon}\, d\boldsymbol{X}$ are based on an ad hoc modification of the Kelvin-Voigt model to account for swelling. The classical Kelvin-Voigt model gives the Cauchy stress as $\boldsymbol{\sigma} = \boldsymbol{K}\boldsymbol{\epsilon} + \eta\dot{\boldsymbol{\epsilon}}$ [64, 120], where $\boldsymbol{K}\boldsymbol{\epsilon}$ is the elastic stress and $\boldsymbol{K}$ is the elasticity tensor, and $\eta\dot{\boldsymbol{\epsilon}}$ is the viscous stress and η is the viscosity. Using the approach developed in [29, 116, 151], swelling is modelled for hyperelastic materials by modifying the hyperelastic constitutive equation. As a result, we replace the elastic stress in the Kelvin-Voigt model by a hyperelastic material stress with swelling effects while keeping the unmodified viscous term, resulting in

$$\sigma = (\det \boldsymbol{F})^{-1}\boldsymbol{F}\boldsymbol{S}(\boldsymbol{E},v)\boldsymbol{F}^{\intercal} + \eta\dot{\boldsymbol{\epsilon}},$$

where $\boldsymbol{S}(\boldsymbol{E},v)$ is dependent on the swelling field, v, and Green strain, $\boldsymbol{E}$, through the swelling constitutive equation introduced in Section 5.2.2. Note $v = 1$ implies no swelling (no volume change), while $v = 1.2$ represents a 20 % increase in the free volume (volume with no external loading). In the virtual work statement, the viscous stress is a Cauchy stress work-conjugate with the virtual small strain, while the hyperelastic stress is a second Piola-Kirchhoff stress work-conjugate with the the virtual Green strain [152].

The material density ρ in Equation (5.1) requires special consideration in the case of swelling. Since swelling introduces additional mass into the system, ρ is given by

$$\rho = \rho_0 + (v-1)\rho_v, \tag{5.2}$$

where ρ_0 is again the nominal density in the absence of swelling (that is, at $v = 1$) and ρ_v is the density of the incoming material causing the swelling, which is assumed to be water. Per unit volume in the reference configuration, the first term of Equation (5.2) represents the original mass of material and the second term represents the additional mass due to the influx of fluid with swelling. Note that Equation (5.2) considers density in the reference configuration; the density in the deformed configuration will be approximately ρ_0 as the VF volume will increase with swelling.

The first three terms in the first integral of Equation (5.1) represent the virtual work due to inertial forces, material strain energy, and viscous effects. The second integral term in Equation (5.1) represents the strain energy contribution due to an epithelium over the medial surface, where $\boldsymbol{\sigma}_{\text{epi}}$ and $\boldsymbol{\epsilon}_{\text{epi}}$ are the membrane stress and strain tensors, respectively [1, 136]. A separate epithelium was included because past studies found the epithelium to significantly influence VF dynamics [1, 131, 140–142]; furthermore, the epithelium herein acts as an outer barrier that constrains internal swelling, thus affecting the shape of the swollen material. The third term in Equation (5.1) represents the surface traction on $\partial\Omega_{\text{med}}$ due to aerodynamic loading and VF collision. In this term $\boldsymbol{t}$ represents the surface traction, which is discussed in further detail in Section 5.2.3.

5.2.2 Swelling generalized constitutive equation

Following the approach laid out in Gou and Pence [29], Tsai et al. [116], and Pence and Tsai [151], the constitutive equation employed herein is based on a generalized form for a hyperelastic material. Briefly, the generalized form for swelling of a hyperelastic material with strain energy function $w(\boldsymbol{F})$, is given by $\bar{w}(\boldsymbol{F}, v) = m(v)w(v^{-1/3}\boldsymbol{F})$, where $\bar{w}$ is the swelling-generalized strain energy, and m is a monotonic scalar function satisfying $m(1) = 1$ [116, Equation 3]. In the modified strain energy, $\bar{m}(v) = m/v$ controls the change in stiffness of the swollen material (see Appendix B.1), where its slope governs whether the material stiffness increases or decreases with swelling; if, for example, $\bar{m}' = d\bar{m}/dv < 0$, modulus softening of the swollen material occurs [151, 153]. For a Saint Venant-Kirchhoff material, this results in

$$\begin{aligned} \boldsymbol{S} &= (\bar{m}'(v-1)+1)\, v^{1/3}\left(\frac{E\nu}{(1+\nu)(1-2\nu)}(\mathrm{Tr}\bar{\boldsymbol{E}})\boldsymbol{I} + \frac{E}{1+\nu}\bar{\boldsymbol{E}}\right), \\ \bar{\boldsymbol{E}} &= \frac{1}{2}(\bar{\boldsymbol{F}}^{\intercal}\bar{\boldsymbol{F}} - \boldsymbol{I}) = v^{-2/3}\boldsymbol{E} + \frac{1}{2}(v^{-2/3}-1)\boldsymbol{I}, \end{aligned} \tag{5.3}$$

where E and ν are Young's modulus and Poisson's ratio, respectively. The term $(\bar{m}'(v-1)+1)$ represents the linearized effect of $\bar{m}(v)$ about $v = 1$. The swelling-modified Green strain

tensor, $\bar{\boldsymbol{E}}$, contains an additional strain term $1/2(v^{-2/3}-1)\boldsymbol{I}$ that creates a hydrostatic pressure that results in the swelling (see Appendix B.1).

5.2.3 Fluid and contact models

The surface traction $\boldsymbol{t}$ results from fluid pressures based on the Bernoulli equation and contact [1]. Contact was modeled by a penalty method [60] and the collision pressure is given by

$$p_{\text{con}} = k_{\text{con}} \left(\frac{\max\{g(\boldsymbol{X}), 0\}}{2} \right)^3, \tag{5.4}$$

$$g(\boldsymbol{X}) = Y - Y_{\text{con}}, \tag{5.5}$$

where k_{con} is the contact spring stiffness and g is the contact gap. Note that the term $\max\{g(\boldsymbol{X}), 0\}$ ensures that the contact gap is positive when the VFs are contacting and 0 otherwise. A cubic contact spring is employed to ensure continuity of first and second derivatives of p_{con} at contact.

The Bernoulli equation is given by

$$\begin{aligned}
p(s_i) &= \begin{cases} p_{\text{sub}} + \frac{\rho_{\text{air}}}{2} q^2 \left(\frac{1}{a_{\text{sub}}^2} - \frac{1}{a(s_i)^2} \right) & s < s_{\text{sep}} \\ p_{\text{sep}} & s \geq s_{\text{sep}} \end{cases} \\
q^2 &= \frac{2}{\rho_{\text{air}}} \left(\frac{1}{a_{\text{sep}}^2} - \frac{1}{a_{\text{sub}}^2} \right)^{-1} (p_{\text{sub}} - p_{\text{sep}}) \\
a_{\text{sep}} &= r_{\text{sep}} a_{\text{min}} \\
a_{\text{min}} &= \min_{s_i} a(s_i) \\
a(s_i) &= \max\{2(y_i - Y_{\text{con}}), a_{\text{lb}}\},
\end{aligned} \tag{5.6}$$

where p is pressure, q is flow rate, ρ_{air} is the air density, r_{sep} is the separation area ratio, and a is the cross-sectional area of the glottis (see Figure 5.1). Subscripts 'sep' and 'sub' denote quantities at the separation point and subglottal region, respectively. Areas a_{min} and a_{lb} represent the minimum glottal area and a lower bound on the glottal area function. Specifically, a_{lb} is used to define a "safe" area [72], which is employed in practice to prevent negative areas that can occur from the penalty contact method. As a result, instead of $a(s)$ in Equation (5.6), the safe area

$$a_{\text{safe}}(s) = \begin{cases} a(s) & a(s) > a_{\text{lb}} \\ a_{\text{lb}} & a(s) \leq a_{\text{lb}} \end{cases}, \tag{5.7}$$

is used.

The final surface traction term is then due to both contact and fluid pressures and is given by

$$\boldsymbol{t} = -p \det \boldsymbol{F} \boldsymbol{F}^{-\intercal} \boldsymbol{n} - p_{\text{con}} \boldsymbol{n}_{\text{con}}, \tag{5.8}$$

where $\boldsymbol{n}_{\text{con}}$ is the contact normal. Due to left-right symmetry of the VFs the contact normal is constant and given by $\boldsymbol{n}_{\text{con}} = (0, 1)$.

5.2.4 Numerical solution

To integrate Equation (5.1) in time, we used the Newmark-beta method [126] to approximate $\boldsymbol{v}, \boldsymbol{a}$ at time step $n+1$ using

$$\boldsymbol{v}^{n+1} = \frac{\gamma}{\beta \Delta t}(\boldsymbol{u}^{n+1} - \boldsymbol{u}^n) - \left(\frac{\gamma}{\beta} - 1\right) \boldsymbol{v}^n - \Delta t \boldsymbol{a}^n \left(\frac{\gamma}{2\beta} - 1\right) \tag{5.9}$$

$$\boldsymbol{a}^{n+1} = \frac{1}{\beta \Delta t^2}(\boldsymbol{u}^{n+1} - \boldsymbol{u}^n - \Delta t \boldsymbol{v}^n) - \left(\frac{1}{2\beta} - 1\right) \boldsymbol{a}^n \tag{5.10}$$

where superscripts n denote time indices (for example, $\boldsymbol{a}^n = \boldsymbol{a}(\boldsymbol{X}, t^n)$), $\gamma = 1/2$ and $\beta = 1/4$ were chosen for stability, and $\Delta t = 1.25 \times 10^{-5}\,\text{s}$. The choice of Δt and mesh size were based on an independence study described in Appendix B.2. Substituting Equations (5.9) and (5.10) into Equation (5.1) yields a set of recursive relations for the state $\boldsymbol{u}^{n+1}, \boldsymbol{v}^{n+1}, \boldsymbol{a}^{n+1}$ from known conditions at n. The initial state $n = 0$ is set as the static equilibrium state from Equation (5.1) without external loads (no Bernoulli pressure) but with swelling. External loads are applied for all remaining time steps. The system of equations were solved using the FEniCS library [121, 122].

A parametric study over varying swelling values $v = 1.0, 1.05, \ldots, 1.25, 1.3$ and $\bar{m}' = 0.0, -0.4, -0.8, -1.2, -1.6$ was performed. The range of swelling parameter, v, was chosen based on an extreme level of systemic dehydration for children of 10 % [100, 154]; since local hydration changes are likely larger than systemic levels, a maximum swelling level of 30 % was employed. Swelling was restricted to the cover layer based upon clinical observations which found fluid retention primarily occurred in the superficial lamina propria [30]. Swelling-induced stiffness change, $\bar{m}'$, was chosen based on the study by Yang et al. [109] where they measured force-displacement curves as a function of dehydration. Equation (5.3) implies a 1D modulus for a uniaxial stress test of $k(v) = (\bar{m}'(v-1)+1)E$

so that $k(v)/k(1) = \bar{m}'(v-1)+1$, where $k(v)$ denotes the 1D modulus for swelling level v. Rearranging yields

$$\bar{m}' \approx \left(\frac{k(v)}{k(1)} - 1\right)/(v-1). \tag{5.11}$$

Using 1D modulus values from Yang et al. [109, Tables 2 and 3] we computed $\bar{m}'$ according to different values of $k(v)$ formed from the average of reported loading/unloading modulus values. Dehydration levels were converted to swelling levels assuming an initial water content by volume of 80 %. Over the varying dehydration/swelling levels, we found swelling-induced stiffness change varied from $\bar{m}' \approx -0.4$ to -1.6 (with more negative values at higher dehydration), so values from 0.0 to -1.6 centered around a nominal value of -0.8 were chosen.

All remaining model parameters were fixed and chosen based on past studies and experimental values, as summarized in Table 5.1. Elastic moduli were chosen based on values used in Chhetri et al. [19], Alipour-Haghighi et al. [66], and Miri [155] and Poisson's ratio ν was chosen to model near incompressibility while avoiding numerical instability due to volumetric locking [65, Section 4.4.3]. Epithelium properties were chosen based on previous experimental studies [130, 142]. The contact spring value was chosen to balance minimizing the contact overlap while preventing ill-conditioning of the stiffness matrix [60]. Subglottal and separation pressures were chosen based on physiological ranges during speech [156], and $r_{\text{sep}} = 1.2$ was chosen based on usage in past studies [71, 131].

5.3 Results

In this section, we present results for static parameters (volume and VF geometry changes induced by swelling), acoustic and kinematic outputs (fundamental frequency, SPL, and glottal width amplitude), and measures of VF damage (von Mises stress, viscous dissipation rate, and collision pressure) for varying levels of swelling and swelling-induced stiffness change. We also present results showing the impact of separate swelling-induced effects, specifically, swelling-induced mass, stiffness, and prephonatory gap changes, on the measures of VF damage.

5.3.1 Static parameters

We first consider the influence of swelling on the shape and mass of the VF without external fluid loading (expansion under swelling only). Generalized swelling throughout the cover

Table 5.1: Summary of fixed model parameter values

Parameter	Value
ρ_0, ρ_v	$1\,\mathrm{g/cm^3}$
E_{cover}	$2.5\,\mathrm{kPa}$
E_{body}	$5.0\,\mathrm{kPa}$
E_{epi}	$50\,\mathrm{kPa}$
ν, ν_{epi}	0.4
η	5 poise
d_{epi}	$50\,\mu\mathrm{m}$
Y_{mid}	$0.53\,\mathrm{cm}$ (see Figure 5.1)
Y_{con}	$0.525\,\mathrm{cm}$ (see Figure 5.1)
k_{con}	$1 \times 10^{15}\,\mathrm{Pa/cm^3}$
p_{sub}	$300\,\mathrm{Pa}$
p_{sep}	$0\,\mathrm{Pa}$
r_{sep}	1.2
ρ_{air}	$1.2 \times 10^{-3}\,\mathrm{g/cm^3}$
a_{lb}	$2(Y_{\mathrm{mid}} - Y_{\mathrm{con}})$

was considered to represent phonotraumatic damage distributed throughout the cover after normal voice usage as seen in experimental studies [30]. Figure 5.2 compares the nominal VF geometry with that of a VF with 30% swelling in the cover layer ($v = 1.30$) and swelling-induced relaxation ($\bar{m}' = -0.8$). Swelling leads to an outwards expansion of the medial surface due to the increase in volume of the cover layer. The remainder of the cover layer also experiences swelling, though to a lesser degree due to the fixed constraint at the intersection with $\partial\Omega_{\mathrm{dir}}$. The body layer remains nearly fixed when swelling occurs except for a slight expansion adjacent to the medial surface that arises because of the expansion of the cover.

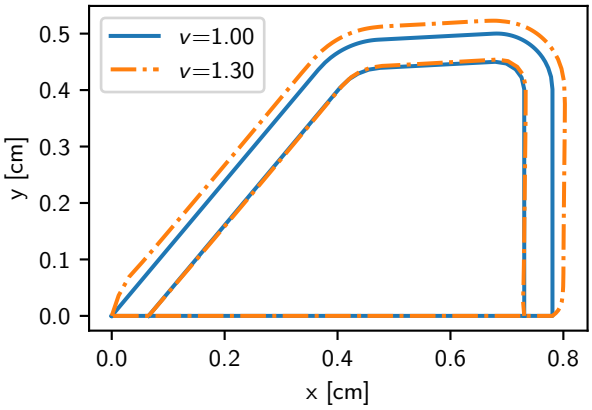

Figure 5.2: Vocal fold geometry for the swollen ($v = 1.3$, dash-dotted lines) and original ($v = 1.0$, solid lines) states for intermediate swelling-induced softening ($\bar{m}' = -0.8$). Displacements due to swelling are exaggerated by two times for clarity

The increase in VF volume with swelling is shown quantitatively in Figure 5.3. The actual volume increase is smaller than the prescribed swelling (close to 20 % for 30 % swelling) due to the action of external forces on the cover layer and the slight compressibility of the cover. The corresponding mass increase is linearly related to the prescribed swelling based on the linear relationship given in Equation (5.2).

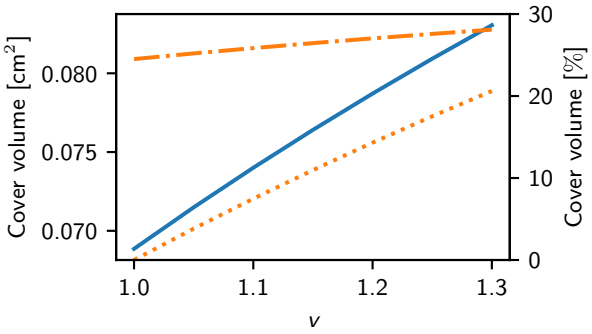

Figure 5.3: Vocal fold cover volume as a function of swelling level, v, for intermediate swelling-induced softening ($\bar{m}' = -0.8$). The left abscissa shows the absolute cover volume (solid line). The right abscissa shows the change in cover volume relative to the total vocal fold volume (dotted line) and the change relative to the initial cover volume (dash-dotted line)

5.3.2 Acoustic and kinematic outputs

Figure 5.4 presents the effect of swelling on kinematic and acoustic outputs. To compute the effect of swelling on fundamental frequency (F_o) we detect peaks of the glottal width waveform ($a_{\min}(t)$) and measure the average period between peaks. To compute SPL we use the flow rate ($q(t)$ from Equation (5.6)) and the piston-in-baffle approximation [50, Section 7.4] at 1 m; this model gives the radiated pressure from an idealized piston sound source. The drop in frequency is about 10 Hz while the reduction in SPL is about 0.5 dB over the range $v = 1.0$ to 1.3. A small increase in SPL is present for small amounts of swelling despite consistently decreasing amplitudes of motion (Figure 5.4) likely due to slight changes in the frequency content of harmonics. Both SPL and F_o also vary with swelling-induced stiffness change ($\bar{m}'$). Greater swelling-induced softening corresponds to larger F_o and SPL decreases for the same level of swelling.

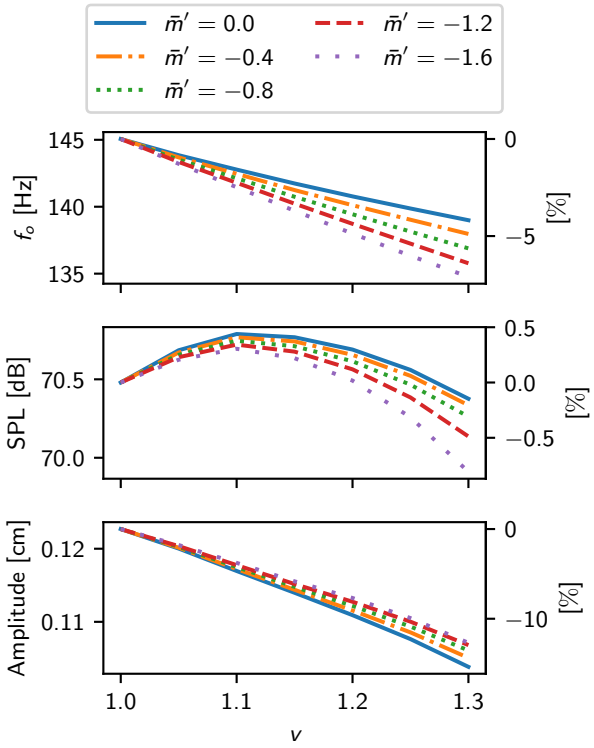

Figure 5.4: Fundamental frequency (F_o), SPL at 1 m, and glottal width waveform amplitude as a function of swelling level (v) and swelling-induced stiffness change ($\bar{m}'$). The right abscissa shows the percent change from the initial value

5.3.3 Vocal fold damage measures

We consider three candidate metrics to assess potential VF damage (phonotrauma), namely von Mises stress, viscous dissipation, and collision pressure, defined as follows. The von Mises stress is given by $\sigma_{\text{vm}} = \sqrt{3/2\boldsymbol{\sigma}_{\text{dev}} : \boldsymbol{\sigma}_{\text{dev}}}$, where $\boldsymbol{\sigma}_{\text{dev}} = \boldsymbol{\sigma} - 1/3(\text{Tr}\boldsymbol{\sigma})\boldsymbol{I}$ is the deviatoric part of the Cauchy stress. Spatial fields of viscous dissipation are defined by $w_{\text{visc}} = \eta\dot{\boldsymbol{\epsilon}} : \dot{\boldsymbol{\epsilon}}$ and spatial fields of collision pressure, p_{con}, are given in Equation (5.4).

To quantitatively compare these spatially and temporally varying variables, we compute the spatial and temporal averages as follows. For a function $f(\boldsymbol{X}, t)$ (representing von Mises stress or viscous dissipation), the spatio-temporal average and temporal average, are

denoted by $\hat{f}$ and $\tilde{f}$, respectively, are defined as

$$\hat{f} = \underset{\boldsymbol{X},t}{\text{avg}}\, f(\boldsymbol{X},t) = \frac{\int_{0.25}^{0.5}\int_{\Omega_{\text{cover}}} f(\boldsymbol{X},t)\, d\boldsymbol{X}\, dt}{\int_{0.25}^{0.5}\int_{\Omega_{\text{cover}}} d\boldsymbol{X}\, dt}, \tag{5.12}$$

$$\tilde{f} = \underset{t}{\text{avg}}\, f(\boldsymbol{X},t) = \frac{\int_{0.25}^{0.5} f(\boldsymbol{X},t)\, dt}{\int_{0.25}^{0.5} dt}, \tag{5.13}$$

where the time integration limits of $(0.25, 0.5)$ represent the last half of the time series.

In the case of contact quantities, we compute similar averages but only count instances where contact occurs. These averages are given by

$$\hat{f} = \underset{s,t}{\text{avg}}\, f(s,t) = \frac{\int_{0.25}^{0.5}\int_{\partial\Omega_{\text{med}}} H(g(s,t))f(s,t)\, ds dt}{\int_{0.25}^{0.5}\int_{\partial\Omega_{\text{med}}} H(g(s,t))\, ds dt}, \tag{5.14}$$

$$\tilde{f} = \underset{t}{\text{avg}}\, f(s,t) = \frac{\int_{0.25}^{0.5} H(g(s,t))f(s,t)\, dt}{\int_{0.25}^{0.5} H(g(s,t))\, dt}, \tag{5.15}$$

where H is the Heaviside step function and $g(s,t)$ is the contact gap from Equation (5.4); note $H(g(s,t))$ is 1 when contact occurs and is 0 otherwise.

Figure 5.5 shows time-averaged von Mises stress fields ($\tilde{\sigma}_{\text{vm}}$) for the no-swelling condition (first column) and as differences relative to the no-swelling condition as swelling increases (subsequent columns). In the inferior portion of the cover layer, increasing swelling causes a slight decrease in the von Mises stress (for example $v = 1.10, \bar{m}' = -0.8$) although this decrease is less severe at higher swelling levels. In the medial and superior portions of the cover layer, increasing swelling consistently increases the von Mises stress. Within the body increasing swelling causes minimal changes. Greater swelling-induced softening (negative $\bar{m}'$) tends to mitigate increases in von Mises stress at higher levels of swelling (see, for example, $v = 1.30$ for the different $\bar{m}'$ values).

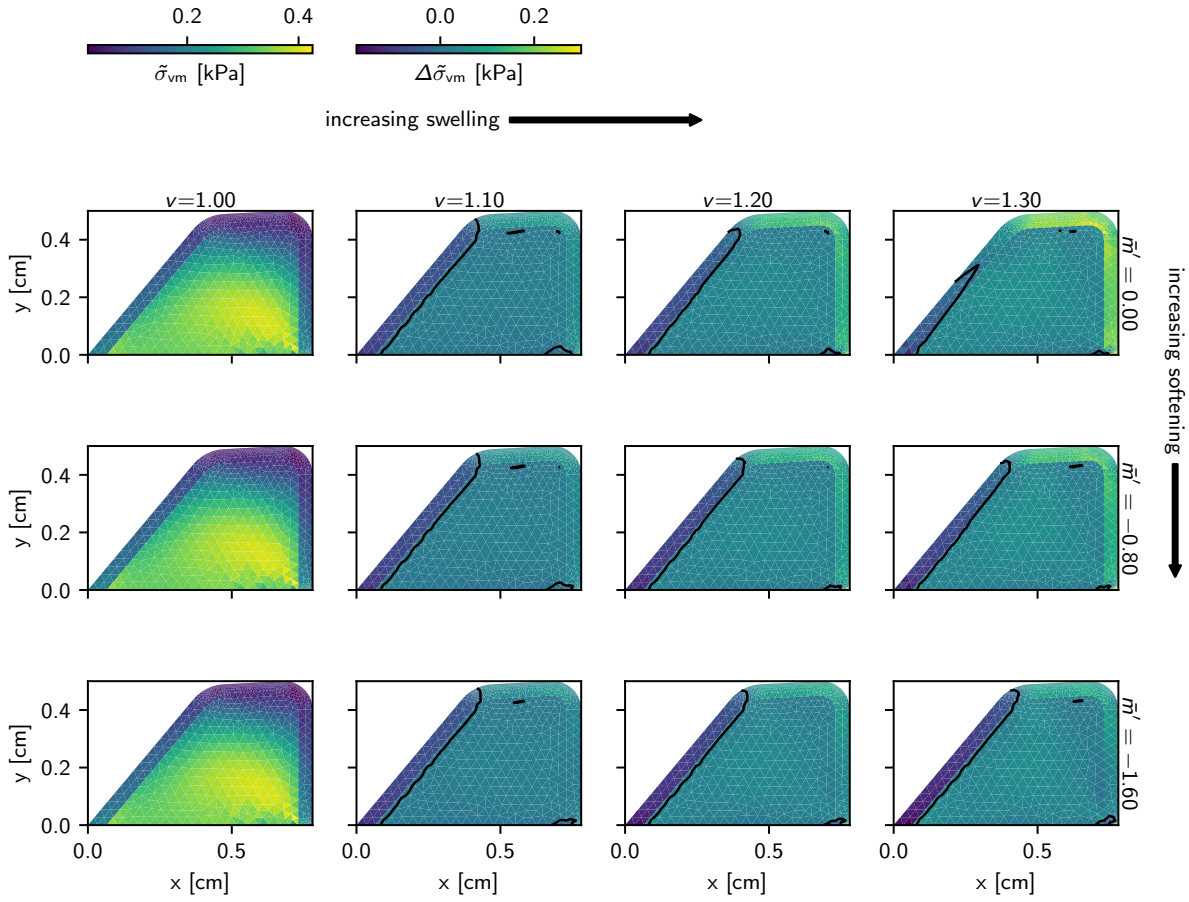

Figure 5.5: Time averaged (over the last 0.25 s) von Mises stress fields ($\tilde{\sigma}_{\text{vm}}$) as a function of swelling level (v) and swelling-induced stiffness change ($\bar{m}'$). The first column shows the absolute von Mises stress while the remaining columns show changes in von Mises stress relative to the no-swelling condition (first column $v = 1$). Regions with $\Delta\tilde{\sigma}_{\text{vm}} = 0$ are indicated by a solid dark contour for clarity

Figure 5.6 summarizes the spatio-temporally averaged trends of von Mises stress ($\hat{\sigma}_{\text{vm}}$). Mean von Mises stress initially drops with increasing swelling (v) due to the decrease in von Mises stress in the inferior part of the cover. This is followed by a more substantial rise with further increases in swelling due to the effects of increasing von Mises stress in the superior and medial parts of the cover. As seen in Figure 5.5, greater swelling-induced softening tends to mitigate the rise in von Mises stress induced by swelling; for the greatest swelling-induced softening ($\bar{m}' = -1.6$), this effect is strong enough to slightly decrease

von Mises stress for all swelling conditions.

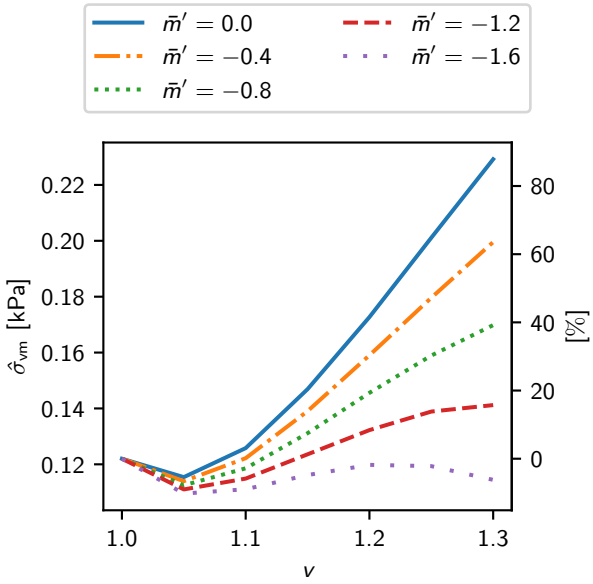

Figure 5.6: Spatio-temporally averaged von Mises stress in the cover ($\hat{\sigma}_{\mathrm{vm}}$) as a function of swelling level (v) and swelling-induced stiffness change ($\bar{m}'$). The right abscissa shows the percent change from the initial value

Figure 5.7 presents time-averaged viscous dissipation fields ($\tilde{w}_{\mathrm{visc}}$) for the no-swelling condition (first column) and as differences compared to the no-swelling condition (subsequent columns). Greater degrees of swelling increases viscous dissipation in the cover, which tends to be concentrated within the medial region of the cover where contact occurs. Greater swelling-induced softening (negative $\bar{m}'$) also results in increased viscous dissipation for the same level of swelling.

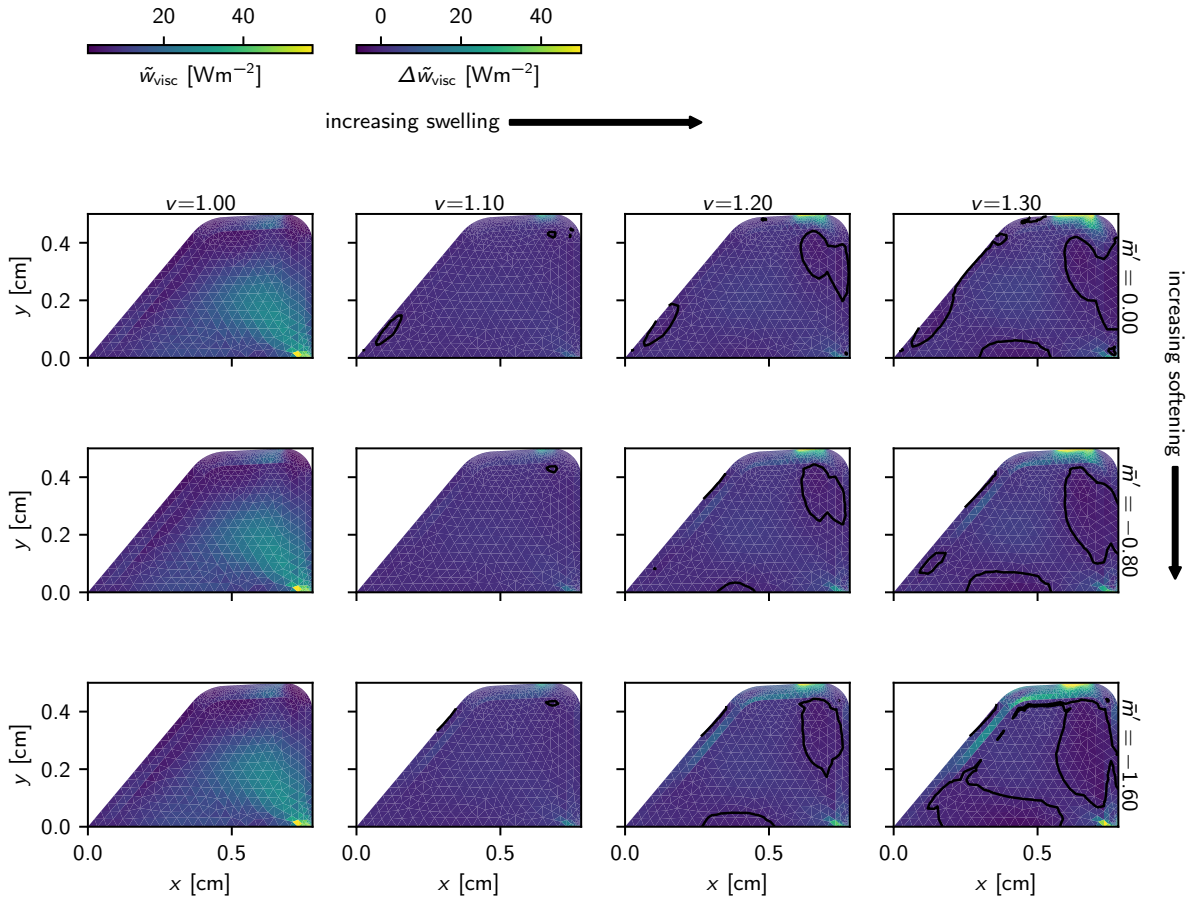

Figure 5.7: Time averaged viscous dissipation rate fields ($\tilde{w}_{\text{visc}}$) as a function of swelling level (v) and swelling-induced stiffness change ($\bar{m}'$). The first column shows absolute values of viscous dissipation rate; subsequent columns to the right show changes relative to the first column. Solid line contours indicate zero viscous dissipation change for clarity

Analogous to Figure 5.6, Figure 5.8 shows the spatio-temporally averaged viscous dissipation rate in the cover ($\hat{w}_{\text{visc}}$). Clearly, viscous dissipation is affected by both swelling magnitude (v) and swelling-induced stiffness change ($\bar{m}'$). Greater swelling and/or swelling-induced softening both result in increased viscous dissipation.

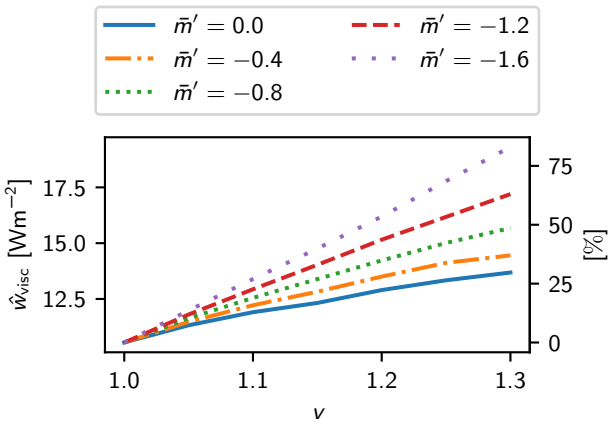

Figure 5.8: Spatio-temporally averaged viscous dissipation rate in the cover ($\hat{w}_{\mathrm{visc}}$) as a function of swelling level (v) and swelling-induced stiffness change ($\bar{m}'$). The right abscissa shows the percent change from the initial value

Figure 5.9 shows the time averaged collision pressure during VF collision ($\tilde{p}_{\mathrm{c}}$). As swelling increases, so does collision pressure and contact area. Greater swelling-induced softening (negative $\bar{m}'$) reduces the magnitude of collision pressure and slightly reduces the contact area.

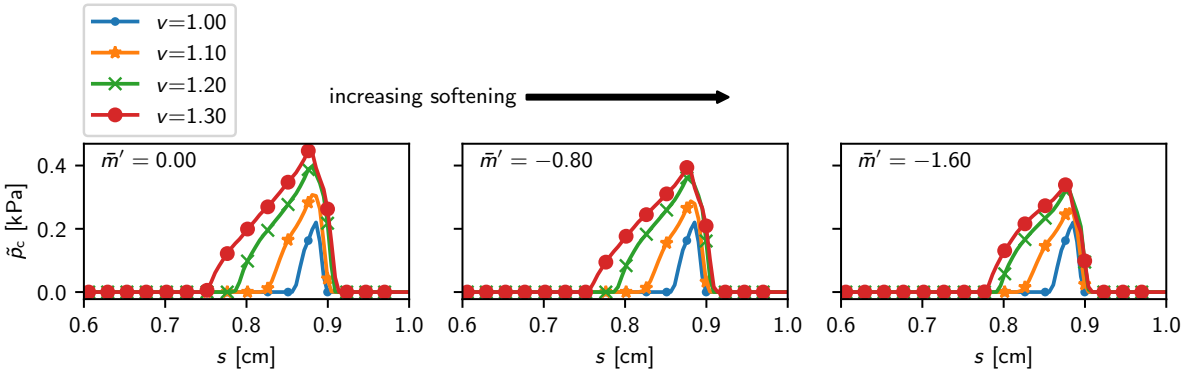

Figure 5.9: Time averaged (over the contacting duration) collision pressure distributions ($\tilde{p}_c$) as a function of swelling level (v) and swelling-induced stiffness change ($\bar{m}'$)

Figure 5.10 illustrates the temporal and spatial statistics of contact quantities over the contacting duration and areas. For the spatio-temporally averaged collision pressure ($\hat{p}_c$), Figure 5.10 shows that increasing swelling (v) generally increases collision pressure (both average and maximum), except for a small dip in spatio-temporally averaged contact pressure for slight swelling ($v = 1.1$), which is exacerbated with increasing swelling-induced softening ($\bar{m}'$). In general, greater swelling-induced softening ($\bar{m}'$) reduces the increase in collision pressure with swelling. Contact area ($\tilde{A}_c$) is similarly affected with more swelling leading to larger contact areas. Swelling-induced stiffness change has a small mediating effect where greater softening results in a slightly smaller contact areas.

5.3.4 Isolating the impact of swelling-induced effects on damage measures

In this section we aim to isolate the influence of various swelling-induced effects on VF damage measures. Specifically, we decompose swelling into four constituent effects; namely, swelling-induced changes in:

1. mass, arising from Equation (5.2),

2. stiffness, arising from the term $(\bar{m}'(v-1)+1)$ in Equation (5.3)

3. VF geometry from the hydrostatic pressure generated by the swelling-modified Green strain ($\bar{\boldsymbol{E}}$) in Equation (5.3), and

4. prephonatory gap (the minimum distance between the symmetry plane and VF surface in Figure 5.1); the gap change is related to the static deformation from swelling and a fixed symmetry plane.

To explore the isolated effects of swelling-induced changes in mass, stiffness, and prephonatory gap, we conducted simulations wherein the chosen parameters was held constant. For mass, this was accomplished by leaving the density constant; for stiffness this coincides with setting $\bar{m}' = 0$; for the gap change this involves shifting the symmetry plane (Y_{mid} in Table 5.1) to ensure the prephonatory gap remains fixed. To examine the effect of VF geometry change, we removed the other effects (mass, stiffness, and prephonatory gap change) and observed how the damage quantity changed with increasing swelling (which induced a VF geometry change). This was made possible because when these three effects are removed, only the swelling-induced VF geometry change effect remains. By then comparing against results with all influences included, the impact of the selected component could be assessed.

Figure 5.11 shows that each damage measure is affected by different swelling-induced changes. Spatio-temporally averaged von Mises stress ($\hat{\sigma}_{\text{vm}}$) is primarily affected by swelling-induced VF geometry changes and stiffness changes ($\bar{m}'$), as seen in Figure 5.11 since the 'no stiffness change' trend differs significantly from the 'all swelling effects' trend. When only the VF geometry change effect is present ('no stiffness, mass, or gap change') von Mises stress increases with swelling (v), thus showing the effect of swelling-induced VF geometry change on von Mises stress. Swelling-induced mass, stiffness, and prephonatory gap all tend to increase spatio-temporally averaged viscous dissipation ($\hat{w}_{\text{visc}}$). Removing these three effects ('no stiffness, mass, or gap change') results in little variation of viscous dissipation with swelling, indicating that swelling-induced VF geometry changes have little impact. Swelling-induced softening (the 'no stiffness change' trend is above the 'all swelling effects' trend) tends to decrease spatio-temporally averaged collision pressure ($\hat{p}_{\text{c}}$), whereas swelling-induced mass and gap changes tend to increase collision pressure (the 'no mass change' and 'no gap change' trends are below the 'all swelling effects' trends). When these three effects are removed collision pressures vary only slightly with swelling, again indicating that swelling-induced VF geometry change has little effect.

5.4 Discussion

As expected, swelling clearly alters the shape and mass of the VFs. Mass change follows the linear relationship prescribed in Equation (5.2). For the volume change, the medial surface predictably bulges outwards (Figure 5.2); furthermore, because the body layer does not swell, the expansion of the cover layer also slightly expands the body by pulling it outwards. The slight expansion of the body layer is a result of the small but non-zero compressibility of the system.

As seen in Figure 5.4, fundamental frequency (F_o) decreases with increasing swelling (v) and swelling-induced softening ($\bar{m}'$). Considering a spring-mass-damper analogy for the VF, swelling increases mass and decreases stiffness, both of which reduce frequency. Swelling-induced softening results in a larger stiffness reduction for the same degree of swelling, leading to a drop in fundamental frequency. Swelling has a small effect on SPL, where increasing swelling and/or swelling-induced softening tends to reduce SPL. We hypothesize this is due in part to the reduced prephonatory gap with swelling due to the bulging cover. Reduced prephonatory gap is associated with diminished vibration amplitudes (Figure 5.4), leading to smaller flow rate waveform amplitudes and thus SPL. The changes in SPL were on the order of 0.5 dB, however, which is likely insignificant considering variations in SPL for a speaker between utterances have been measured at over 1 dB [157]. The observed changes in SPL and F_o herein are qualitatively similar to changes in these quantities found in a recent study exploring the effect of dehydration-induced stiffness changes [34] (the reverse of swelling-induced softening studied herein) of 8.6 Hz and −0.4 dB, respectively, at 10 % systemic dehydration.

5.4.1 Damage measures

Swelling has differing effects on the various damage measures explored herein, with some showing propitious effects of swelling and others exhibiting detrimental trends, depending on the degree of swelling. As swelling increases, von Mises stress in the cover ($\tilde{\sigma}_{vm}$) is affected differently depending on the region. In the medial and superior parts of the cover, increased swelling consistently increased von Mises stress (Figure 5.5), while in the inferior portion of the cover it experienced a slight decrease. The spatio-temporal average of von Mises stress over the cover ($\hat{\sigma}_{vm}$ shown in Figure 5.6) exhibits a slight decrease with low degrees of swelling followed by a rapid rise as swelling increases further. Similarly, average contact pressure ($\hat{p}_c$ seen in Figure 5.10), though increasing initially with swelling, exhibits a plateau over a range of modest swelling. That is modest swelling may be

beneficial, at least in terms of these particular damage measures, which is aligned with the clinical impression of the protective benefits of vocal warm up exercises in mitigating vocal fatigue and potentially vocal injury [158]. In contrast, spatio-temporally averaged viscous dissipation ($\hat{w}_{\text{visc}}$) and maximum collision pressure (Figures 5.8 and 5.10, respectively) both exhibited detrimental effects with swelling.

The selected damage measures are primarily affected by different aspects of swelling (see Figure 5.11) likely due to differing physical mechanisms that drive them. The von Mises stress, for example, is primarily affected by VF geometry changes and swelling-induced stiffness change (Figure 5.11) likely due to the mechanism of cover deformation induced by swelling (v). This is supported by differences in the von Mises stress distribution between the inferior part of the cover and the remainder. In the inferior portion of the cover, swelling acts to expand the cover while air pressure in the glottis tends to compress it, thus leading to less distortion and lower von Mises stress. Over the medial and superior surfaces, however, fluid pressures are negligible due to flow separation so the swelling-induced VF geometry change leads to distortions that purely increase von Mises stress. Under greater swelling-induced softening, distortions induced by VF geometry change will likewise directly result in smaller stresses.

Swelling-induced mass, stiffness, and prephonatory gap changes were all found to increase viscous dissipation (Figure 5.11) due to its dependence on tissue strain rates. Lowering stiffness, for example, tends to increase tissue deformations which would increase strain rates and thus increase viscous dissipation. Increasing mass tends to increase VF momentum which would also lead to higher viscous dissipation, particularly during contact, when the additional momentum is dissipated. Similarly, as swelling reduces the prephonatory gap, the VFs tend to collide with greater momentum, as evidenced by collision pressure [159, 160], which would lead to higher internal strain rate and greater viscous dissipation.

Effects of swelling-induced changes on collision pressure ($\hat{p}_{\text{c}}$) are explained by the momentum of the VFs at contact. The effect of swelling-induced softening on lowering collision pressure arises because the softer cover layer increases the time and area over which contact force is distributed. Swelling-induced mass variation tends to increase collision pressure (Figure 5.11) likely due to the increase in momentum of the VFs, which was found to increase with increasing swelling. Similarly, swelling-induced prephonatory gap tends to cause increased collision pressure, as seen for smaller prephonatory gaps in past studies [159, 160], likely due to an increase in the pre-collision momentum.

All damage measures appear concentrated in the medial and superior portions of the cover (Figures 5.5, 5.7, and 5.9). If von Mises stress ($\tilde{\sigma}_{\text{vm}}$) plays a dominant role in damage

then swelling would be broadly distributed throughout the medial and superior portions of the cover (Figure 5.5). In contrast, if collision pressure ($\tilde{p}_c$) and viscous dissipation ($\tilde{w}_{visc}$) drive damage, then swelling would likely concentrate at local regions on the medial surface, (Figures 5.9 and 5.7).

Our results also suggest how swelling could play a role in initiating a vicious cycle that leads to PVH. The first aspect of the vicious cycle is a hyperfunctional response induced by changes in acoustic outputs from swelling. Our study shows that moderate amounts of swelling (30 %) induce relatively small changes in SPL (about 0.5 dB) and moderate changes in fundamental frequency (about 10 Hz) which suggests that hyperfunctional adjustments for voice changes induced by swelling would likely compensate for fundamental frequency rather than loudness. Increases in fundamental frequency could be facilitated by compensatory hyperfunctional increases in muscle tension and subglottal pressure. Higher subglottal pressures would likely then trigger further swelling due to the damage induced by swelling as discussed previously. This could potentially lead to a vicious cycle and the development of PVH. We note, that the simulations presented herein were performed at very low subglottal pressures, which was necessary to ensure self-sustained oscillations over the entire range of swelling parameters considered. We suspect that the impact of swelling on SPL and F_o would be more significant at higher subglottal pressures, but confirming this will require significant modifications to the methodology that are beyond the scope of this preliminary effort.

5.4.2 Study limitations

There are several important limitations in our study. First, three-dimensional (3D) effects are inherently omitted by virtue of the 2D model. Given the aspect ratio of fully adducted VFs, we expect that 3D simulation findings would be similar to the present results in a mid-coronal plane. That said, protuberances in the mid-membranous region evident in structural pathologies and their influence on VF dynamics cannot be accurately explored with a 2D model. Similarly, swelling localized to this region would require a full 3D simulation.

The third term in the first integral of Equation 1 represents viscous effects through a simple Kelvin-Voigt model, which is assumed herein to be unaffected by swelling. Hydration of the VFs is known to affect VF viscosity, with experiments finding that dehydration increases viscosity [108]. This suggests that swelling, which increases water content, should lower viscosity. We expect that incorporating this effect will not significantly influence our results except for the viscous dissipation rate, since this measure is directly affected by viscous stresses. We hypothesize that modelling this effect will increase the viscous dissipation

with swelling, $\tilde{w}_{\text{visc}}$, since the reduced viscosity will facilitate larger strain rates for the same external forcing. In addition, the Kelvin-Voigt model is a simple viscoelastic model that does not capture some viscoelastic behaviour of VFs, such as shear-thinning [128, Figure 6]. We opted to omit more complicated viscoelastic models and swelling effects on viscosity in order to focus our study on the change in shape and stiffness induced by swelling. More sophisticated viscoelastic models, like biphasic models, are more suited to investigate hydration-induced changes in viscosity and potentially capture viscoelastic phenomena like shear-thinning. Coupling stress-driven fluid flux and swelling is left for future work.

Importantly, the present model does not incorporate physical mechanisms that cause swelling, such as chemical concentration differences leading to osmotic pressure gradients. Our model considers swelling that is purely related to mechanical trauma; however, swelling is mediated and caused by numerous factors, such as presence of disease, changes in lymph drainage, and increases in capillary pressure [105]. While the current approach allows us to prescribe the level of swelling *a priori*, modeling the physical mechanisms that cause swelling is necessary for future studies examining the the progression of phonotrauma. For example, in swelling induced by damage, the swelling profile would likely be concentrated near regions of local damage in contrast to the uniformly distributed swelling considered here. Consideration of physical mechanisms that cause swelling will be the subject of future work.

The subglottal pressure used in our model (300 Pa, Table 5.1) is lower than the typical value of about 1000 Pa used in many computational studies (see, for example, [54, 68, 70]). In our simulations, we observed the hyperelastic material model predicted the VFs would adopt a static "blown apart" configuration at subglottal pressures above about 500 Pa while the VFs would self-oscillate for intermediate pressures above the onset pressure but below this value. While this subglottal pressure is lower than the typical value employed in previous studies, it is within the lower end of the physiological range [156]. Another study employing a different hyperelastic material model (Mooney-Rivlin) for the VFs [117] coupled with a Bernoulli-based glottal flow used a subglottal pressure value of 2000 Pa but also modeled the VFs as three-dimensional and employed a different VF geometry. Extending the current model to three-dimensions along with modifications to VF geometry and constitutive models might allow for similarly high subglottal pressures to be employed while maintaining self-oscillation of the VFs. These higher subglottal pressures could also increase the effects of swelling on SPL and frequency seen here.

Our model does not include acoustic feedback effects (level 2 interactions [51]) which could influence the VF dynamics with swelling. Given that the effects of swelling without acoustics induced relatively small changes, we suspect that acoustic coupling effects would likewise be minor. In special cases where the fundamental frequency is near a formant

frequency, however, the changes in frequency induced by swelling could lead to dramatic changes in behavior due to resonance effects. Such acoustic feedback requires further investigation.

Finally, in the broader context of quantifying phonotrauma, there remains debate as to the most appropriate damage measure, with several having been proposed in the literature, including dissipation dose, contact pressures, and internal stresses [144–146, 160–162], which inspired the viscous dissipation metric employed herein [144, 146]. Furthermore, it remains unclear whether localized damage or more distributed measures are most important and how these translate to swelling. The process leading from mechanical trauma to swelling involves a complex bio-chemical response at the cellular level which ultimately disturbs the normal fluid exchange through tissue [29]. Whether localized or distributed measures of damage are more important then, would require detailed knowledge of how tissue damage affects these cellular mechanisms that control the fluid balance, which is incompletely understood [29]. The measures explored herein were selected to canvas some of the parameters considered in prior literature for quantifying phonotrauma, but we make no claim that these are the best, nor even necessarily the most appropriate, measures to consider. As additional clinically-validated measures are identified the influence of swelling should be reconsidered through their lens.

5.5 Conclusions

In this manuscript we presented a first investigation into the impact of swelling distributed throughout the VF cover layer on VF kinematics and selected damage measures. At modest levels of swelling the impacts were marginal, but grew as the degree of fluid accumulation increased. For example in terms of voice outputs, swelling consistently reduced fundamental frequency and SPL (a swelling value of 30 % induced around a 0.5 dB drop and 10 Hz drop in SPL and frequency, respectively). Such changes in voice outputs would lead to compensatory adjustments that could trigger the development of PVH.

Damage measures (von Mises stress, viscous dissipation, and collision pressure) were affected by swelling in different ways. In the case of von Mises stress, small values of swelling reduced average stresses in the cover due to a protective effect in the inferior portion of the cover while larger values of swelling increased von Mises stress depending on the amount of swelling-induced stiffness change (by about 40 % at swelling of $v = 1.3$ and swelling-induced softening of $\bar{m}' = -0.8$). Viscous dissipation consistently increased with increasing swelling and with greater swelling-induced stiffness change exacerbating the effect (by about 50 % at $v = 1.3$ and $\bar{m}' = -0.8$). Similarly, swelling tended to increase

collision pressure (by about 75 % at $v = 1.3$ and $\bar{m}' = -0.8$) with increasing swelling, whereas greater swelling-induced stiffness change ameliorated the effect.

Swelling was decomposed into constituent effects to examine the factor that most contributed to observed trends in damage measures. Von Mises stress in the VFs was primarily affected by the swelling induced shape and stiffness changes. In the inferior part of the cover, swelling induced volume increases balanced with the compressive effects of the fluid loading resulting in decreases in von Mises stress. In the medial and superior portions of the cover, however, the flow accelerates or separates resulting in little fluid loading and therefore von Mises stress increased under the effect of swelling. In contrast to the von Mises stress, viscous dissipation and collision pressures were affected primarily by swelling-induced mass, stiffness, and prephonatory gap, and not the VF geometry change (Figure 5.11). In the case of swelling-induced stiffness, for example, we hypothesized the reduced stiffness tended to increase the magnitude of deformations which increased viscous dissipation; for collision pressure, the reduced stiffness would tend to distribute contact forces over longer times and areas, thus reducing average collision pressures.

Future work will aim to connect the distribution and magnitude of swelling with measures of damage. This will then be used to model the progressive effects of swelling with repeated voice usage due to the feedback of swelling-induced voice output changes leading to compensatory changes in the VFs that further increase swelling. To capture the important effects of swelling on viscoelastic parameters, coupling of swelling with biphasic models will also be pursued. Incorporating these two mechanisms will allow investigation of the etiology of PVH from phonotrauma.

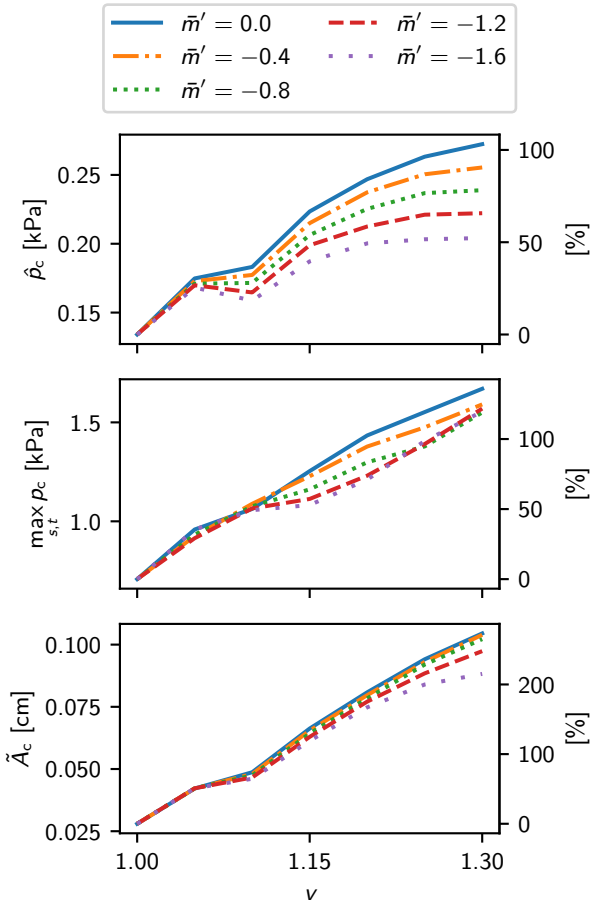

Figure 5.10: Statistics of contact quantities over the contacting duration and area consisting of spatio-temporally averaged collision pressure ($\hat{p}_c$), maximum collision pressure, and time averaged contact area ($\tilde{A}_c$) as a function of swelling level (v) and swelling-induced stiffness change ($\bar{m}'$). In each case, the right abscissa shows the percent change from the initial value

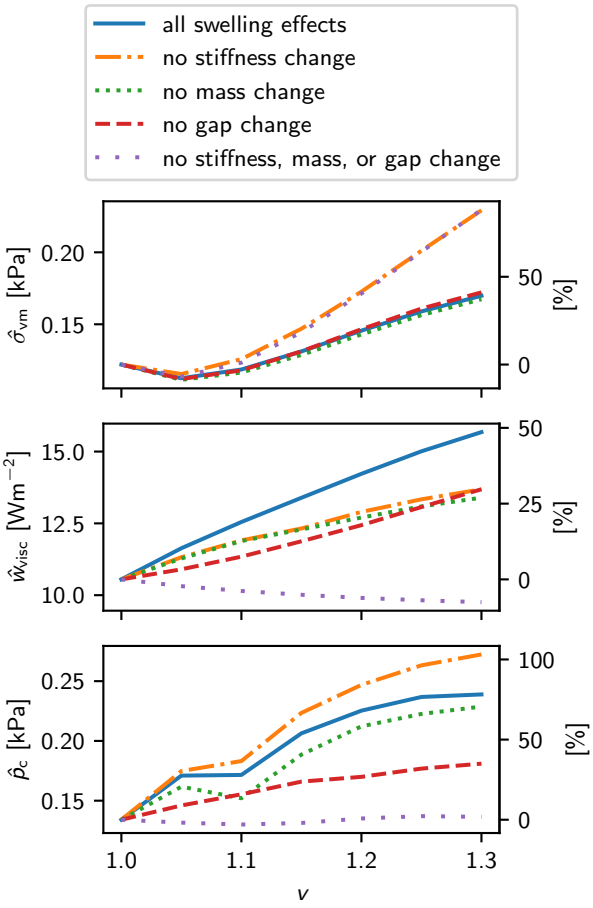

Figure 5.11: Comparison of spatio-temporally averaged von Mises stress ($\hat{\sigma}_{\mathrm{vm}}$), viscous dissipation ($\hat{w}_{\mathrm{visc}}$), and collision pressure ($\hat{p}_{\mathrm{c}}$) trends versus swelling (v) with different swelling-induced effects removed and/or present for the intermediate swelling-induced softening ($\bar{m}' = -0.8$). In the case 'no stiffness, mass, or gap change', only swelling-induced geometry change remains. The right abscissa shows the percent change from the initial value

Chapter 6

Conclusions and recommendations

6.1 Conclusions

The thesis investigated physical mechanisms in the etiology of VH using computational models. Vocal hyperfunction is a disorder wherein excessive or abnormal (hyperfunctional) muscular adjustments occur in speech due to compensation for some underlying issue [9, 10], and it is estimated to occur in 40 % of all voice disorders [8]. Despite VH being a highly prevalent and impactful disorder, its etiology is poorly understood [9, 13]. A wide range of hypothesized etiologies have been proposed ranging from psychological to biomechanical factors [13]. The basic computational model employed consists of a 2D FEM based representation of the VFs with a 1D Bernoulli based representation of the glottal flow. Three studies were conducted where modifications and additions to this core model were made in order to explore different hypothesized physical mechanisms, summarized and reiterated here as (see Chapter 1):

1. Explore the sensitivity of phonation onset pressure to stiffness distributions within the VFs to uncover if particular stiffness distributions have larger impacts on increasing onset pressure and thus risk for developing PVH.

2. Investigate how modelling separate epithelium and LP layers differs from modelling a single cover layer and develop a membrane model of the epithelium to reduce computational cost of modelling the epithelium.

3. Develop a model of VF swelling to investigate if/how swelling induced changes in the VFs can trigger a hyperfunctional response and vicious cycle, and thus if swelling

can trigger the development of PVH.

In Chapter 3 the role of stiffness distributions of the VFs in increasing risk for developing PVH was studied. The computational VF model was treated as a dynamical system in order to compute onset pressure, and to obtain a second-order Taylor model of these quantities with respect to stiffness distributions. The results showed that three stiffness variations are of primary importance in controlling onset pressure: a BC-like variation with smooth gradients in the IS and ML directions, a IS stiffness difference in the interior region of the VFs, and a roughly uniform stiffness increase. The BC-like and IS stiffness distributions had positive quadratic effects on onset pressure, which implies that these stiffness variations have specific values which minimize onset pressure. The uniform stiffness increase, on the other hand, was associated with a linear increase in onset pressure. Because increases in average stiffness are associated with increases in natural frequency, this gives the interpretation that linear increases in onset pressure due to uniform stiffness increases are associated with increases in frequency of speech. Conversely, the BC-like and IS-like stiffnesses have little effect on average stiffness so represent stiffness distributions that vary onset pressure for a given phonation frequency. This suggests that BC-like and IS-like stiffness differences play an important role in minimizing risk for developing PVH. For a given phonation frequency (average stiffness) a critical BC-like and IS-like stiffness distribution is needed to minimize onset pressure which reduces phonatory effort and would minimize risk for developing PVH. This finding improves on previous results which considered simplified stiffness distributions that do not reflect actual stiffness variations in the VFs [19, 23, 24, 163], and previous studies which predicted monotonic effects of BC-like variations [18] (that is, the greater the BC variation the better). This result identifies the two stiffness distributions of greatest importance in governing onset pressure, and hence vocal effort and risk for PVH, which can help focus future research into prevention and treatment of the disorder.

In Chapter 4, effects of the epithelium were modelled as a preliminary step and requirement for the modelling of swelling. Specifically, while VFs have a well-known layered structure that is commonly grouped into body and cover layers, the cover actually consists of a stiff thin epithelium on top of a thicker loose lamina propria. Experimental studies exploring the effects of modelling epithelium and lamina propria layers separately found that the distinct layers behaved differently from a lumped cover, and thus distinct layers would likely play an important role on swelling in the VFs. To model the epithelium and lamina propria separately, a FEM implementation of the epithelium as a membrane was created and added to the basic BC FEM VF model. Testing of the model showed that while modeling a lumped cover results in qualitatively similar glottal area waveforms compared to modelling the epithelium and lamina propria separately, details of internal dynamics

and kinematic measures (for example, IS displacement, internal stresses, and viscous dissipation) were markedly different. This suggests modelling the layers separately rather than together in a lumped cover is important to capture the difference in dynamics and kinematics. This result improves on previous models which incorporated an epithelium by discretizing the thin layer with elements [131] (which increases computational complexity) and also agrees with past experimental studies that found the epithelium has significant impacts on VF motion (such as in reducing IS displacement).

In Chapter 5, the role of swelling in triggering a vicious cycle that leads to PVH was studied. To do this, the epithelium BC FEM model described in Chapter 4, was augmented with a developed model of swelling [29, 116]. This swelling model consists of a modified hyperelastic constitutive equation which causes swelling through a hydrostatic pressure given by a prescribed swelling field. The swelling model captures shape changes induced during swelling as well as changes in stiffness and density of the swollen material. The developed model was used to conduct parametric studies on the effects of swelling on voice outputs (F_o and SPL) and measures of VF damage (von Mises stress, viscous dissipation, contact pressure). Results showed that increasing swelling consistently lead to increased measures of VF damage, moderated by swelling induced softening. In addition, increasing swelling reduces F_o albeit with negligible changes in SPL. These two findings suggest swelling could play a role in triggering the vicious cycle in PVH in the following manner. Initial swelling reduces output frequency which results in compensatory increases in subglottal pressure and muscle tension. Under these compensatory adjustments measures of VF damage tend to increase because forces are higher with increase subglottal pressure, which leads to further swelling. With increased swelling, measures of VF damage also increase so that a positive feedback process may be triggered. This result suggests the physical mechanism through which a vicious cycle in PVH can be triggered (through compensatory adjustments for F_o) and thus could inform future research and clinical treatment of PVH. The result also improves on previous work by introducing a swelling model for VFs which has previously not been considered.

6.2 Recommendations for future work

The onset study considered the effect of changes in elasticity on onset pressure; however there are additional factors that affect onset pressure. The onset study aimed to see what stiffness distributions are most important to maintain a low onset pressure, and thus avoid high phonatory effort that could lead to PVH. While such changes are an important factor in controlling the onset pressure there are other factors, namely, shape of the VF medial

surface and changes in VF posture through muscle activation. Shape changes have largely not been studied, but likely play a role in the dynamics of the VFs and onset pressure. Similarly, muscle activations create active stresses in the VFs [117] which creates pre-stresses and strains and changes the prephonatory shape of the VFs, ultimately affecting the mechanical response and onset pressure. Muscle activation is particularly important because modulation in frequency of the VFs is accomplished with muscle activation [3], not stiffness of the VFs as was considered in this study. A similar study of the effects of muscle activation on onset pressure could illustrate what types of muscle activation have the least phonatory effort (lower onset pressure) for a target frequency, which is more useful physiologically since muscle activation is physiologically controlled, rather than VF stiffness. A potential approach to study this is to develop a model of muscle activation as done in past studies [117] and study the sensitivity of onset pressure with respect to muscle activation rather than stiffness.

The swelling study only considered a parametric study of how swelling changes voice outputs and damage measures to investigate if they can trigger a vicious cycle, but did not model the vicious cycle itself. A next step would be to modelling the vicious cycle directly by modelling the compensatory response and by linking measures of phonotrauma to resulting swelling. Linking measures of phonotrauma to swelling is a particularly important and complicated aspect of this since, physiologically, swelling occurs through a complex biochemical process (Section 2.5). Modelling this will thus involve phsyiological and biochemical factors that could also vary between individuals. Nevertheless, modelling the vicious cycle is important because it would inform details of how the vicious cycle leads to PVH, such as the time required, and resulting severity.

The epithelium membrane model considered a small-deformation assumption which should be extended to a large deformation membrane. For the range of swelling considered, deformations of the membrane were small and so the small strain assumption was likely sufficient; however, large strains in the VFs can occur during loud voicing and notably during VF posturing movements induced by muscle activation. Modelling such scenarios with an epithelium will require a large deformation model. Large deformation thin-shell models are available in many off-the-shelf finite element method software packages, however, such a model does not exist in FEniCS so must be implemented under the constraints of the FEniCS library. Potential formulations that could be used to accomplish this were given in a "intrinsic" formulation [138, 164].

Models used across the different studies relied on a 2D plane-strain representation but 3D effects are likely important in some scenarios. The 2D plane strain representation is a useful simplification due to lower computational cost and is likely reasonably accurate for some scenarios such as for long VFs (AP dimension in the coronal plane) which

would ensure accuracy of the 2D strain assumption. In many situations, however, these assumptions are invalidated and thus necessitate a 3D model. For example, VFs undergo posturing changes through muscle activations which involve changes in shape of the VFs and so involves 3D effects. Similarly VFs have transversely isotropic properties where the properties in the AP direction are different from those in the coronal plane (the plane considered in the simplified 2D representations). When VFs are tensed or loosened, these properties may play a large role in the mechanical response necessitating modelling of 3D effects.

Models used a simplified 1D Bernoulli flow which should be extended to higher fidelity flow models. Past studies have commonly used the 1D Bernoulli flow approximation because of its simplicity, and some studies have shown that 1D Bernoulli type models give qualitatively similar results to those based on the NS equations. However, the 1D Bernoulli flow model cannot capture complex physical phenomena such as flow seperation, and formation of boundary layers in the thin glottal channel (viscous effects become important when the VFs are near closure). These more complicated flow effects can play an important role; for example, flow separation plays a large role in the pressure distribution on the VF surface and so must be specified in an ad-hoc manner for 1D flow models. One promising approach that could balance the fidelity of complicated models and simplicity of 1D models are more recent 1D flow models for collapsible flow channels [72, 74] that attempt to capture 3D flow phenomena using additional terms.

Models also did not include acoustic effects, which can play an important role in certain situations. For example, acoustic effects are theorized to play a large role on VF dynamics when the acoustic tract opening above the glottis is small, or when the frequency of formants is close to the frequency of VF vibration [51]. These voice situations may occur when producing particular vowel sounds and pitches. Future work could employ 1D acoustic models, such as the wave-reflection analog approach, to capture these effects.

Letter of Copyright Permission

Order Date	10-Aug-2023	**Type of Use**	Republish in a thesis/dissertation
Order License ID	1385034-1		
ISSN	0066-4189	**Publisher**	Annual Reviews
		Portion	Chart/graph/table/figure

LICENSED CONTENT

Publication Title	Annual Review of Fluid Mechanics	**Publication Type**	Journal
Article Title	Fluid Dynamics of Human Phonation and Speech	**Start Page**	437
		End Page	467
Date	01/01/1969	**Issue**	1
Language	English	**Volume**	45
Rightsholder	Annual Reviews, Inc.		

REQUEST DETAILS

Portion Type	Chart/graph/table/figure	**Distribution**	Worldwide
Number of Charts / Graphs / Tables / Figures Requested	1	**Translation**	Original language of publication
		Copies for the Disabled?	No
Format (select all that apply)	Electronic	**Minor Editing Privileges?**	Yes
Who Will Republish the Content?	Academic institution	**Incidental Promotional Use?**	No
Duration of Use	Life of current edition	**Currency**	CAD
Lifetime Unit Quantity	Up to 9,999		
Rights Requested	Main product		

NEW WORK DETAILS

Title	Modelling Physical Mechanisms of Nodule Development in Phonotraumatic Vocal Hyperfunction using Computational Vocal Fold Models	**Institution Name**	Univeristy of Waterloo
		Expected Presentation Date	2023-08-31
Instructor Name	Jonathan Deng		

ADDITIONAL DETAILS

Order Reference Number	N/A	**The Requesting Person/Organization to Appear on the License**	Jonathan Deng

REQUESTED CONTENT DETAILS

Title, Description or Numeric Reference of the Portion(s)	Figure 1	**Title of the Article/Chapter the Portion Is From**	Fluid Dynamics of Human Phonation and Speech
Editor of Portion(s)	Mittal, Rajat; Erath, Byron D.; Plesniak, Michael W.	**Author of Portion(s)**	Mittal, Rajat; Erath, Byron D.; Plesniak, Michael W.
Volume / Edition	45	**Issue, if Republishing an Article From a Serial**	1
Page or Page Range of Portion	437-467	**Publication Date of Portion**	2013-01-03

Marketplace Permissions General Terms and Conditions

The following terms and conditions ("General Terms"), together with any applicable Publisher Terms and Conditions, govern User's use of Works pursuant to the Licenses granted by Copyright Clearance Center, Inc. ("CCC") on behalf of the applicable Rightsholders of such Works through CCC's applicable Marketplace transactional licensing services (each, a "Service").

1) **Definitions.** For purposes of these General Terms, the following definitions apply:

"License" is the licensed use the User obtains via the Marketplace platform in a particular licensing transaction, as set forth in the Order Confirmation.

"Order Confirmation" is the confirmation CCC provides to the User at the conclusion of each Marketplace transaction. "Order Confirmation Terms" are additional terms set forth on specific Order Confirmations not set forth in the General Terms that can include terms applicable to a particular CCC transactional licensing service and/or any Rightsholder-specific terms.

"Rightsholder(s)" are the holders of copyright rights in the Works for which a User obtains licenses via the Marketplace platform, which are displayed on specific Order Confirmations.

"Terms" means the terms and conditions set forth in these General Terms and any additional Order Confirmation Terms collectively.

"User" or "you" is the person or entity making the use granted under the relevant License. Where the person accepting the Terms on behalf of a User is a freelancer or other third party who the User authorized to accept the General Terms on the User's behalf, such person shall be deemed jointly a User for purposes of such Terms.

"Work(s)" are the copyright protected works described in relevant Order Confirmations.

2) **Description of Service.** CCC's Marketplace enables Users to obtain Licenses to use one or more Works in accordance with all relevant Terms. CCC grants Licenses as an agent on behalf of the copyright rightsholder identified in the relevant Order Confirmation.

3) **Applicability of Terms.** The Terms govern User's use of Works in connection with the relevant License. In the event of any conflict between General Terms and Order Confirmation Terms, the latter shall govern. User acknowledges that Rightsholders have complete discretion whether to grant any permission, and whether to place any limitations on any grant, and that CCC has no right to supersede or to modify any such discretionary act by a Rightsholder.

4) **Representations; Acceptance.** By using the Service, User represents and warrants that User has been duly authorized by the User to accept, and hereby does accept, all Terms.

5) **Scope of License; Limitations and Obligations.** All Works and all rights therein, including copyright rights, remain the

sole and exclusive property of the Rightsholder. The License provides only those rights expressly set forth in the terms and conveys no other rights in any Works

6) **General Payment Terms.** User may pay at time of checkout by credit card or choose to be invoiced. If the User chooses to be invoiced, the User shall: (i) remit payments in the manner identified on specific invoices, (ii) unless otherwise specifically stated in an Order Confirmation or separate written agreement, Users shall remit payments upon receipt of the relevant invoice from CCC, either by delivery or notification of availability of the invoice via the Marketplace platform, and (iii) if the User does not pay the invoice within 30 days of receipt, the User may incur a service charge of 1.5% per month or the maximum rate allowed by applicable law, whichever is less. While User may exercise the rights in the License immediately upon receiving the Order Confirmation, the License is automatically revoked and is null and void, as if it had never been issued, if CCC does not receive complete payment on a timely basis.

7) **General Limits on Use.** Unless otherwise provided in the Order Confirmation, any grant of rights to User (i) involves only the rights set forth in the Terms and does not include subsequent or additional uses, (ii) is non-exclusive and non-transferable, and (iii) is subject to any and all limitations and restrictions (such as, but not limited to, limitations on duration of use or circulation) included in the Terms. Upon completion of the licensed use as set forth in the Order Confirmation, User shall either secure a new permission for further use of the Work(s) or immediately cease any new use of the Work(s) and shall render inaccessible (such as by deleting or by removing or severing links or other locators) any further copies of the Work. User may only make alterations to the Work if and as expressly set forth in the Order Confirmation. No Work may be used in any way that is unlawful, including without limitation if such use would violate applicable sanctions laws or regulations, would be defamatory, violate the rights of third parties (including such third parties' rights of copyright, privacy, publicity, or other tangible or intangible property), or is otherwise illegal, sexually explicit, or obscene. In addition, User may not conjoin a Work with any other material that may result in damage to the reputation of the Rightsholder. Any unlawful use will render any licenses hereunder null and void. User agrees to inform CCC if it becomes aware of any infringement of any rights in a Work and to cooperate with any reasonable request of CCC or the Rightsholder in connection therewith.

8) **Third Party Materials.** In the event that the material for which a License is sought includes third party materials (such as photographs, illustrations, graphs, inserts and similar materials) that are identified in such material as having been used by permission (or a similar indicator), User is responsible for identifying, and seeking separate licenses (under this Service, if available, or otherwise) for any of such third party materials; without a separate license, User may not use such third party materials via the License.

9) **Copyright Notice.** Use of proper copyright notice for a Work is required as a condition of any License granted under the Service. Unless otherwise provided in the Order Confirmation, a proper copyright notice will read substantially as follows: "Used with permission of [Rightsholder's name], from [Work's title, author, volume, edition number and year of copyright]; permission conveyed through Copyright Clearance Center, Inc." Such notice must be provided in a reasonably legible font size and must be placed either on a cover page or in another location that any person, upon gaining access to the material which is the subject of a permission, shall see, or in the case of republication Licenses, immediately adjacent to the Work as used (for example, as part of a by-line or footnote) or in the place where substantially all other credits or notices for the new work containing the republished Work are located. Failure to include the required notice results in loss to the Rightsholder and CCC, and the User shall be liable to pay liquidated damages for each such failure equal to twice the use fee specified in the Order Confirmation, in addition to the use fee itself and any other fees and charges specified.

10) **Indemnity.** User hereby indemnifies and agrees to defend the Rightsholder and CCC, and their respective employees and directors, against all claims, liability, damages, costs, and expenses, including legal fees and expenses, arising out of any use of a Work beyond the scope of the rights granted herein and in the Order Confirmation, or any use of a Work which has been altered in any unauthorized way by User, including claims of defamation or infringement of rights of copyright, publicity, privacy, or other tangible or intangible property.

11) **Limitation of Liability.** UNDER NO CIRCUMSTANCES WILL CCC OR THE RIGHTSHOLDER BE LIABLE FOR ANY DIRECT, INDIRECT, CONSEQUENTIAL, OR INCIDENTAL DAMAGES (INCLUDING WITHOUT LIMITATION DAMAGES FOR LOSS OF BUSINESS PROFITS OR INFORMATION, OR FOR BUSINESS INTERRUPTION) ARISING OUT OF THE USE OR INABILITY TO USE A WORK, EVEN IF ONE OR BOTH OF THEM HAS BEEN ADVISED OF THE POSSIBILITY OF SUCH DAMAGES. In any event, the total liability of the Rightsholder and CCC (including their respective employees and directors) shall not exceed the total amount actually paid by User for the relevant License. User assumes full liability for the actions and omissions of its principals, employees, agents, affiliates, successors, and assigns.

12) **Limited Warranties.** THE WORK(S) AND RIGHT(S) ARE PROVIDED "AS IS." CCC HAS THE RIGHT TO GRANT TO USER THE

RIGHTS GRANTED IN THE ORDER CONFIRMATION DOCUMENT. CCC AND THE RIGHTSHOLDER DISCLAIM ALL OTHER WARRANTIES RELATING TO THE WORK(S) AND RIGHT(S), EITHER EXPRESS OR IMPLIED, INCLUDING WITHOUT LIMITATION IMPLIED WARRANTIES OF MERCHANTABILITY OR FITNESS FOR A PARTICULAR PURPOSE. ADDITIONAL RIGHTS MAY BE REQUIRED TO USE ILLUSTRATIONS, GRAPHS, PHOTOGRAPHS, ABSTRACTS, INSERTS, OR OTHER PORTIONS OF THE WORK (AS OPPOSED TO THE ENTIRE WORK) IN A MANNER CONTEMPLATED BY USER; USER UNDERSTANDS AND AGREES THAT NEITHER CCC NOR THE RIGHTSHOLDER MAY HAVE SUCH ADDITIONAL RIGHTS TO GRANT.

13) **Effect of Breach.** Any failure by User to pay any amount when due, or any use by User of a Work beyond the scope of the License set forth in the Order Confirmation and/or the Terms, shall be a material breach of such License. Any breach not cured within 10 days of written notice thereof shall result in immediate termination of such License without further notice. Any unauthorized (but licensable) use of a Work that is terminated immediately upon notice thereof may be liquidated by payment of the Rightsholder's ordinary license price therefor; any unauthorized (and unlicensable) use that is not terminated immediately for any reason (including, for example, because materials containing the Work cannot reasonably be recalled) will be subject to all remedies available at law or in equity, but in no event to a payment of less than three times the Rightsholder's ordinary license price for the most closely analogous licensable use plus Rightsholder's and/or CCC's costs and expenses incurred in collecting such payment.

14) **Additional Terms for Specific Products and Services.** If a User is making one of the uses described in this Section 14, the additional terms and conditions apply:

a) ***Print Uses of Academic Course Content and Materials (photocopies for academic coursepacks or classroom handouts).*** For photocopies for academic coursepacks or classroom handouts the following additional terms apply:

i) The copies and anthologies created under this License may be made and assembled by faculty members individually or at their request by on-campus bookstores or copy centers, or by off-campus copy shops and other similar entities.

ii) No License granted shall in any way: (i) include any right by User to create a substantively non-identical copy of the Work or to edit or in any other way modify the Work (except by means of deleting material immediately preceding or following the entire portion of the Work copied) (ii) permit "publishing ventures" where any particular anthology would be systematically marketed at multiple institutions.

iii) Subject to any Publisher Terms (and notwithstanding any apparent contradiction in the Order Confirmation arising from data provided by User), any use authorized under the academic pay-per-use service is limited as follows:

A) any License granted shall apply to only one class (bearing a unique identifier as assigned by the institution, and thereby including all sections or other subparts of the class) at one institution;

B) use is limited to not more than 25% of the text of a book or of the items in a published collection of essays, poems or articles;

C) use is limited to no more than the greater of (a) 25% of the text of an issue of a journal or other periodical or (b) two articles from such an issue;

D) no User may sell or distribute any particular anthology, whether photocopied or electronic, at more than one institution of learning;

E) in the case of a photocopy permission, no materials may be entered into electronic memory by User except in order to produce an identical copy of a Work before or during the academic term (or analogous period) as to which any particular permission is granted. In the event that User shall choose to retain materials that are the subject of a photocopy permission in electronic memory for purposes of producing identical copies more than one day after such retention (but still within the scope of any permission granted), User must notify CCC of such fact in the applicable permission request and such retention shall constitute one copy actually sold for purposes of calculating permission fees due; and

F) any permission granted shall expire at the end of the class. No permission granted shall in any way include any right by User to create a substantively non-identical copy of the Work or to edit or in any other way modify the Work (except by means of deleting material immediately preceding or following the entire portion of the Work copied).

iv) Books and Records; Right to Audit. As to each permission granted under the academic pay-per-use Service, User shall maintain for at least four full calendar years books and records sufficient for CCC to determine the numbers of copies made by User under such permission. CCC and any representatives it may designate shall have the right to audit such books and records at any time during User's ordinary business hours, upon two days' prior notice. If any such audit shall determine that User shall have underpaid for, or underreported, any photocopies sold or by three percent (3%) or more, then User shall bear all the costs of any such audit; otherwise, CCC shall bear the costs of any such audit. Any amount determined by such audit to have been underpaid by User shall immediately be paid to CCC by User, together with interest thereon at the rate of 10% per annum from the date such amount was originally due. The provisions of this paragraph shall survive the termination of this License for any reason.

b) ***Digital Pay-Per-Uses of Academic Course Content and Materials (e-coursepacks, electronic reserves, learning management systems, academic institution intranets).*** For uses in e-coursepacks, posts in electronic reserves, posts in learning management systems, or posts on academic institution intranets, the following additional terms apply:

i) The pay-per-uses subject to this Section 14(b) include:

A) **Posting e-reserves, course management systems, e-coursepacks for text-based content,** which grants authorizations to import requested material in electronic format, and allows electronic access to this material to members of a designated college or university class, under the direction of an instructor designated by the college or university, accessible only under appropriate electronic controls (e.g., password);

B) **Posting e-reserves, course management systems, e-coursepacks for material consisting of photographs or other still images not embedded in text,** which grants not only the authorizations described in Section 14(b)(i)(A) above, but also the following authorization: to include the requested material in course materials for use consistent with Section 14(b)(i)(A) above, including any necessary resizing, reformatting or modification of the resolution of such requested material (provided that such modification does not alter the underlying editorial content or meaning of the requested material, and provided that the resulting modified content is used solely within the scope of, and in a manner consistent with, the particular authorization described in the Order Confirmation and the Terms), but not including any other form of manipulation, alteration or editing of the requested material;

C) **Posting e-reserves, course management systems, e-coursepacks or other academic distribution for audiovisual content,** which grants not only the authorizations described in Section 14(b)(i)(A) above, but also the following authorizations: (i) to include the requested material in course materials for use consistent with Section 14(b)(i)(A) above; (ii) to display and perform the requested material to such members of such class in the physical classroom or remotely by means of streaming media or other video formats; and (iii) to "clip" or reformat the requested material for purposes of time or content management or ease of delivery, provided that such “clipping” or reformatting does not alter the underlying editorial content or meaning of the requested material and that the resulting material is used solely within the scope of, and in a manner consistent with, the particular authorization described in the Order Confirmation and the Terms. Unless expressly set forth in the relevant Order Conformation, the License does not authorize any other form of manipulation, alteration or editing of the requested material.

ii) Unless expressly set forth in the relevant Order Confirmation, no License granted shall in any way: (i) include any right by User to create a substantively non-identical copy of the Work or to edit or in any other way modify the Work (except by means of deleting material immediately preceding or following the entire portion of the Work copied or, in the case of Works subject to Sections 14(b)(1)(B) or (C) above, as described in such Sections) (ii) permit "publishing ventures" where any particular course materials would be systematically marketed at multiple institutions.

iii) Subject to any further limitations determined in the Rightsholder Terms (and notwithstanding any apparent contradiction in the Order Confirmation arising from data provided by User), any use authorized under the electronic course content pay-per-use service is limited as follows:

A) any License granted shall apply to only one class (bearing a unique identifier as assigned by the institution, and thereby including all sections or other subparts of the class) at one institution;

B) use is limited to not more than 25% of the text of a book or of the items in a published collection of essays, poems or articles;

C) use is limited to not more than the greater of (a) 25% of the text of an issue of a journal or other periodical

or (b) two articles from such an issue;

D) no User may sell or distribute any particular materials, whether photocopied or electronic, at more than one institution of learning;

E) electronic access to material which is the subject of an electronic-use permission must be limited by means of electronic password, student identification or other control permitting access solely to students and instructors in the class;

F) User must ensure (through use of an electronic cover page or other appropriate means) that any person, upon gaining electronic access to the material, which is the subject of a permission, shall see:

- a proper copyright notice, identifying the Rightsholder in whose name CCC has granted permission,
- a statement to the effect that such copy was made pursuant to permission,
- a statement identifying the class to which the material applies and notifying the reader that the material has been made available electronically solely for use in the class, and
- a statement to the effect that the material may not be further distributed to any person outside the class, whether by copying or by transmission and whether electronically or in paper form, and User must also ensure that such cover page or other means will print out in the event that the person accessing the material chooses to print out the material or any part thereof.

G) any permission granted shall expire at the end of the class and, absent some other form of authorization, User is thereupon required to delete the applicable material from any electronic storage or to block electronic access to the applicable material.

iv) Uses of separate portions of a Work, even if they are to be included in the same course material or the same university or college class, require separate permissions under the electronic course content pay-per-use Service. Unless otherwise provided in the Order Confirmation, any grant of rights to User is limited to use completed no later than the end of the academic term (or analogous period) as to which any particular permission is granted.

v) Books and Records; Right to Audit. As to each permission granted under the electronic course content Service, User shall maintain for at least four full calendar years books and records sufficient for CCC to determine the numbers of copies made by User under such permission. CCC and any representatives it may designate shall have the right to audit such books and records at any time during User's ordinary business hours, upon two days' prior notice. If any such audit shall determine that User shall have underpaid for, or underreported, any electronic copies used by three percent (3%) or more, then User shall bear all the costs of any such audit; otherwise, CCC shall bear the costs of any such audit. Any amount determined by such audit to have been underpaid by User shall immediately be paid to CCC by User, together with interest thereon at the rate of 10% per annum from the date such amount was originally due. The provisions of this paragraph shall survive the termination of this license for any reason.

c) ***Pay-Per-Use Permissions for Certain Reproductions (Academic photocopies for library reserves and interlibrary loan reporting) (Non-academic internal/external business uses and commercial document delivery).*** The License expressly excludes the uses listed in Section (c)(i)-(v) below (which must be subject to separate license from the applicable Rightsholder) for: academic photocopies for library reserves and interlibrary loan reporting; and non-academic internal/external business uses and commercial document delivery.

i) electronic storage of any reproduction (whether in plain-text, PDF, or any other format) other than on a transitory basis;

ii) the input of Works or reproductions thereof into any computerized database;

iii) reproduction of an entire Work (cover-to-cover copying) except where the Work is a single article;

iv) reproduction for resale to anyone other than a specific customer of User;

v) republication in any different form. Please obtain authorizations for these uses through other CCC services or directly from the rightsholder.

Any license granted is further limited as set forth in any restrictions included in the Order Confirmation and/or in these Terms.

d) ***Electronic Reproductions in Online Environments (Non-Academic-email, intranet, internet and extranet).*** For "electronic reproductions", which generally includes e-mail use (including instant messaging or other electronic transmission to a defined group of recipients) or posting on an intranet, extranet or Intranet site (including any display or performance incidental thereto), the following additional terms apply:

i) Unless otherwise set forth in the Order Confirmation, the License is limited to use completed within 30 days for any use on the Internet, 60 days for any use on an intranet or extranet and one year for any other use, all as measured from the "republication date" as identified in the Order Confirmation, if any, and otherwise from the date of the Order Confirmation.

ii) User may not make or permit any alterations to the Work, unless expressly set forth in the Order Confirmation (after request by User and approval by Rightsholder); provided, however, that a Work consisting of photographs or other still images not embedded in text may, if necessary, be resized, reformatted or have its resolution modified without additional express permission, and a Work consisting of audiovisual content may, if necessary, be "clipped" or reformatted for purposes of time or content management or ease of delivery (provided that any such resizing, reformatting, resolution modification or “clipping” does not alter the underlying editorial content or meaning of the Work used, and that the resulting material is used solely within the scope of, and in a manner consistent with, the particular License described in the Order Confirmation and the Terms.

15) **Miscellaneous.**

a) User acknowledges that CCC may, from time to time, make changes or additions to the Service or to the Terms, and that Rightsholder may make changes or additions to the Rightsholder Terms. Such updated Terms will replace the prior terms and conditions in the order workflow and shall be effective as to any subsequent Licenses but shall not apply to Licenses already granted and paid for under a prior set of terms.

b) Use of User-related information collected through the Service is governed by CCC's privacy policy, available online at www.copyright.com/about/privacy-policy/.

c) The License is personal to User. Therefore, User may not assign or transfer to any other person (whether a natural person or an organization of any kind) the License or any rights granted thereunder; provided, however, that, where applicable, User may assign such License in its entirety on written notice to CCC in the event of a transfer of all or substantially all of User's rights in any new material which includes the Work(s) licensed under this Service.

d) No amendment or waiver of any Terms is binding unless set forth in writing and signed by the appropriate parties, including, where applicable, the Rightsholder. The Rightsholder and CCC hereby object to any terms contained in any writing prepared by or on behalf of the User or its principals, employees, agents or affiliates and purporting to govern or otherwise relate to the License described in the Order Confirmation, which terms are in any way inconsistent with any Terms set forth in the Order Confirmation, and/or in CCC's standard operating procedures, whether such writing is prepared prior to, simultaneously with or subsequent to the Order Confirmation, and whether such writing appears on a copy of the Order Confirmation or in a separate instrument.

e) The License described in the Order Confirmation shall be governed by and construed under the law of the State of New York, USA, without regard to the principles thereof of conflicts of law. Any case, controversy, suit, action, or proceeding arising out of, in connection with, or related to such License shall be brought, at CCC's sole discretion, in any federal or state court located in the County of New York, State of New York, USA, or in any federal or state court whose geographical jurisdiction covers the location of the Rightsholder set forth in the Order Confirmation. The parties expressly submit to the personal jurisdiction and venue of each such federal or state court.

Last updated October 2022

References

[1]J. J. Deng and S. D. Peterson, "Examining the influence of epithelium layer modeling approaches on vocal fold kinematics and kinetics", Biomech. Model. Mechanobiol. **22**, 479–493 (2023).

[2]J. J. Deng, B. D. Erath, M. Zañartu, and S. D. Peterson, "The effect of swelling on vocal fold kinematics and dynamics", Biomech. Model. Mechanobiol., 10.1007/s10237-023-01740-3 (2023).

[3]Z. Zhang, "Mechanics of human voice production and control", J. Acoust. Soc. Am. **140**, 2614–2635 (2016).

[4]G. Fant, "The source filter concept in voice production (Quarterly Progress and Status Report)", Stl-Qpsr **1**, 21–37 (1981).

[5]J. L. Flanagan, *Speech Analysis Synthesis and Perception*, 1st ed. (Springer Berlin Heidelberg, Berlin, Heidelberg, 1965).

[6]N. Roy, R. M. Merrill, S. D. Gray, and E. M. Smith, "Voice Disorders in the General Population: Prevalence, Risk Factors, and Occupational Impact", Laryngoscope **115**, 1988–1995 (2005).

[7]R. M. Merrill, A. E. Anderson, and A. Sloan, "Quality of life indicators according to voice disorders and voice-related conditions", Laryngoscope **121**, 2004–2010 (2011).

[8]M. D. Morrison, L. A. Rammage, G. M. Belisle, C. B. Pullan, and H. Nichol, "Muscular tension dysphonia.", J. Otolaryngol. **12**, 302–6 (1983).

[9]J. Oates and A. Winkworth, "Current knowledge, controversies and future directions in hyperfunctional voice disorders", Int. J. Speech. Lang. Pathol. **10**, 267–277 (2008).

[10]N. Roy, "Assessment and treatment of musculoskeletal tension in hyperfunctional voice disorders", Int. J. Speech. Lang. Pathol. **10**, 195–209 (2008).

[11]V. S. McKenna, J. A. Hylkema, M. C. Tardif, and C. E. Stepp, "Voice Onset Time in Individuals With Hyperfunctional Voice Disorders: Evidence for Disordered Vocal Motor Control", J. Speech, Lang. Hear. Res. **63**, 405–420 (2020).

[12]R. E. Hillman, E. B. Holmberg, J. S. Perkell, M. Walsh, and C. Vaughan, "Objective Assessment of Vocal Hyperfunction", J. Speech, Lang. Hear. Res. **32**, 373–392 (1989).

[13]R. E. Hillman, C. E. Stepp, J. H. Van Stan, M. Zañartu, and D. D. Mehta, "An updated theoretical framework for vocal hyperfunction", Am. J. Speech-Language Pathol. **29**, 2254–2260 (2020).

[14]V. M. Espinoza, M. Zañartu, J. H. Van Stan, D. D. Mehta, and R. E. Hillman, "Glottal aerodynamic measures in women with phonotraumatic and nonphonotraumatic vocal hyperfunction", J. Speech, Lang. Hear. Res. **60**, 2159–2169 (2017).

[15]G. E. Galindo, S. D. Peterson, B. D. Erath, C. Castro, R. E. Hillman, and M. Zañartu, "Modeling the Pathophysiology of Phonotraumatic Vocal Hyperfunction With a Triangular Glottal Model of the Vocal Folds", J. Speech, Lang. Hear. Res. **60**, 2452–2471 (2017).

[16]M. Zañartu, G. E. Galindo, B. D. Erath, S. D. Peterson, G. R. Wodicka, and R. E. Hillman, "Modeling the effects of a posterior glottal opening on vocal fold dynamics with implications for vocal hyperfunction", J. Acoust. Soc. Am. **136**, 3262–3271 (2014).

[17]M. Hirano, Y. Kakita, K. Ohmaru, and S. Kurita, "Structure and Mechanical Properties of the Vocal Fold", in *Speech lang.* Vol. 7, edited by N. J. Lass, 1st ed. (Elsevier, 1982), pp. 271–297.

[18]I. R. Titze, "The physics of small-amplitude oscillation of the vocal folds", J. Acoust. Soc. Am. **83**, 1536–1552 (1988).

[19]D. K. Chhetri, Z. Zhang, and J. Neubauer, "Measurement of Young's Modulus of Vocal Folds by Indentation", J. Voice **25**, 1–7 (2011).

[20]Z. Zhang, J. Neubauer, and D. A. Berry, "Physical mechanisms of phonation onset: A linear stability analysis of an aeroelastic continuum model of phonation", J. Acoust. Soc. Am. **122**, 2279–2295 (2007).

[21]Z. Zhang, "Characteristics of phonation onset in a two-layer vocal fold model", J. Acoust. Soc. Am. **125**, 1091–1102 (2009).

[22]Z. Zhang, "Dependence of phonation threshold pressure and frequency on vocal fold geometry and biomechanics", J. Acoust. Soc. Am. **127**, 2554–2562 (2010).

[23]J. E. Kelleher, T. H. Siegmund, and R. W. Chan, "Could Spatial Heterogeneity in Human Vocal Fold Elastic Properties Improve the Quality of Phonation?", Ann. Biomed. Eng. **40**, 2708–2718 (2012).

[24]F. Benboujja and C. Hartnick, "Quantitative evaluation of the human vocal fold extracellular matrix using multiphoton microscopy and optical coherence tomography", Sci. Rep. **11**, 2440 (2021).

[25]B. Geng, Q. Xue, and X. Zheng, "The effect of vocal fold vertical stiffness variation on voice production", J. Acoust. Soc. Am. **140**, 2856–2866 (2016).

[26]P. Bhattacharya, J. E. Kelleher, and T. H. Siegmund, "Role of gradients in vocal fold elastic modulus on phonation", J. Biomech. **48**, 3356–3363 (2015).

[27]K. Verdolini, C. A. Rosen, R. C. Branski, and P. A. Hebda, "Shifts in biochemical markers associated with wound healing in laryngeal secretions following phonotrauma: A preliminary study", Ann. Otol. Rhinol. Laryngol. **112**, 1021–1025 (2003).

[28]E. J. Hunter and I. R. Titze, "Quantifying Vocal Fatigue Recovery: Dynamic Vocal Recovery Trajectories after a Vocal Loading Exercise", Ann. Otol. Rhinol. Laryngol. **118**, 449–460 (2009).

[29]K. Gou and T. J. Pence, "Hyperelastic modeling of swelling in fibrous soft tissue with application to tracheal angioedema", J. Math. Biol. **72**, 499–526 (2016).

[30]R. W. Bastian, A. Keidar, and K. Verdolini-Marston, "Simple vocal tasks for detecting vocal fold swelling", J. Voice **4**, 172–183 (1990).

[31]Z. Zhang, "Influence of flow separation location on phonation onset", J. Acoust. Soc. Am. **124**, 1689–1694 (2008).

[32]N. Bhattacharyya, "The prevalence of voice problems among adults in the United States", Laryngoscope **124**, 2359–2362 (2014).

[33]L. Wu and Z. Zhang, "A Computational Study of Vocal Fold Dehydration During Phonation", IEEE Trans. Biomed. Eng. **64**, 2938–2948 (2017).

[34]L. Wu and Z. Zhang, "Computational Study of the Impact of Dehydration-Induced Vocal Fold Stiffness Changes on Voice Production", J. Voice, `10.1016/j.jvoice.2022.02.001` (2022).

[35]R. Mittal, B. D. Erath, and M. W. Plesniak, "Fluid Dynamics of Human Phonation and Speech", Annu. Rev. Fluid Mech. **45**, 437–467 (2013).

[36]J. A. Seikel, D. G. Drumright, and D. W. King, *Anatomy & physiology for speech, language, and hearing* (Cengage Learning, 2015).

[37]M. Hirano, W. Vennard, and J. Ohala, "Regulation of Register, Pitch and Intensity of Voice", Folia Phoniatr. Logop. **22**, 1–20 (1970).

[38]I. R. Titze and B. H. Story, "Rules for controlling low-dimensional vocal fold models with muscle activation", J. Acoust. Soc. Am. **112**, 1064–1076 (2002).

[39]P. Šidlof, J. G. Švec, J. Horáček, J. Veselý, I. Klepáček, and R. Havlík, "Geometry of human vocal folds and glottal channel for mathematical and biomechanical modeling of voice production", J. Biomech. **41**, 985–995 (2008).

[40]M. Hirano, "Morphological Structure of the Vocal Cord as a Vibrator and its Variations", Folia Phoniatr. Logop. **26**, 89–94 (1974).

[41]H. R. Weerathunge, G. A. Alzamendi, G. J. Cler, F. H. Guenther, C. E. Stepp, and M. Zañartu, "LaDIVA: A neurocomputational model providing laryngeal motor control for speech acquisition and production", PLOS Comput. Biol. **18**, edited by F. E. Theunissen, e1010159 (2022).

[42]H. L. Pick, G. M. Siegel, P. W. Fox, S. R. Garber, and J. K. Kearney, "Inhibiting The Lombard Effect", J. Acoust. Soc. Am. **85**, 894–900 (1989).

[43]J. Van den Berg, J. T. Zantema, and P. Doornenbal, "On the Air Resistance and the Bernoulli Effect of the Human Larynx", J. Acoust. Soc. Am. **29**, 626–631 (1957).

[44]B. D. Erath, S. D. Peterson, M. Zañartu, G. R. Wodicka, and M. W. Plesniak, "A theoretical model of the pressure field arising from asymmetric intraglottal flows applied to a two-mass model of the vocal folds", J. Acoust. Soc. Am. **130**, 389–403 (2011).

[45]D. A. Berry and I. R. Titze, "Normal modes in a continuum model of vocal fold tissues", J. Acoust. Soc. Am. **100**, 3345–3354 (1996).

[46]M. Triep, C. Brücker, and W. Schröder, "High-speed PIV measurements of the flow downstream of a dynamic mechanical model of the human vocal folds", Exp. Fluids **39**, 232–245 (2005).

[47]B. D. Erath and M. W. Plesniak, "An investigation of asymmetric flow features in a scaled-up driven model of the human vocal folds", Exp. Fluids **49**, 131–146 (2010).

[48]R. S. McGowan, "An aeroacoustic approach to phonation", J. Acoust. Soc. Am. **83**, 696–704 (1988).

[49]M. H. Krane, "Aeroacoustic production of low-frequency unvoiced speech sounds", J. Acoust. Soc. Am. **118**, 410–427 (2005).

[50]L. E. Kinsler, A. R. Frey, A. B. Coppens, and J. V. Sanders, *Fundamentals of Acoustics*, 4th ed. (John Wiley and Sons, 2000).

[51]I. R. Titze, "Nonlinear source–filter coupling in phonation: Theory", J. Acoust. Soc. Am. **123**, 2733–2749 (2008).

[52]I. Steinecke and H. Herzel, "Bifurcations in an asymmetric vocal-fold model", J. Acoust. Soc. Am. **97**, 1874–1884 (1995).

[53]B. D. Erath, M. Zañartu, K. C. Stewart, M. W. Plesniak, D. E. Sommer, and S. D. Peterson, "A review of lumped-element models of voiced speech", Speech Commun. **55**, 667–690 (2013).

[54]B. H. Story and I. R. Titze, "Voice simulation with a body-cover model of the vocal folds", J. Acoust. Soc. Am. **97**, 1249–1260 (1995).

[55]J. L. Flanagan and L. Landgraf, "Self-oscillating source for vocal-tract synthesizers", IEEE Trans. Audio Electroacoust. **16**, 57–64 (1968).

[56]K. Ishizaka and J. L. Flanagan, "Synthesis of Voiced Sounds From a Two-Mass Model of the Vocal Cords", Bell Syst. Tech. J. **51**, 1233–1268 (1972).

[57]N. Ruty, X. Pelorson, A. Van Hirtum, I. Lopez-Arteaga, and A. Hirschberg, "An in vitro setup to test the relevance and the accuracy of low-order vocal folds models", J. Acoust. Soc. Am. **121**, 479–490 (2007).

[58]M. Döllinger, U. Hoppe, F. Hettlich, J. Lohscheller, S. Schuberth, and U. Eysholdt, "Vibration parameter extraction from endoscopic image series of the vocal folds", IEEE Trans. Biomed. Eng. **49**, 773–781 (2002).

[59]M. E. Gurtin, E. Fried, and L. Anand, *The mechanics and thermodynamics of continua* (Cambridge University Press, 2010).

[60]P. Wriggers, *Computational Contact Mechanics*, 2nd ed. (Springer Berlin Heidelberg, Berlin, Heidelberg, 2006).

[61]Y.-c. Fung, *Biomechanics: mechanical properties of living tissues* (Springer Science & Business Media, 2013).

[62]X. Zheng, "Biomechanical Modelling of Glottal Aerodynamics and Vocal Fold Vibration during Phonation", Doctoral thesis (The George Washington University, 2009), p. 192.

[63]G. Link, M. Kaltenbacher, M. Breuer, and M. Döllinger, "A 2D finite-element scheme for fluid–solid–acoustic interactions and its application to human phonation", Comput. Methods Appl. Mech. Eng. **198**, 3321–3334 (2009).

[64]X. Zheng, Q. Xue, R. Mittal, and S. Beilamowicz, "A Coupled Sharp-Interface Immersed Boundary-Finite-Element Method for Flow-Structure Interaction With Application to Human Phonation", J. Biomech. Eng. **132**, 111003 (2010).

[65]K. J. Bathe, *Finite Element Procedures*, 2nd ed. (Klaus-Jürgen Bathe, Watertown, MA, 2006).

[66]F. Alipour-Haghighi, D. A. Berry, and I. R. Titze, "A finite-element model of vocal-fold vibration", J. Acoust. Soc. Am. **108**, 3003–3012 (2000).

[67]X. Zheng, S. A. Bielamowicz, H. Luo, and R. Mittal, "A Computational Study of the Effect of False Vocal Folds on Glottal Flow and Vocal Fold Vibration During Phonation", Ann. Biomed. Eng. **37**, 625–642 (2009).

[68]X. Zheng, R. Mittal, Q. Xue, and S. A. Bielamowicz, "Direct-numerical simulation of the glottal jet and vocal-fold dynamics in a three-dimensional laryngeal model", J. Acoust. Soc. Am. **130**, 404–415 (2011).

[69]Z. Li, Y. Chen, S. Chang, and H. Luo, "A Reduced-Order Flow Model for Fluid–Structure Interaction Simulation of Vocal Fold Vibration", J. Biomech. Eng. **142**, 1–10 (2020).

[70]H. Luo, R. Mittal, X. Zheng, S. A. Bielamowicz, R. J. Walsh, and J. K. Hahn, "An immersed-boundary method for flow-structure interaction in biological systems with application to phonation", J. Comput. Phys. **227**, 9303–9332 (2008).

[71]G. Z. Decker and S. L. Thomson, "Computational Simulations of Vocal Fold Vibration: Bernoulli Versus Navier–Stokes", J. Voice **21**, 273–284 (2007).

[72]P. Anderson, S. Fels, and S. Green, "Implementation and Validation of a 1D Fluid Model for Collapsible Channels", J. Biomech. Eng. **135**, 10.1115/1.4025326 (2013).

[73]A. Vasudevan, "The voice box: a fast coupled vocal fold model for articulatory speech synthesis", Master's thesis (University of British Columbida, 2017).

[74]C. Cancelli and T. J. Pedley, "A separated-flow model for collapsible-tube oscillations", J. Fluid Mech. **157**, 375–404 (1985).

[75]A. Vasudevan, V. Zappi, P. Anderson, and S. Fels, "A Fast Robust 1D Flow Model for a Self-Oscillating Coupled 2D FEM Vocal Fold Simulation", in Interspeech 2017, Vol. 2017-Augus (2017), pp. 3482–3486.

[76]F. Alipour-Haghighi and R. C. Scherer, "Dynamic glottal pressures in an excised hemilarynx model", J. Voice **14**, 443–454 (2000).

[77]C. Tao and J. J. Jiang, "Anterior-posterior biphonation in a finite element model of vocal fold vibration", J. Acoust. Soc. Am. **120**, 1570–1577 (2006).

[78]W. Zhao, C. Zhang, S. H. Frankel, and L. Mongeau, "Computational aeroacoustics of phonation, Part I: Computational methods and sound generation mechanisms", J. Acoust. Soc. Am. **112**, 2134–2146 (2002).

[79]S. L. Thomson, L. Mongeau, and S. H. Frankel, "Aerodynamic transfer of energy to the vocal folds", J. Acoust. Soc. Am. **118**, 1689–1700 (2005).

[80]F. Alipour-Haghighi and R. C. Scherer, "Time-Dependent Pressure and Flow Behavior of a Self-oscillating Laryngeal Model With Ventricular Folds", J. Voice **29**, 649–659 (2015).

[81]J. Yang, X. Wang, M. Krane, and L. T. Zhang, "Fully-coupled aeroelastic simulation with fluid compressibility — For application to vocal fold vibration", Comput. Methods Appl. Mech. Eng. **315**, 584–606 (2017).

[82]P. Šidlof, J. Horáček, and V. Řidký, "Parallel CFD simulation of flow in a 3D model of vibrating human vocal folds", Comput. Fluids **80**, 290–300 (2013).

[83]J. D. Anderson and J. Wendt, *Computational fluid dynamics*, Vol. 206 (Springer, 1995).

[84]C. Zhang, W. Zhao, S. H. Frankel, and L. Mongeau, "Computational aeroacoustics of phonation, Part II: Effects of flow parameters and ventricular folds", J. Acoust. Soc. Am. **112**, 2147–2154 (2002).

[85]W. Jiang, X. Zheng, and Q. Xue, "Influence of vocal fold cover layer thickness on its vibratory dynamics during voice production", J. Acoust. Soc. Am. **146**, 369–380 (2019).

[86]H. Sadeghi, M. Döllinger, M. Kaltenbacher, and S. Kniesburges, "Aerodynamic impact of the ventricular folds in computational larynx models", J. Acoust. Soc. Am. **145**, 2376–2387 (2019).

[87]G. Fant, *Acoustic theory of speech production: with calculations based on x-ray studies of russian articulations*, 2 (Walter de Gruyter, 1971).

[88]B. H. Story, "Physiologically-Based Speech Simulation Using an Enhanced Wave-Reflection Model of the Vocal Tract", Doctor of Philosophy (University of Iowa, 1995).

[89]J. L. Flanagan, K. Ishizaka, and K. Shipley, "Synthesis of speech from a dynamic model of the vocal cords and vocal tract", Bell Syst. Tech. J. **54**, 485–506 (1975).

[90]M. Zañartu, L. Mongeau, and G. R. Wodicka, "Influence of acoustic loading on an effective single mass model of the vocal folds", J. Acoust. Soc. Am. **121**, 1119–1129 (2007).

[91]G. Fant, "Quarterly Progress and Status Report: Glottal source and excitation analysis.", Stl-Qpsr **20**, 85–107 (1979).

[92]Y.-R. Chien, D. D. Mehta, J. Guenason, M. Zañartu, and T. F. Quatieri, "Evaluation of Glottal Inverse Filtering Algorithms Using a Physiologically Based Articulatory Speech Synthesizer", IEEE/ACM Trans. Audio, Speech, Lang. Process. **25**, 1718–1730 (2017).

[93]M. Rothenberg, "A new inverse-filtering technique for deriving the glottal air flow waveform during voicing", J. Acoust. Soc. Am. **53**, 1632–1645 (1973).

[94]M. Zañartu, J. C. Ho, D. D. Mehta, R. E. Hillman, and G. R. Wodicka, "Subglottal impedance-based inverse filtering of voiced sounds using neck surface acceleration", IEEE Trans. Audio. Speech. Lang. Processing **21**, 1929–1939 (2013).

[95]W. Jiang, X. Zheng, and Q. Xue, "Computational Modeling of Fluid–Structure–Acoustics Interaction during Voice Production", Front. Bioeng. Biotechnol. **5**, 1–10 (2017).

[96]S. H. Strogatz, *Nonlinear dynamics and chaos: with applications to physics, biology, chemistry, and engineeringNo Title*, 2nd ed. (CRC Press, Boca Raton, 2018).

[97]C. P. Jackson, "A finite-element study of the onset of vortex shedding in flow past variously shaped bodies", J. Fluid Mech. **182**, 23 (1987).

[98]A. Griewank and G. Reddien, "The Calculation of Hopf Points by a Direct Method", IMA J. Numer. Anal. **3**, 295–303 (1983).

[99]D. Roose and V. Hlavaček, "A Direct Method for the Computation of Hopf Bifurcation Points", SIAM J. Appl. Math. **45**, 879–894 (1985).

[100]R. E. King, K. Steed, A. E. Rivera, J. J. Wisco, and S. L. Thibeault, "Magnetic resonance imaging quantification of dehydration and rehydration in vocal fold tissue layers", PLoS One **13**, 1–17 (2018).

[101]J. Gordon Betts, P. Desaix, E. Johnson, J. E. Johson, O. Korol, D. Kruse, B. Poe, J. A. Wise, M. Womble, and K. A. Young, *Anatomy and Physiology 2e*, 2nd ed. (OpenStax, Houston, 2022).

[102]G. Guven, M. P. Hilty, and C. Ince, "Microcirculation: Physiology, Pathophysiology, and Clinical Application", Blood Purif. **49**, 143–150 (2020).

[103]J. R. Levick and C. C. Michel, "Microvascular fluid exchange and the revised Starling principle", Cardiovasc. Res. **87**, 198–210 (2010).

[104]E. H. Starling, "On the Absorption of Fluids from the Connective Tissue Spaces", J. Physiol. **19**, 312–326 (1896).

[105]P. S. Mortimer and J. R. Levick, "Chronic peripheral oedema: The critical role of the lymphatic system", Clin. Med. J. R. Coll. Physicians London **4**, 448–453 (2004).

[106]D. M. McDONALD, G. THURSTON, and P. BALUK, "Endothelial Gaps as Sites for Plasma Leakage in Inflammation", Microcirculation **6**, 7–22 (1999).

[107]R. K. Reed, Å. Lidén, and K. Rubin, "Edema and fluid dynamics in connective tissue remodelling", J. Mol. Cell. Cardiol. **48**, 518–523 (2010).

[108]R. W. Chan and N. Tayama, "Biomechanical effects of hydration in vocal fold tissues", Otolaryngol. - Head Neck Surg. **126**, 528–537 (2002).

[109]S. Yang, Y. Zhang, R. D. Mills, and J. J. Jiang, "Quantitative Study of the Effects of Dehydration on the Viscoelastic Parameters in the Vocal Fold Mucosa", J. Voice **31**, 269–274 (2017).

[110]L. R. G. Treloar, *The Physics of Rubber Elasticity*, 3rd ed. (Oxford University Press, 2005).

[111]C. Frantz, K. M. Stewart, and V. M. Weaver, "The extracellular matrix at a glance", J. Cell Sci. **123**, 4195–4200 (2010).

[112]Y. Zhang, L. Czerwonka, C. Tao, and J. J. Jiang, "A biphasic theory for the viscoelastic behaviors of vocal fold lamina propria in stress relaxation", J. Acoust. Soc. Am. **123**, 1627–1636 (2008).

[113]A. K. Miri, F. Barthelat, and L. Mongeau, "Effects of dehydration on the viscoelastic properties of vocal folds in large deformations", J. Voice **26**, 688–697 (2012).

[114]W. M. Lai, J. S. Hou, and V. C. Mow, "A triphasic theory for the swelling and deformation behaviors of articular cartilage", J. Biomech. Eng. **113**, 245–258 (1991).

[115]W. Wilson, C. C. Van Donkelaar, and J. M. Huyghe, "A comparison between mechano-electrochemical and biphasic swelling theories for soft hydrated tissues", J. Biomech. Eng. **127**, 158–165 (2005).

[116]H. Tsai, T. J. Pence, and E. Kirkinis, "Swelling Induced Finite Strain Flexure in a Rectangular Block of an Isotropic Elastic Material", J. Elast. **75**, 69–89 (2004).

[117]M. Movahhedi, B. Geng, Q. Xue, and X. Zheng, "Effects of cricothyroid and thyroarytenoid interaction on voice control: Muscle activity, vocal fold biomechanics, flow, and acoustics", J. Acoust. Soc. Am. **150**, 29–42 (2021).

[118]P. J. Hadwin, M. Motie-Shirazi, B. D. Erath, and S. D. Peterson, "Bayesian Inference of Vocal Fold Material Properties from Glottal Area Waveforms Using a 2D Finite Element Model", Appl. Sci. **9**, 2735 (2019).

[119]R. C. Scherer, D. Shinwari, K. J. De Witt, C. Zhang, B. R. Kucinschi, and A. A. Afjeh, "Intraglottal pressure profiles for a symmetric and oblique glottis with a divergence angle of 10 degrees", J. Acoust. Soc. Am. **109**, 1616–1630 (2001).

[120]Y.-C. Fung, *Biomechanics*, 2nd ed. (Springer New York, New York, NY, 1993).

[121]A. Logg, M. Kent-Andre, and G. N. Wells, *Automated Solution of Differential Equations by the Finite Element Method*, edited by A. Logg, K.-A. Mardal, and G. Wells, Vol. 84, Lecture Notes in Computational Science and Engineering (Springer Berlin Heidelberg, Berlin, Heidelberg, 2012).

[122]A. Logg and G. N. Wells, "DOLFIN", ACM Trans. Math. Softw. **37**, 1–28 (2010).

[123]R. Phillips, Y. Zhang, M. Keuler, C. Tao, and J. J. Jiang, "Measurement of liquid and solid component parameters in canine vocal fold lamina propria", J. Acoust. Soc. Am. **125**, 2282–2287 (2009).

[124]N. Boullé, P. E. Farrell, and M. E. Rognes, "Optimal control of Hopf bifurcations", (2022).

[125]D. M. Hamby, "A review of techniques for parameter sensitivity", Environ. Monit. Assess. **32**, 135 –154 (1994).

[126]N. M. Newmark, "A Method of Computation for Structural Dynamics", Trans. Am. Soc. Civ. Eng. **127**, 1406–1433 (1962).

[127]B. A. Pickup and S. L. Thomson, "Identification of geometric parameters influencing the flow-induced vibration of a two-layer self-oscillating computational vocal fold model", J. Acoust. Soc. Am. **129**, 2121–2132 (2011).

[128]R. W. Chan and I. R. Titze, "Viscoelastic shear properties of human vocal fold mucosa: Measurement methodology and empirical results", J. Acoust. Soc. Am. **106**, 2008–2021 (1999).

[129]X. Wang, W. Jiang, X. Zheng, and Q. Xue, "A computational study of the effects of vocal fold stiffness parameters on voice production", J. Voice, 10.1016/j.jvoice.2019.09.004 (2019).

[130]M. Hirano and Y. Kakita, "Cover-body theory of vocal fold vibration", in *Speech sci. recent adv.* Edited by R. Daniloff (College-Hill Press, San Diego, CA, 1985), pp. 1–46.

[131]P. J. Hadwin, B. D. Erath, and S. D. Peterson, "The influence of flow model selection on finite element model parameter estimation using Bayesian inference", JASA Express Lett. **1**, 045204 (2021).

[132]E. B. Holmberg, R. E. Hillman, and J. S. Perkell, "Glottal airflow and transglottal air pressure measurements for male and female speakers in soft, normal, and loud voice", J. Acoust. Soc. Am. **84**, 511–529 (1988).

[133]I. R. Titze, J. J. Jiang, and T.-Y. Hsiao, "Measurement of Mucosal Wave Propagation and Vertical Phase Difference in Vocal Fold Vibration", Ann. Otol. Rhinol. Laryngol. **102**, 58–63 (1993).

[134]D. Chapelle and K. J. Bathe, "Fundamental considerations for the finite element analysis of shell structures", Comput. Struct. **66**, 19–36 (1998).

[135]G. A. Holzapfel, R. Eberlein, P. Wriggers, and H. W. Weizsäcker, "Large strain analysis of soft biological membranes: Formulation and finite element analysis", Comput. Methods Appl. Mech. Eng. **132**, 45–61 (1996).

[136]P. Hansbo and M. G. Larson, "Finite element modeling of a linear membrane shell problem using tangential differential calculus", Comput. Methods Appl. Mech. Eng. **270**, 1–14 (2014).

[137]M. Delfour and J.-P. Zolésio, "A Boundary Differential Equation for Thin Shells", J. Differ. Equ. **119**, 426–449 (1995).

[138]M. Delfour and J.-P. Zolésio, "Tangential Differential Equations for Dynamical Thin/Shallow Shells", J. Differ. Equ. **128**, 125–167 (1996).

[139]P. R. Murray and S. L. Thomson, "Synthetic, Multi-Layer, Self-Oscillating Vocal Fold Model Fabrication", J. Vis. Exp., e3498 (2011).

[140]P. R. Murray and S. L. Thomson, "Vibratory responses of synthetic, self-oscillating vocal fold models", J. Acoust. Soc. Am. **132**, 3428–3438 (2012).

[141]Y. Xuan and Z. Zhang, "Influence of embedded fibers and an epithelium layer on the glottal closure pattern in a physical vocal fold model", J. Speech, Lang. Hear. Res. **57**, 416–425 (2014).

[142]J. R. Tse, Z. Zhang, and J. L. Long, "Effects of vocal fold epithelium removal on vibration in an excised human larynx model", J. Acoust. Soc. Am. **138**, EL60–EL64 (2015).

[143]P. Bhattacharya and T. H. Siegmund, "A computational study of systemic hydration in vocal fold collision", Comput. Methods Biomech. Biomed. Engin. **17**, 1835–1852 (2014).

[144]I. R. Titze, J. G. Švec, and P. S. Popolo, "Vocal Dose Measures", J. Speech, Lang. Hear. Res. **46**, 919–932 (2003).

[145]I. R. Titze and E. J. Hunter, "Comparison of Vocal Vibration-Dose Measures for Potential-Damage Risk Criteria", J. Speech, Lang. Hear. Res. **58**, 1425–1439 (2015).

[146]M. Motie-Shirazi, M. Zañartu, S. D. Peterson, and B. D. Erath, "Vocal fold dynamics in a synthetic self-oscillating model: Contact pressure and dissipated-energy dose", J. Acoust. Soc. Am. **150**, 478–489 (2021).

[147]H. E. Gunter, "Mechanical Stresses in Vocal Fold Tissue during Voice Production", Doctoral thesis (Harvard University, 2003), p. 105.

[148]Q. Xue, X. Zheng, S. Bielamowicz, and R. Mittal, "Sensitivity of vocal fold vibratory modes to their three-layer structure: Implications for computational modeling of phonation", J. Acoust. Soc. Am. **130**, 965–976 (2011).

[149]B. A. Pickup and S. L. Thomson, "Flow-induced vibratory response of idealized versus magnetic resonance imaging-based synthetic vocal fold models", J. Acoust. Soc. Am. **128**, EL124–EL129 (2010).

[150]Z. Zhang, "Interaction between epilaryngeal and laryngeal adjustments in regulating vocal fold contact pressure", JASA Express Lett. **1**, 025201 (2021).

[151]T. J. Pence and H. Tsai, "On the cavitation of a swollen compressible sphere in finite elasticity", Int. J. Non. Linear. Mech. **40**, 307–321 (2005).

[152]M. E. Gurtin, E. Fried, and L. Anand, *The Mechanics and Thermodynamics of Continua* (Cambridge University Press, 2010).

[153]K. Gou, H. Topol, H. Demirkoparan, and T. J. Pence, "Stress-Swelling Finite Element Modeling of Cervical Response with Homeostatic Collagen Fiber Distributions", J. Biomech. Eng. **142**, 80–90 (2020).

[154]J. N. Friedman, R. D. Goldman, R. Srivastava, and P. C. Parkin, "Development of a clinical dehydration scale for use in children between 1 and 36 months of age", J. Pediatr. **145**, 201–207 (2004).

[155]A. K. Miri, "Mechanical characterization of vocal fold tissue: A review study", J. Voice **28**, 657–667 (2014).

[156]Z. Zhang, "Respiratory Laryngeal Coordination in Airflow Conservation and Reduction of Respiratory Effort of Phonation", J. Voice **30**, 760.e7–760.e13 (2016).

[157]E. B. Holmberg, R. E. Hillman, J. S. Perkell, and C. Gress, "Relationships between intra-speaker variation in aerodynamic measures of voice production and variation in SPL across repeated recordings", J. Speech Hear. Res. **37**, 484–495 (1994).

[158]R. L. Milbrath and N. P. Solomon, "Do vocal warm-up exercises alleviate vocal fatigue?", J. Speech, Lang. Hear. Res. **46**, 422–436 (2003).

[159]C. Tao, J. J. Jiang, and Y. Zhang, "Simulation of vocal fold impact pressures with a self-oscillating finite-element model", J. Acoust. Soc. Am. **119**, 3987–3994 (2006).

[160]I. R. Titze, "Mechanical stress in phonation", J. Voice **8**, 99–105 (1994).

[161]H. E. Gunter, "Modeling mechanical stresses as a factor in the etiology of benign vocal fold lesions", J. Biomech. **37**, 1119–1124 (2004).

[162]C. Tao and J. J. Jiang, "Mechanical stress during phonation in a self-oscillating finite-element vocal fold model", J. Biomech. **40**, 2191–2198 (2007).

[163]D. K. Chhetri and S. Rafizadeh, "Young's modulus of canine vocal fold cover layers", J. Voice **28**, 406–410 (2014).

[164]P. Hansbo, M. G. Larson, and F. Larsson, "Tangential differential calculus and the finite element modeling of a large deformation elastic membrane problem", Comput. Mech. **56**, 87–95 (2015).

[165]V. Hernandez, J. E. Roman, and V. Vidal, "SLEPC: A scalable and flexible toolkit for the solution of eigenvalue problems", ACM Trans. Math. Softw. **31**, 351–362 (2005).

Appendices

Appendix A

Sensitivity of phonation onset pressure to vocal fold stiffness distribution

A.1 Sensitivity of phonation onset pressure

To solve for Hopf bifurcations, we use the Griewank-Reddien equations, given by

$$F_{\text{Hopf}} = \begin{pmatrix} F \\ \partial F/\partial X \Delta X_{\text{r}} + \omega \partial F/\partial \dot{X} \Delta X_{\text{i}} \\ \partial F/\partial X \Delta X_{\text{i}} - \omega \partial F/\partial \dot{X} \Delta X_{\text{r}} \\ Z^{\intercal} \Delta X_{\text{r}} \\ Z^{\intercal} \Delta X_{\text{i}} - 1 \end{pmatrix}, \tag{A.1}$$

$$X_{\text{Hopf}} = \begin{pmatrix} X & \Delta X_{\text{i}} & \Delta X_{\text{r}} & p_{\text{sub}} & \omega \end{pmatrix}^{\intercal}, \tag{A.2}$$

where ω is frequency of the neutrally stable oscillation, $\Delta X = \Delta X_r + \Delta X_i j$ is the mode of the oscillation (with real part ΔX_r and imaginary part ΔX_i; $j = \sqrt{-1}$), and Z is a constant vector used to normalize the real and imaginary modes [98]; herein we chose all components of Z to equal 1 ($Z[i] = 1$ for all i). We employ a Newton method to iteratively determine the phonation onset state from an initial guess by finding the state, X_{Hopf}, that satisfies the residual

$$F_{\text{Hopf}}(X_{\text{Hopf}}; E) = 0, \tag{A.3}$$

for a known distribution of stiffness, E.

To generate an initial guess for the iterative solution of Equation (A.3), we compute fixed points and stabilities of the fixed points over a range of subglottal pressures, $p_{\text{sub}} = 0\,\text{Pa}$ to $800\,\text{Pa}$ in $100\,\text{Pa}$ increments. Fixed-points in Equation (3.7) correspond to a static state and are found by solving

$$F(X_{\text{fp}}, 0) = 0, \tag{A.4}$$

using an iterative Newton method, where X_{fp} denotes the fixed-point state. Stability of the fixed points was assessed by solving an eigenvalue problem for small perturbations, $\Delta X = \Delta X_r + \Delta X_i j$, about the fixed point given by [96, 97]

$$(\omega_r + \omega_i j)\left(\frac{\partial F}{\partial \dot{X}}\right)_{X_{\text{fp}}} (\Delta X_{\text{r}} + \Delta X_{\text{i}} j) = \left(\frac{\partial F}{\partial X}\right)_{X_{\text{fp}}} (\Delta X_{\text{r}} + \Delta X_{\text{i}} j). \tag{A.5}$$

A positive ω_r corresponds to an unstable mode with angular frequency ω_i. We locate a pressure interval where a mode transitions from stable to unstable and use conditions at the midpoint of this interval as an initial guess for X_{Hopf}. At the midpoint, we compute the fixed point and stability of the system for the midpoint pressure, p_{sub}, to find $X_{\text{fp}}, \Delta X_{\text{i}}, \Delta X_{\text{r}}, \omega_r, \omega_i$. We normalize the modes to satisfy the normalization conditions in the Griewank-Reddien equations using

$$\begin{aligned}
\overline{\Delta X_{\text{r}}} + \overline{\Delta X_{\text{i}}} j &= (a + bj)(\Delta X_{\text{r}} + \Delta X_{\text{i}} j), \\
a &= \frac{\Delta X_{\text{i}}^{\intercal} Z}{(\Delta X_{\text{i}}^{\intercal} Z)^2 + (\Delta X_{\text{r}}^{\intercal} Z)^2}, \\
b &= \frac{\Delta X_{\text{r}}^{\intercal} Z}{(\Delta X_{\text{i}}^{\intercal} Z)^2 + (\Delta X_{\text{r}}^{\intercal} Z)^2},
\end{aligned}$$

where $\overline{\Delta X_{\text{r}}} + \overline{\Delta X_{\text{i}}} j$ can be seen to satisfy the the final two blocks of Equation (A.1). This results in the initial guess

$$X_{\text{Hopf}} = \begin{pmatrix} X_{\text{fp}} & \overline{\Delta X_{\text{i}}} & \overline{\Delta X_{\text{r}}} & p_{\text{sub}} & \omega_i \end{pmatrix}^{\intercal},$$

where the quantities are obtained at the midpoint as described.

While Hopf bifurcations can also be located by iteratively testing subglottal pressures and determining the stability of the fixed points (for example, by testing stability of intervals as described previously), solution of Hopf bifurcations by the Griewank-Reddien equations has at least two key benefits. Firstly, the nonlinear system of equations characterizes the conditions for a Hopf bifurcation to occur so can be solved to high accuracy

with an iterative method (Newton's method), and thus locates phonation onset with high accuracy. Secondly, the nonlinear system of equations form a differentiable relationship characterizing onset which allows computation of the sensitivity of onset to stiffness for deviations about a linearization point. This strategy is employed to characterize the sensitivity of onset pressure and frequency with respect to stiffness, as outlined in Section A.1 below.

Sensitivity analysis of the Hopf bifurcation system

To characterize the gradient of onset pressure to arbitrary stiffness distributions, we use an adjoint approach to compute these sensitivities from the Griewank-Reddien equations, which has a computational cost similar to solving the Griewank-Reddien equations themselves. Consider an arbitrary non-linear functional of the Hopf state, $\hat{G}(X_{\text{Hopf}})$, and the same non-linear functional viewed as a pure function of E, $G(E) = \hat{G}(X_{\text{Hopf}}(E))$, where, $X_{\text{Hopf}}(E)$, involves the implicit solution of the Griewank-Reddien equations at the given stiffness distribution, and where $\hat{(\cdot)}$ is used to distinguish between the functionals. The respective gradients are then related by

$$\frac{\partial G}{\partial E} = -\frac{\partial \hat{G}}{\partial X_{\text{Hopf}}}\left(\frac{\partial F_{\text{Hopf}}}{\partial X_{\text{Hopf}}}\right)^{-1}\left(\frac{\partial F_{\text{Hopf}}}{\partial E}\right), \tag{A.6}$$

where solving $(\partial F_{\text{Hopf}}/\partial X_{\text{Hopf}})^{-\intercal}\partial \hat{G}/\partial X_{\text{Hopf}}^{\intercal}$ corresponds to the adjoint problem and has a similar cost to a single iteration of the Newton method when solving Equation (A.3). For the case of onset pressure, the functional is given by

$$\widehat{p_{\text{on}}}(X_{\text{Hopf}}) = \begin{pmatrix} 0 & 0 & 0 & 1 & 0 \end{pmatrix} X_{\text{Hopf}} = p_{\text{sub}}, \tag{A.7}$$

and Equation (A.6) is used to compute their gradients $(\partial p_{\text{on}}/\partial E, \partial f_{\text{on}}/\partial E)$ with respect to stiffness.

To characterize the Hessian of onset pressure with respect to arbitrary stiffness distributions, we use a finite-difference method to approximate the action of the Hessian along a given direction, ΔE, and couple this with the Krylov-Schur method of SLEPc [165] to compute an eigenvalue decomposition of the Hessian

$$\frac{\partial^2 G}{\partial E^2}\Delta E_i = \Lambda_i \Delta E_i \tag{A.8}$$

where $\Delta E_i, \Lambda_i$ are the eigenvectors and eigenvalues, respectively, and i is the index. To compute the Hessian vector products needed by the Krylov-Schur method, we use the

strategy for computing gradients described previously and a finite difference approximation

$$\frac{\partial^2 G}{\partial E^2}\Delta E \approx \frac{||\Delta E||_{l_2(\Omega)}}{h}\left(\left(\frac{\partial G}{\partial E}\right)_{E+h\widehat{\Delta E}} - \left(\frac{\partial G}{\partial E}\right)_{E}\right), \tag{A.9}$$

$$\widehat{\Delta E} = \frac{\Delta E}{||\Delta E||_{l_2(\Omega)}}, \tag{A.10}$$

where $||\Delta E||_{l_2(\Omega)} = \sqrt{\int_\Omega (\Delta E)^2 d\boldsymbol{X}}$ (the norm over the function, ΔE, corresponding to ΔE) and h are chosen to scale the perturbation to avoid the effects of numerical error. The step size, h, in the finite difference approximation must be chosen sufficiently large so that numerical round-off error is mitigated while simultaneously being small enough to accurately approximate the derivative. We tested a range of step sizes $h = (1\times10^{-2}, 1\times10^{-3}, 1\times10^{-4})$ (see Appendix A.3), and found the eigenvalue decomposition was not affected over this range; as such, we select $h = 1 \times 10^{-3}$ moving forward.

A.2 Effect of separation point location

As mentioned in Section 3.3, sensitivities of onset pressure can be strongly affected by the ad hoc separation point prescription used in the Bernoulli equation. The separation point model enforces flow separation at a fixed vertex location (Equation (3.3) and Equation (3.2)), and therefore displacement of the separation point impacts pressures over the entire medial surface. By using discontinuous changes in stiffness around the separation point, the point can be made to move nearly independently of the remainder of the medial surface and greatly impact the onset conditions. This is illustrated in Figure A.1. For the first column of Figure A.1, the first eigenvector has a discontinuity situated close to the separation point location. The second eigenvector, which is smooth, has only a weak discontinuity. Similarly, for the second column and second eigenvector the discontinuity is situated close to the shifted separation location. This suggests the discontinuity is associated with moving the location of the separation point.

We note that placing the separation point further upstream resulted in instability of the Griewank-Reddien equations, so only the two pictured separation points were considered.

While the separation point model results in discontinuities in eigenvectors for certain linearization points, the 'smooth' eigenvectors have physical meaning that are not a product of the specific separation point model. This can be partly seen in the qualitative similarities between 'smooth' eigenvectors in Figure A.1 which resemble the BC-like eigenvectors in

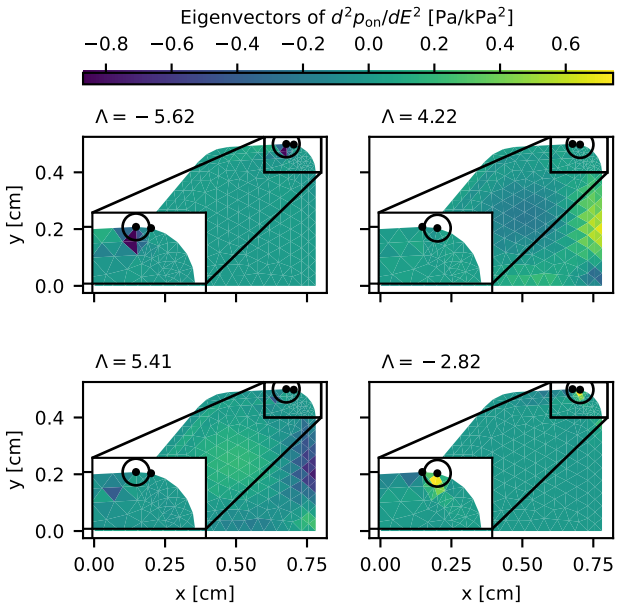

Figure A.1: Eigendecomposition of the Hessian for the linearization point $(E_\mathrm{b}, E_\mathrm{c}) = (6\,\mathrm{kPa}, 2\,\mathrm{kPa})$ with varying separation point, indicated by a circle. Eigenvectors are sorted in descending order by the largest absolute value of the eigenvalue from top to bottom and are also normalized by the max-min difference, $\max(\Delta E_i) - \min(\Delta E_i)$

Figure 3.3. Figure A.2 further illustrates this using the eigenvector decomposition of the Hessian for the linearization $(E_\mathrm{b}, E_\mathrm{c}) = (6\,\mathrm{kPa}, 6\,\mathrm{kPa})$, where separation point induced discontinuities did not occur. As the separation point moves, the first eigenvector shares qualitative characteristics, although the associated eigenvalue does change. The fact that the eigenvector appears similar across different separation points suggests this eigenvector is a product of bulk flow forcing, rather than the separation model.

Preliminary experiments showed that discontinuities are particularly prevalent when the medial surface stiffness is loose and/or when the prephonatory gap is small. This is likely the ability of glottal flow pressures to drive motion increases under small prephonatory gaps and/or low medial surface stiffnesses. When the VFs are nearly closed, for example, small motions of the separation point can drastically change the area ratios, $a(s)/a_\mathrm{sep}$, over the medial surface, which results in dramatic pressure predictions from the Bernoulli equation for small displacements; these large pressures can induce significant motion of the VFs. Low medial surface stiffnesses also result in larger displacements of the medial surface for the same surface pressure. This could be why separation point discontinuities

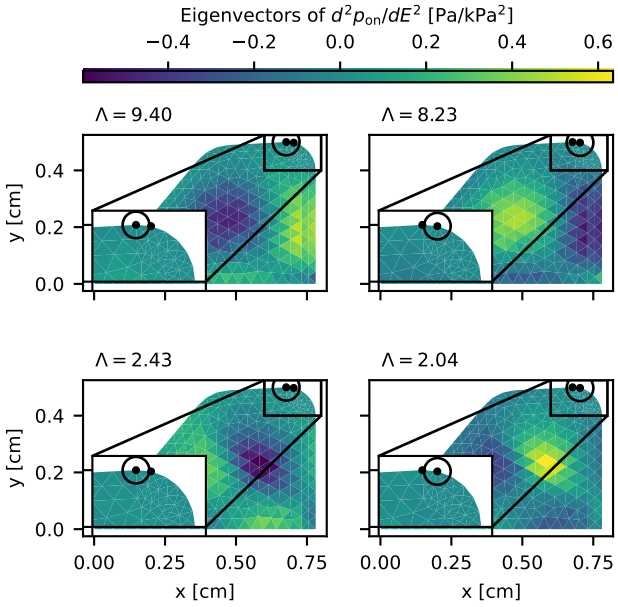

Figure A.2: Eigendecomposition of the Hessian for the linearization point $(E_\mathrm{b}, E_\mathrm{c}) = (6\,\mathrm{kPa}, 6\,\mathrm{kPa})$ with varying separation point, indicated by a circle. Eigenvectors are sorted in descending order by the largest real value of the eigenvalue from top to bottom and are also normalized by the max-min difference, $\max(\Delta E_i) - \min(\Delta E_i)$

are seen for the $(E_\mathrm{b}, E_\mathrm{c}) = (6\,\mathrm{kPa}, 2\,\mathrm{kPa})$ linearization point (Figure A.1) and not the $(E_\mathrm{b}, E_\mathrm{c}) = (6\,\mathrm{kPa}, 6\,\mathrm{kPa})$ linearization point (Figure A.2).

Taylor model of onset pressure

To better interpret the quadratic approximation from Equation (3.9) (for both projected and non-layered sensitivities), the Taylor approximation is further decomposed based on eigenvalues of the Hessian and the critical point of the quadratic approximation. To illustrate this, four schematic cases are illustrated in Figure A.3 for the case where stiffness, $E = (E_\mathrm{c}, E_\mathrm{b})$, varies only in the cover and body layers, which allows for plotting in 2D. In all cases we see that elliptical contours are present representing either a quadratic or a saddle surface with a critical point where the gradient is zero. Figure A.3 A illustrates the case where the Hessian has two positive eigenvalues, Λ, therefore indicating a minimum in onset pressure for a particular combination of $E^* = (E_\mathrm{b}, E_\mathrm{c})$. The larger the eigenvalue, the faster the onset pressure varies along the associated eigenvector and thus the more

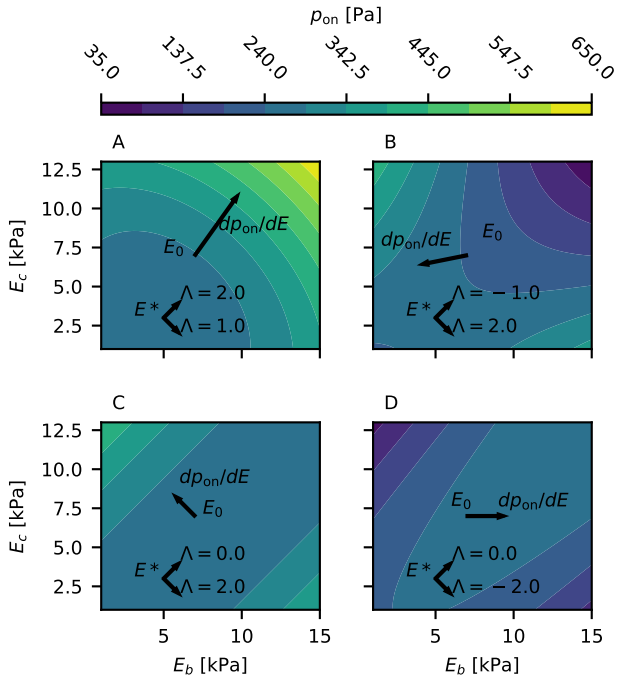

Figure A.3: Schematic second order Taylor models for onset pressure for a two-layer body cover stiffness variation. Eigenvectors and values of the quadratic surface are illustrated at the critical point, E^*, while the gradient, $\partial p_{on}/\partial E$, is shown at the linearization point, E_0. The subplots represent: (a) two non-negligible eigenvalues, (b) one positive and one negative eigenvalue, (c) one non-negligible eigenvalue (d) one non-negligible eigenvalue with a linear change in the direction of 0 curvature.

compressed contours are along the direction. Figure A.3 B illustrates the case of one positive and one negative eigenvalue resulting in a saddle surface. Figure A.3 C illustrates one positive eigenvalue and one 0 eigenvalue; in this case the dependence of onset pressure on stiffness is one-dimensional along the eigenvector with non-zero eigenvalue since variations in onset pressure along directions with 0 curvature are negligible. Figure A.3 D illustrates the same eigendecomposition as Figure A.3 C, but with a linear increase along the 0 curvature direction; the dependence of onset pressure on stiffness here is two-dimensional with quadratic increases in the direction of the eigenvector and linear increases orthogonal to it.

To compute this Taylor model for onset pressure, we find a subset of n eigenpairs of the Hessian that have the most significant effect on onset pressure and use these to determine

the critical point, E^*. For our case, we found that only one or two eigenpairs had significant impacts on onset pressure. The eigenvectors forms a matrix of basis vectors

$$A_{\text{eig}} = \left[\Delta E_1, \ldots, \Delta E_n\right],$$

where each eigenvector is normalized such that $||\Delta E_i||_2 = 1$. We find the critical point E^* in the low-dimensional basis by solving for the point where the gradient is zero

$$\begin{aligned} A_{\text{eig}}^{\intercal}\left(\frac{\partial^2 p_{\text{on}}}{\partial E^2}\right)_{E_0} A_{\text{eig}} B = A_{\text{eig}}^{\intercal}\left(\frac{\partial p_{\text{on}}}{\partial E}\right)_{E_0}^{\intercal} \\ E^* = E_0 - AB, \end{aligned} \tag{A.11}$$

where B is a vector of coefficients in the basis A_{eig} (note that A_{eig} diagonalizes the Hessian making the solution straightforward). The predicted onset pressure at this critical point is found by substitution into Equation (3.9)

$$p_{\text{on}}{}^* = p_{\text{on}}(E_0) - \frac{1}{2}\left(\frac{\partial p_{\text{on}}}{\partial E}\right)_{E_0} AB. \tag{A.12}$$

Finally, to compute any linear effect (as in Figure A.3 D), we remove any components of the gradient along the eigenvector basis

$$\Delta E_0 = \frac{\partial p_{\text{on}}}{\partial E}(1 - A_{\text{eig}}^{\intercal} A_{\text{eig}}), \tag{A.13}$$

where ΔE_0 denotes the direction of linear increase in onset pressure. The Taylor model then gives a low-dimensional interpretation of the dependence of onset pressure on stiffness based on stiffness changes around the critical point, as given in Equation (3.10).

A.3 Mesh density and hessian-vector product step size independence

To assess the dependence of our results on mesh density and the step size approximation used in Equation (A.9), the Hessian of onset pressure was computed for a range of coarse-to-fine meshes and step sizes as shown in Figure A.4. Figure A.4 shows that changing mesh density or step size within the chosen range has minimal effects on the first eigenpair. Eigenvectors are qualitatively similar while eigenvalues, adjusted for the norm $||(\cdot)||_{l_2(\Omega)}$ (see Equation (3.12)), change only slightly. Adjusting eigenvalues for the norm $||(\cdot)||_{l_2(\Omega)}$ is

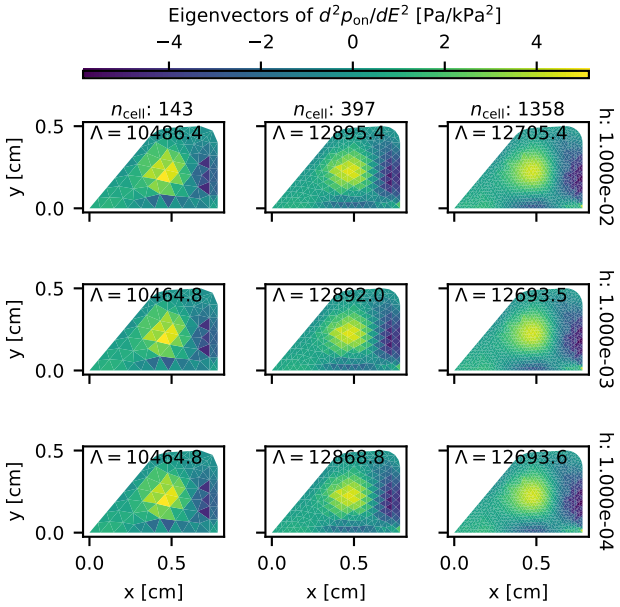

Figure A.4: The first eigenpair of the Hessian of onset pressure for the linearization point $(E_b, E_c) = (6\,\text{kPa}, 6\,\text{kPa})$ and for varying step size, h, (see Equation (A.9)) and mesh density as measured by the number of cells, n_{cell}. Eigenvectors and eigenvalues are normalized by the norm $||(\cdot)||_{l_2(\Omega)}$

required to ensure that eigenvalues are comparable across different mesh densities. Ideally, eigenvalues would converge to a fixed value as mesh density increases, which does not occur here. This could be a product of the Hessian approximation using finite differences which may have introduced errors that prevent this convergence from occurring. Due to the approximate mesh and step size independence, the first mesh ($n_{cell} = 397$) and step size, $h = 1 \times 10^{-3}$, were selected for computing results.

Appendix B

The effect of swelling on vocal fold kinematics and dynamics

B.1 Swelling constitutive equation

Let the deformation from a reference configuration, $\boldsymbol{X}$, to spatial coordinates, $\boldsymbol{x}$, be given by $\boldsymbol{x} = \boldsymbol{X} + \boldsymbol{u}(\boldsymbol{X})$. Then $\boldsymbol{F} = \partial \boldsymbol{u}/\partial \boldsymbol{X}$ is the deformation gradient and $\boldsymbol{E} = 1/2(\boldsymbol{F}^\intercal \boldsymbol{F} - \boldsymbol{I})$ is the Green strain tensor. To incorporate the effects of swelling, Gou and Pence [116, 151] proposed an extension of a hyperelastic strain energy w to the form (the strain energy is formulated here with dependence on $\boldsymbol{E}$ instead of $\boldsymbol{F}$ where the relation between the two strain energies is $w(\boldsymbol{E}) = w(1/2(\boldsymbol{F}^\intercal \boldsymbol{F} - \boldsymbol{I})) = w(\boldsymbol{F})$)

$$\bar{w}(\boldsymbol{E}; v) = m(v) w(\bar{\boldsymbol{E}}(\boldsymbol{E}; v)) \tag{B.1}$$

where $\bar{w}$ is the swelling generalized strain energy, w is the original strain energy, v is the swelling, and $m(v)$ is a scalar valued monotonic function that satisfies $m(1) = 1$. The swelling modified deformation gradient is given by

$$\bar{\boldsymbol{F}}(\boldsymbol{F}; v) = v^{-1/3} \boldsymbol{F};$$

and the swelling modified Green strain by

$$\bar{\boldsymbol{E}}(\boldsymbol{E}; v) = \frac{1}{2}(\bar{\boldsymbol{F}}^T \bar{\boldsymbol{F}} - \boldsymbol{I}) = v^{-2/3} \boldsymbol{E} + \frac{1}{2}(v^{-2/3} - 1)\boldsymbol{I}.$$

The second Piola-Kirchhoff stress for the swelling modified strain energy is

$$\begin{aligned}\bar{\boldsymbol{S}} &= \frac{\partial \bar{w}(\boldsymbol{E}; v)}{\partial \boldsymbol{E}} \\ &= m(v)\frac{\partial w(\bar{\boldsymbol{E}})}{\partial \bar{\boldsymbol{E}}}\frac{\partial \bar{\boldsymbol{E}}}{\partial \boldsymbol{E}} \\ &= m(v)v^{-2/3}\frac{\partial w(\bar{\boldsymbol{E}})}{\partial \bar{\boldsymbol{E}}} \\ &= m(v)v^{-2/3}\boldsymbol{S}|_{\bar{\boldsymbol{E}}(\boldsymbol{E};v)}\end{aligned} \tag{B.2}$$

For a Saint Venant-Kirchhoff material $w(\boldsymbol{E}) = \lambda(\mathrm{Tr}\boldsymbol{E})^2 + \mu\mathrm{Tr}\boldsymbol{E}^2$ so that the second Piola-Kirchhoff stress is

$$\boldsymbol{K}_{ijkl} = \lambda\delta_{ij}\delta_{kl} + \mu(\delta_{ik}\delta_{jl} + \delta_{il}\delta_{jk}), \tag{B.3}$$

$$\boldsymbol{S} = \boldsymbol{K}\boldsymbol{E} = \lambda\mathrm{Tr}\boldsymbol{E}\boldsymbol{I} + 2\mu\boldsymbol{E}, \tag{B.4}$$

where μ and λ are Lame's parameters. Substituting the above (Equation (B.4)) into $\bar{\boldsymbol{S}}$ (Equation (B.2)) results in

$$\bar{\boldsymbol{S}} = \frac{m(v)}{v}v^{1/3}\left(\lambda\mathrm{Tr}\bar{\boldsymbol{E}}\boldsymbol{I} + 2\mu\bar{\boldsymbol{E}},\right), \tag{B.5}$$

where $\boldsymbol{K}$ is the constant elasticity tensor for a Saint Venant-Kirchhoff material.

To determine how $m(v)$ changes the modulus with swelling, consider the reference configuration coordinate, $\boldsymbol{X}^\star$, corresponding to equiaxial expansion by the prescribed swelling such that $\partial\boldsymbol{X}^\star/\partial\boldsymbol{X} = v^{1/3}\boldsymbol{I}$. The deformation gradient and Green strain measured with respect to the unswollen reference configuration, $\boldsymbol{X}$, and with respect to the swollen reference configuration, $\boldsymbol{X}^\star$, are then related by

$$\boldsymbol{F}^\star = v^{-1/3}\boldsymbol{F}$$

$$\boldsymbol{E}^\star = \frac{1}{2}(\boldsymbol{F}^{\star\intercal}\boldsymbol{F}^\star - \boldsymbol{I}) = v^{-2/3}\boldsymbol{E} + \frac{1}{2}(v^{-2/3} - 1)\boldsymbol{I},$$

identical to the relation between $\bar{\boldsymbol{E}}$ and $\boldsymbol{E}$ described above. The strain energy of the material with respect to the swollen reference configuration is

$$w^\star(\boldsymbol{E}^\star; v) = m(v)\frac{w(\bar{\boldsymbol{E}}(\boldsymbol{E}, v))}{v} = m(v)\frac{w(\boldsymbol{E}^\star)}{v}$$

where the factor $1/v$ is due to the volume increase. The tangent modulus with respect to the swollen configuration is then given by

$$\frac{\partial^2 w^\star(\boldsymbol{E}^\star; v)}{\partial(\boldsymbol{E}^\star)^2} = \frac{m(v)}{v}\frac{\partial^2 w(\boldsymbol{E}^\star)}{\partial(\boldsymbol{E}^\star)^2} = \frac{m(v)}{v}\boldsymbol{K},$$

where $\boldsymbol{K}$ is the elasticity tensor of the swollen material. This shows that the change in modulus is controlled by $m(v)/v$,

To simplify investigating different functional forms of $m(v)$, we approximate the effect of $m(v)/v$ with a linear approximation

$$\bar{\boldsymbol{S}} \approx (\bar{m}'|_{v=1}(v-1)+1)v^{-1/3}\left(\lambda \mathrm{Tr}\bar{\boldsymbol{E}}\boldsymbol{I} + 2\mu\bar{\boldsymbol{E}},\right) \tag{B.6}$$

where $\bar{m} = m(v)/v$.

B.2 Independence study

The mesh density in Figure 5.1 and time step Δt were chosen based on a mesh and time step independence study shown in Figure B.1. The mean (over time and the cover region) for von Mises stress and viscous dissipation rate both converge to within 1 % of the finest discretization case (mesh size scale of 0.5 and Δt refinement factor of 16) by a Δt factor of 8 for the mesh refinement factor of 1. Errors in mean (over time) for contact force and area similarly converge by the same refinement condition. Therefore a time step of $\Delta t = 1.25 \times 10^{-5}$ s and the mesh refinement factor of 1 (corresponding to the mesh shown in Figure 5.1) were chosen.

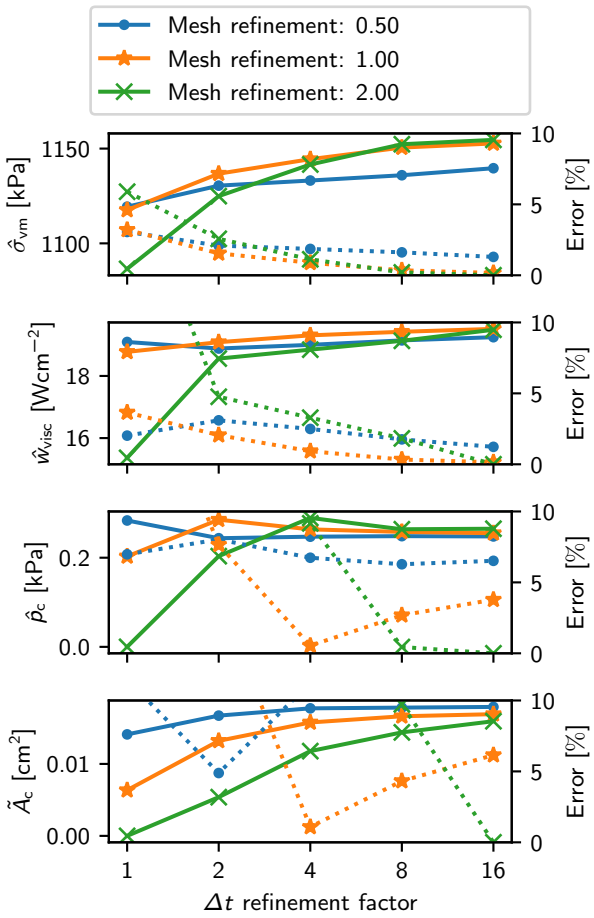

Figure B.1: Mesh and time step independence study results in terms of 4 derived quantities for the case $(v, \bar{m}') = (1.3\,, -1.6\,)$. Solid lines show absolute values while dotted lines show errors relative to the finest mesh and time step case (mesh refinement of 2 and time step refinement of 16)

Glossary

General

phonation The production of speech sounds involving quasi-periodic oscillation of the vocal folds

glottis The space in the airway between the vocal folds.

viscoelastic Describing a material with both viscous and elastic behaviour.

Speech disorders

etiology The cause (or causes) of a disease or disorder.

phonotrauma Damage sustained by the vocal folds due to phonation and excessive voice usage

phonotraumatic lesion Growths on the vocal fold surface that occur due to damage sustained by the vocal (phonotrauma). Different types of lesions are classified according to their appearance and cause and include nodules, polyps, and cysts.

nodule A type of phonotraumatic lesions, typically appearing as small symmetric bumps on both left and right vocal folds

Anatomy

coronal Relating to the coronal plane of the body. The coronal plane splits the body into front and back halves (see Figure 2.1 A).

sagittal	Relating to the sagittal plane of the body. The sagittal plane splits the body into imaginary left and right halves (see Figure 2.1 A).
transverse	Relating to the transverse plane of the body. The transverse plane splits the body into imaginary top and bottom halves (see Figure 2.1 A).
medial	Relating to the middle of the body (see Figure 2.1 A).
lateral	Relating to either side (left or right) of the body (see Figure 2.1 A).
inferior	Relating to the bottom of the body (see Figure 2.1 A).
superior	Relating to the top of the body (see Figure 2.1 A).
anterior	Relating to the front of the body (see Figure 2.1 A).
posterior	Near the back of the body (see Figure 2.1 A).